RIJKSUNIVERSITEIT GRONINGEN

Frustrated magnets: non-collinear spin textures, excitations and dynamics

Proefschrift

ter verkrijging van het doctoraat in de
Wiskunde en Natuurwetenschappen
aan de Rijksuniversiteit Groningen
op gezag van de
Rector Magnificus, dr. E. Sterken,
in het openbaar te verdedigen op
maandag, 13 februari 2012
om 12.45 uur

door

Sergey Leonidovich Artyukhin

geboren op 24 februari 1984
te Tambov, Rusland

Promotores:	Prof. dr. M. V. Mostovoy
	Prof. dr. J. Knoester
Beoordelingscommissie:	Prof. dr. S. Blügel
	Prof. dr. D. I. Khomskii
	Prof. dr. G. A. Sawatzky

Contents

Chapter 1

Introduction

1.1 Outline

Interacting electron systems are of both fundamental and practical interest. At low enough temperatures interactions between electrons win the competition with thermal fluctuations and stabilize long-range ordered states, characterized by order parameters describing collective degrees of freedom [1]. These degrees of freedom, such as magnetization and polarization, are much less sensitive to thermal fluctuations than the states of a single electron. That is why ordered, or *ferroic*, materials are widely used in information storage devices. For instance, in all the modern hard drives the unit of information, or *bit*, is represented by the magnetization direction of a tiny area on the surface of a magnetic material. Thus deep understanding of related physics is crucial for improving the energy efficiency, response time, information density and reliability of devices.

This thesis is mainly devoted to the study of magnetic materials with competing, or *frustrated*, interactions. Such interactions would alone stabilize different states, but being present in the system simultaneously, they have to find a compromise, which usually leads to non-collinear spin textures. For example, in perovskite manganites $GdMnO_3$ and $TbMnO_3$, containing antiferromagnetically coupled chains, interactions within the chains are frustrated. The nearest-neighbor interaction, irrespective of its sign, favors ferromagnetic alignment of next-nearest-neighbor spins thus competing with the antiferromagnetic next-nearest-neighbor intrachain interaction, J_2 [2–4]. The compromise is found in a magnetic spiral state, in which spins rotate in space. Frustration results in a rich variety of non-collinear spin states. Many such states break inversion symmetry and induce an electric polarization [5, 6], thus making the material *multiferroic* (multiferroics are the materials with different ferroic orders, such as ferromagnetism and ferroelectricity, present simultaneously in a single phase [7]). This opens a route to control magnetism by electric fields, which is very desirable for spintronics and information storage applications.

Frustration does not only occur due to next-nearest-neighbor interactions, but can even arise in systems with only the nearest-neighbor exchange interactions due to a special lattice geometry, incompatible with magnetic interactions – the so-called *geometric frustration* [8]. For example, in triangular antiferromagnets with nearest-neighbor interactions, frustration leads to the state with the 120° angle between neighboring spins. In Pb_2MnO_4 geometric frustration results in a very unusual state with the neighboring spins in *ab* planes being almost perpendicular to each other. Finally, in YMn_2O_5 both the $J_1 - J_2$ and geometric frustrations coexist: the $J_1 - J_2$ competing interactions in the chains stabilize a spin spiral ordering, while the weaker geometrically frustrated interactions between the chains orient spins in the neighboring chains almost perpendicularly to each other. The near orthogonality of the neighboring spins in the *ab* planes of Pb_2MnO_4, and in the neigboring chains of YMn_2O_5 results in small exchange fields from the neighbors and, consequently, in narrow magnon bands, making the magnetic system very sensitive to an applied magnetic field.

In antiferromagnets frustration can be induced locally by doping. In $FeTiO_3$ the spins in neighboring Fe layers are antiferromagnetically coupled. A Fe impurity located between the layers mediates strong local ferromagnetic coupling between them, which frustrates the antiferromagnetic ordering (Chapter 2). The result is the formation of a spin polaron – a distortion of the antiferromagnetic ordering, carrying a large ferromagnetic moment. At around 5% doping the overlapping polarons percolate, and their magnetic moments order ferromagnetically. Non-isovalent doping introduces a hole, which in the electric field shifts to one of the layers, making it more ferromagnetic and thus changing the polaron magnetic moment – the polaron magnetoelectric effect, which in $FeTiO_3$ could lead to magnetodielectric anomalies.

In antiferromagnets with two interpenetrating sublattices frustration occurs naturally without any doping. In $TbFeO_3$ an Fe^{3+} ion is exchange-coupled to its nearest eight Tb ions, and since the Tb spins are antiferromagnetically ordered, the effective fields acting on the Fe spin from the Tb ions cancel each other. However, if the Tb ordering is non-uniform, the compensation of the effective fields is lifted, and a non-zero effective field proportional to the derivative of the Tb order parameter is exerted on the Fe spin. This is described by the so-called Lifshitz term in the free energy density, involving a spatial derivative of order parameters. In the uniform state this term is zero. Thus, in order to gain energy due to this term, the system develops a periodic modulation. This explains a spectacular large-period solitonic lattice observed in $TbFeO_3$.

Another highlight of Chapter 3 is the analogy between domain walls in the Tb magnetic ordering interacting through the distortions of the Fe ordering and the Yukawa force between the nucleons exchanging by pions. This analogy allows us to explain two very different length scales of the observed incommensurate state: the atomically sharp Tb domain walls and the 340Å period of the solitonic lattice.

The same mechanism gives rise to interactions between the domain walls in the multiferroic $GdFeO_3$, in which limited magnetoelectric control was realized [9]. The polarization in this material is proportional to the product of Gd and Fe antiferromagnetic order parameters. The Fe magnetic ordering is also weakly ferromagnetic, which makes possible to switch it by a magnetic field, and since the purely antiferromagnetic Gd order does not couple to magnetic field, the sign of the polarization upon the reversal of magnetic field should be reversed. However the polarization is not reversed in the experiment, indicating that the Gd order parameter does change in an applied magnetic field. This can be explained by the drag of the Gd domain walls by the moving domain walls in the Fe magnetic ordering. Chapter 4 is devoted to the theory of this effect. This is to our knowledge the first study of the coupled domain wall motion, which is of large importance for the field of magnetoelectric switching in multiferroics.

Another fascinating multiferroic material, where different types of domain walls interact and even induce each other, is hexagonal $YMnO_3$. Experiment shows the clamped ferroelectric and antiferromagnetic domain walls [10] and hexagonal structural vortices with the electric polarization changing sign six times around the vortex core [11]. We have formulated the Landau-type theory describing the interacting structural, charge and spin degrees of freedom and explain experimental findings on the shape of structural vortices, vortex-antivortex pairs, coupled antiferromagnetic and structural domain walls, and multiferroic vortices (Chapter 5).

Chapter 6 on the theory of magnetoabsorption in Cu_2O was motivated by the experiment performed by the group of Paul van Loosdrecht at the University of Groningen. Cu_2O is the first semiconductor discovered, and also the first material in which excitons have been observed. However, after more than half-century of studies the interpretation of its magnetoabsorption spectra remains incomplete and there is no agreement about the number of excitonic states absorbing the light of different polarizations and the masses of holes and electrons. The group of Paul van Loosdrecht did high-resolution polarized magnetoabsorption measurements, which motivated the present theoretical study. We calculated the

excitonic energies in both high and low magnetic field regimes and derived the selection rules for excitons, which allowed us to fit the experimental spectra. We found out that two states with $n = 2$ have close energies and remained previously unresolved. This is an origin of the long-standing controversy over the number of excitonic levels and masses of charge carriers. The electron and hole masses extracted from our analysis of optical data are in agreement with results of cyclotron resonance measurements.

In the remainder of this chapter we briefly outline the main mechanisms leading to the emergence of non-collinear spin textures and the formalism useful to calculate magnon spectra and magnetization dynamics.

1.2 Classical spin models with non-collinear ground state

The Hubbard model [12] contains the essential ingredients to describe strongly-correlated materials: the hopping amplitude t_{ij} between the sites i and j and the on-site Coulomb repulsion U. The Hamiltonian of the model has the form:

$$\mathcal{H} = \sum_{i,j,\sigma} t_{i,j} c^\dagger_{i,\sigma} c_{j,\sigma} + U \sum_i n_{i\uparrow} n_{i\downarrow}, \tag{1.1}$$

where $c_{i,\sigma}$ annihilates the electron in the spin state σ on the site i, and $n_{i,\sigma} = c^\dagger_{i\sigma} c_{i\sigma}$. At half filling (one electron per site) the hopping term favors a metallic state, in which the system maximally gains kinetic energy, while the on-site Coulomb repulsion suppresses the polar states in which some sites are empty and some are doubly occupied. When the Hubbard U exceeds some critical value of the order of the electronic band width, the system becomes a Mott insulator with a charge gap and low-lying excitations in the spin sector described by the Heisenberg Hamiltonian [1]:

$$\mathcal{H} = \sum_{i,j} J_{i,j} \boldsymbol{S}_i \boldsymbol{S}_j, \tag{1.2}$$

where $\boldsymbol{S}_i = \frac{1}{2} c^\dagger_i \boldsymbol{\sigma} c_i$ is the operator of spin on the site i, and the exchange interaction, described by the constants $J_{i,j} = 4t^2_{i,j}/U$, results from the hopping of electrons to neighboring sites and back and the denominator U is the energy of an intermediate state with two electrons on the same site. In oxides the electrons hop between the metal ions through the oxygen orbitals, in which case the mechanism is called *superexchange* [14, 15].

[1] Important non-trivial effects in charge sector are also known, for a review see [13].

In real materials the situation is further complicated by the presence of many orbital states and several electrons on a single site, and by the Coulomb repulsion between electrons on neighboring sites. In oxides the exchange is usually mediated by the hopping of electrons from filled oxygen orbitals to the empty orbitals of neighboring metal ions (Fig. 1.1), lying higher in energy [15–17]. Alternatively, one can speak about the hopping of holes from transition metal ions to oxygen ions. If two metal-oxygen (M-O) bonds form the right angle, the holes from transition metal (TM) ions hop to the orthogonal p-orbitals and the energy is gained if those have parallel spins (due to the ferromagnetic Hund's rule coupling in the intermediate state). If the two M-O bonds form an angle close to 180°, the holes from TM ions hop to the same oxygen orbital, which is only allowed if their spins are opposite (Pauli principle). That gives rise to an antiferromagnetic exchange (see Fig. 1.1).

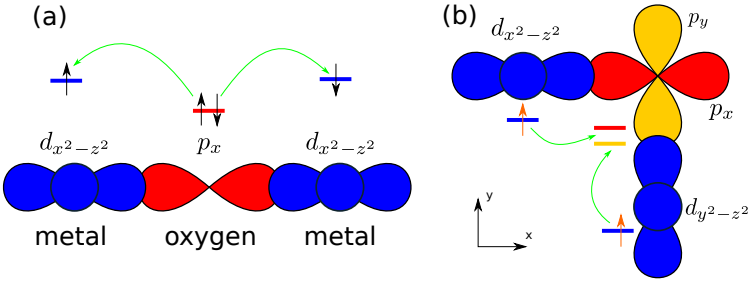

Figure 1.1: Anderson-Goodenough-Kanamori rules for the superexchange between half-filled orbitals. (a) For the 180° coordination the antiferromagnetic spin configuration enables a gain in kinetic energy due to the process, in which both electrons from an oxygen p-orbital hop to the neighboring metal ions (and then back). This is prohibited by Pauli principle for parallel spins on metal ions. (b) In the 90° coordination the holes from the magnetic ions could hop to the orthogonal oxygen 2p orbitals for both parallel and antiparallel spin configurations. However, the Coulomb energy of an intermediate state with parallel spins of two holes on oxygen ion is much lower (Hund's rule).

We now derive the *Dzyaloshinskii-Moriya antisymmetric exchange interaction* [18–20], playing an important role in the formation of chiral spin textures [21].

We first consider two magnetic ions with 2 orbital states on each of them (Fig. 1.2, orbitals $|\alpha\rangle$ and $|\beta\rangle$ on the first ion and $|\gamma\rangle$ and $|\delta\rangle$ on the second one). For simplicity, we will now ignore the second orbital of the second magnetic

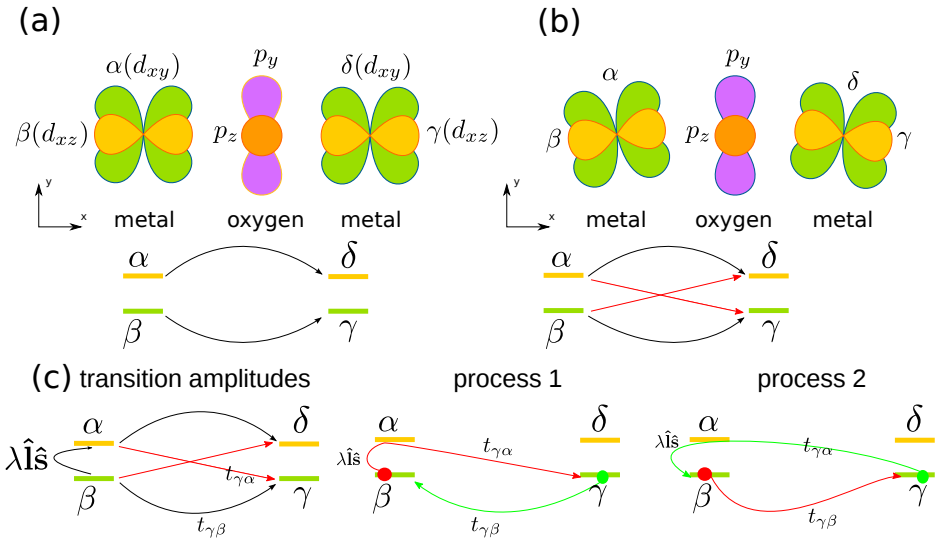

Figure 1.2: (a) 180° M-O-M configuration in which electrons only hop between the d orbitals marked by the same color. (b) The distorted configuration in which the hopping between the α and γ orbitals through the oxygen becomes possible. (c) possible hopping processes in the distorted configuration and transitions between the different orbitals on the same site due to the spin-orbit coupling. Two processes exchanging the electrons (time-conjugate to each other), giving rise to the antisymmetric exchange interaction.

ion and will include it into the consideration later. The Hamiltonian describing the on-site energies (ϵ-terms), the spin-orbit coupling (λ-term) and the hopping processes (t-terms) has the form:

$$\hat{H} = \epsilon_\alpha \hat{n}_\alpha + \epsilon_\beta(\hat{n}_\beta + \hat{n}_\gamma) + \lambda \hat{\mathbf{l}}\hat{\mathbf{s}} + (t_{\gamma\beta} \left|\beta\right\rangle \left\langle\gamma\right| + t_{\gamma\alpha} \left|\alpha\right\rangle \left\langle\gamma\right| + \text{H.c.}) \,.$$

We are interested in the contribution to the ground state energy, linear in the spin-orbit coupling λ. There are two different processes giving a desired contribution: in the process I the electron initially located on the left site (in the following referred to as "red electron") is promoted by the spin-orbit interaction to the state $|\alpha\rangle$, and then hops to $|\gamma\rangle$, while the "green" electron hops to the state $|\beta\rangle$:

$$\Delta E_1 = \hat{S}_{12} t_{\beta\gamma} \frac{1}{U} t_{\gamma\alpha} \frac{1}{\epsilon_\beta - \epsilon_\alpha} \lambda \mathbf{l}_{\alpha\beta} \mathbf{s_1},$$

where the spin-exchange operator $S_{12} = 2\boldsymbol{s}_1\boldsymbol{s}_2 + \frac{1}{2}$ takes care of the fact that

the exchange of the electrons leaves the triplet wave function invariant, while the singlet wave function changes sign. Indeed, starting with a triplet state (i.e. when both spins are up, or both are down, or $\uparrow_{\text{left}}\downarrow_{\text{right}} + \downarrow_{\text{left}}\uparrow_{\text{right}}$), and then exchanging the electrons by the process I, we obtain the initial state. But if we apply this operation to the singlet, $\uparrow_{\text{left}}\downarrow_{\text{right}} - \downarrow_{\text{left}}\uparrow_{\text{right}}$, we get $-\uparrow_{\text{left}}\downarrow_{\text{right}} + \downarrow_{\text{left}}\uparrow_{\text{right}}$, so the minus sign appears. This is taken into account by S_{12}, which has eigenvalue $+1$ for a triplet and -1 for a singlet state.

Complex conjugate of ΔE_1, corresponding to the process 2 in the Fig. 1.2, is

$$\Delta E_2 = \lambda \mathbf{l}^*_{\alpha\beta}\mathbf{s_1}\frac{1}{\epsilon_\beta - \epsilon_\alpha}t_{\gamma\alpha}\frac{1}{U}t_{\beta\gamma}\hat{S}_{12}$$

and together the two contributions add up to

$$\Delta E = \lambda \mathbf{l}_{\alpha\beta}\frac{1}{\epsilon_\beta - \epsilon_\alpha}t_{\gamma\alpha}\frac{1}{U}t_{\beta\gamma}(\hat{S}_{12}\hat{\mathbf{s}}_1 - \hat{\mathbf{s}}_1\hat{S}_{12})$$

since the wavefunctions of the crystal-field-split orbitals (transforming as $xy, yz, xz, x^2-y^2, 3z^2-r^2$) can be chosen real, and the matrix elements of $\boldsymbol{l} = [\boldsymbol{r} \times \frac{\hbar}{i}\boldsymbol{\nabla}]$ are then purely imaginary, so that $\boldsymbol{l}^*_{\alpha\beta} = -\boldsymbol{l}_{\beta\alpha}$.

The commutator in ΔE is easy to calculate:

$$(S_{12}s_1^b - s_1^b S_{12}) = [2s_1^a s_2^a, s_1^b] = 2[s_1^a, s_1^b]s_2^a = 2s_2^a i e_{abc} s_1^c = 2i[\boldsymbol{s}_1 \times \boldsymbol{s}_2]_b.$$

Finally we get

$$\Delta E = 2\lambda i \mathbf{l}_{\alpha\beta}\frac{1}{\epsilon_\beta - \epsilon_\alpha}t_{\gamma\alpha}\frac{1}{U}t_{\beta\gamma}[\boldsymbol{s}_1 \times \boldsymbol{s}_2].$$

Naturally, if the oxygen ion is located on the line connecting two magnetic ions, the hopping $t_{\gamma\alpha}$ is zero and $\Delta E = 0$. The Dzyaloshinskii-Moriya interaction between two magnetic ions is non-zero even if the spin-orbit coupling constant on one of the ions is zero. The inclusion of δ orbital gives an additional factor of 2 in ΔE.

To summarize, we considered the first-order correction in the spin-orbit interaction to the exchange between two TM ions mediated by the oxygen ion. The interaction energy involves the vector product of spins of the TM ions:

$$\mathcal{H}_{DM} = \boldsymbol{D}_{ij}[\boldsymbol{S}_i \times \boldsymbol{S}_j]. \tag{1.3}$$

This interaction favors the 90° angle between the spins and thus competes with the (usually stronger) superexchange interaction.

1.2.1 Frustrated J_1-J_2 exchange interactions

We now discuss a quasi-one dimensional material made of ferromagnetically coupled chains. The exchange interactions in the chain (see Fig. 1.3) are described by the Hamiltonian:

$$\mathcal{H} = \sum_n \left(J_1 \boldsymbol{S}_n \boldsymbol{S}_{n+1} + J_2 \boldsymbol{S}_n \boldsymbol{S}_{n+2} \right). \tag{1.4}$$

Here the nearest-neighbor exchange J_1 competes with an antiferromagnetic next-nearest-neighbor exchange $J_2 > 0$. The classical ground state of this model is

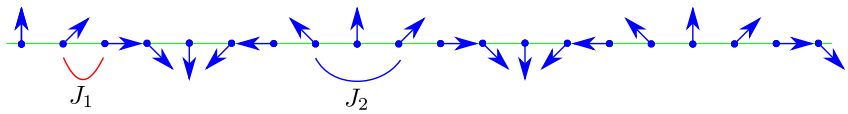

Figure 1.3: The magnetic spiral ordering in the chain of quasi-1D $J_1 - J_2$ magnet

ferromagnetic for $J_1 < -4J_2$, antiferromagnetic for $J_1 > 4J_2$ and otherwise a spiral $\boldsymbol{S}_n = (\cos qn, \sin qn)$ with the wavevector $q = \arccos\left(-\frac{J_1}{4J_2}\right)$, and the spiral plane is determined by the anisotropy. This mechanism is responsible for the magnetic spiral ordering in perovskite manganites [22]. Period of spirals induced by competing exchange interactions is a few unit cells.

1.2.2 Frustration by Dzyaloshinskii-Moriya exchange

If all the oxygen ions shift in the same direction from the line connecting TM ions, the Dzyaloshinskii vectors on all bonds $\boldsymbol{D}_{ij}$ are parallel, and the model Hamiltonian is

$$\mathcal{H} = \sum_n \left(J_1 \boldsymbol{S}_n \boldsymbol{S}_{n+1} + \boldsymbol{D} \cdot [\boldsymbol{S}_n \times \boldsymbol{S}_{n+1}] \right).$$

The minimization leads to the spiral state with the wavevector $q = \arctan(D/J)$. If the shifts of oxygen ions are alternating, the weak ferromagnetic state is induced [23], with the magnetization proportional to D/J (see Fig. 1.4).

The inverse Dzyaloshinskii-Moriya effect is also observed: if the magnetic spiral state is stabilized by $J_1 - J_2$ interactions, the system can further gain energy on the DM interaction by shifting the oxygen ions from the line, connecting metal ions. That gives rise to an electric polarization [24, 6].

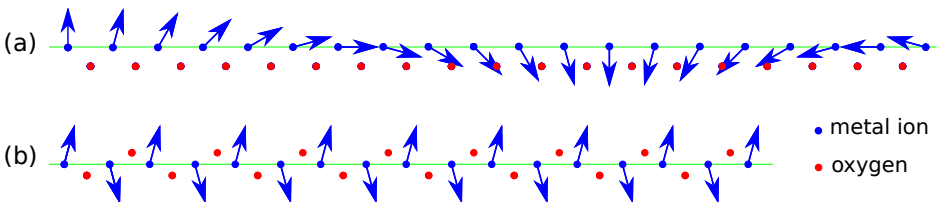

Figure 1.4: (a) The shift of all oxygen ions in the same direction from the M-M line leads to the Dzyaloshinskii-Moriya interaction stabilizing the magnetic spiral state. (b) Alternating shifts of oxygen ions from the M-M line lead to weak ferromagnetism.

1.3 Magnons

Magnetic excitations are very important because they determine the response of the system to external magnetic fields. Here we outline the basic notions related to magnon spectra of classical spin systems. The magnon spectrum of the classical spin system described by the Hamiltonian

$$\mathcal{H} = \sum_{i,j} \left(J_{i,j} \boldsymbol{S}_i \boldsymbol{S}_j + K_z S_{i,z}^2 \right),$$

where the last term describes a hard z-axis anisotropy, is most simply obtained within the Lagrangian formalism. In spherical coordinates $\boldsymbol{S}_i(\theta_i, \phi_i)$ ($|\boldsymbol{S}_i| = 1$) the Lagrangian is [25]

$$\mathcal{L} = \sum_i \dot{\phi}_i \cos\theta_i - \mathcal{H}, \tag{1.5}$$

and for a planar ground state spin configuration with spins perpendicular to the z axis, we describe the spin directions by the spherical angles $\theta_i = \pi/2 - \alpha_i$, $\phi_i = \phi_{i,0} + \beta_i$, where the index 0 denotes the ground state configuration. In these variables the Lagrangian is given by $\mathcal{L} = \sum_i \dot{\beta}_i \alpha_i - \mathcal{H}$, where the Heisenberg part of the Hamiltonian $\mathcal{H}$ takes a very simple form (the unit vector in the direction of the spin $\boldsymbol{n}_i$ has the spherical coordinates $(\theta_i = \pi/2, \phi_{i,0})$, and $\boldsymbol{\tau}_i = \partial \boldsymbol{n}/\partial\phi$ is

the tangent vector in the xy plane):

$$\sum_{i,j} \boldsymbol{S}_i \boldsymbol{S}_j \approx \sum_{i,j} J_{i,j} \left(\left[1 - \frac{1}{2}(\alpha_i^2 + \beta_i^2) \right] \boldsymbol{n}_i + \hat{z}\alpha_i + \boldsymbol{\tau}_i \beta_i \right) \times \left(\left[1 - \frac{1}{2}(\alpha_j^2 + \beta_j^2) \right] \boldsymbol{n}_j + \hat{z}\alpha_j + \boldsymbol{\tau}_j \beta_j \right) \approx \sum_{i,j} J_{i,j} \left[\boldsymbol{n}_i \cdot \boldsymbol{n}_j (\beta_i \beta_j - \frac{1}{2}(\alpha_i^2 + \beta_i^2 + \alpha_j^2 + \beta_j^2)) + \alpha_i \alpha_j \right]. \quad (1.6)$$

In the previous expression the $\approx$ sign means equality of the terms quadratic in small α, β, describing the spin deviations in a single-magnon state from the ground state. The terms of higher orders in α, β describe interactions between magnons and are beyond the spin-wave approximation, while the linear terms are zero because the state described by $\phi_{i,0}$ corresponds to the energy minimum.

The Euler-Lagrange equations are then simply

$$\begin{cases} \dot{\alpha}_i = \sum_j J_{i,j} \boldsymbol{n}_i \boldsymbol{n}_j (\beta_i - \beta_j), \\ \dot{\beta}_i = \sum_j J_{i,j} [\alpha_j - \alpha_i \boldsymbol{n}_i \boldsymbol{n}_j] + 2K_z \alpha_i. \end{cases} \quad (1.7)$$

This gives the spectrum $\omega(q)$ for a chain with the nearest-neighbor ferromagnetic exchange constants $J_{i,i+1} = J < 0$:

$$\omega_q = 4 \left| J \sin \frac{q}{2} \right| \sqrt{\sin^2 \frac{q}{2} + \frac{K_z}{2|J|}},$$

while for antiferromagnetic exchange constants $J_{i,i+1} = J > 0$

$$\omega_q = 4 \left| J \sin \frac{q}{2} \right| \sqrt{\cos^2 \frac{q}{2} + \frac{K_z}{2J}}.$$

These two spectra are plotted in Fig. 1.5.

1.4 Dynamics of magnetization switching in ferromagnets

Here we discuss the domain wall motion, which is the essence of the switching process in bulk ferroic materials. An action for the ferromagnet ($J < 0$) with the

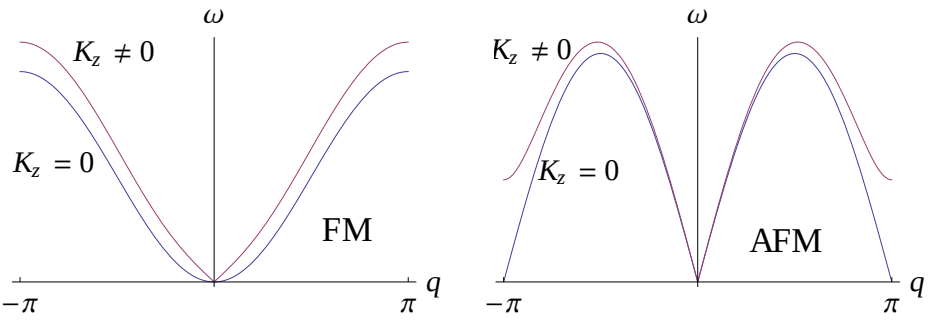

Figure 1.5: The magnon dispersion for easy-plane ferromagnetic and antiferromagnetic chains.

magnetization in the direction described by the spherical angles θ, ϕ, with the easy-z and hard-y anisotropy axes and subjected to the magnetic field $\boldsymbol{H} \parallel \boldsymbol{z}$ is:

$$A = \int dtdx \left(-\dot{\phi}\cos\theta - \left[J\left((\theta')^2 + \sin^2\theta(\phi')^2\right) - \frac{K_z}{2}\cos^2\theta + \frac{K_y}{2}\sin^2\theta\sin^2\phi - H\cos\theta \right] \right). \quad (1.8)$$

Here we assume that the magnetization does not change substantially on the scale of the lattice constant (smoothness of the spin texture) and thus limit ourselves with the quadratic terms in the gradient expansion. In the absence of a magnetic field domain walls do not move. Static domain wall has $\phi = 0$ and

$$A = -\int dtdx \left[J(\theta')^2 - \frac{K_z}{2}\cos^2\theta \right],$$

for which the Euler-Lagrange equation reads:

$$2J\theta'' = \frac{K_z}{2}\sin 2\theta.$$

Multiplying by θ' and integrating over x, we get:

$$J(\theta')^2 = -\frac{1}{4}K_z\cos 2\theta + C.$$

Using the boundary conditions, we find $C = K_z/4$, and

$$\int \frac{d\theta}{\sin\theta} = \log\left|\tan\frac{\theta}{2}\right| = \frac{x - x_0}{\lambda},\ \lambda = \sqrt{2J/K_z}. \quad (1.9)$$

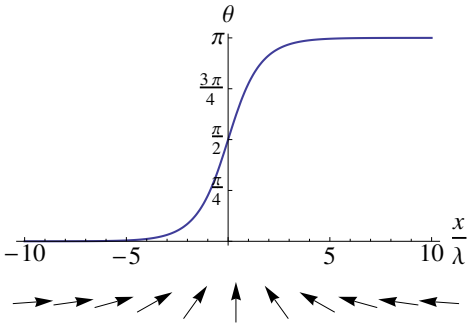

Figure 1.6: The shape of the static domain wall.

1.4.1 Domain wall motion in the magnetic field

In their seminal paper [26] Schryer and Walker derived equations of motion for a domain wall subjected to a magnetic field and identified exact solutions corresponding to a moving domain wall. These solutions have the form

$$\phi = const \quad \text{and} \quad \log\tan\frac{\theta}{2} = \frac{x - vt}{\lambda}. \tag{1.10}$$

Here we derive the equations of motion assuming that a weak magnetic field does not significantly change the shape of a domain wall. Physically, this assumption is justified by the fact that the energy of interaction with magnetic fields ~ 0.1 T is much smaller than the single-ion anisotropy and exchange energies, responsible for the domain wall shape (and magnetization switching is normally observed under much smaller fields). The lowest-energy magnon modes are the shift of the domain wall as a whole (it has zero energy, if we neglect the Pierls-Nabarro barrier), the tilt of spins out of the easy plane, and the distortion changing the width of the domain wall. We incorporate these modes into an ansatz $\theta(x,t) = 2\arctan e^{-\frac{x-r(t)}{\lambda}}, \phi(x,t) = \phi(t)$, which we substitute in Eq. (1.8). Performing the integration over x we get

$$A = 2\int dt \left(\hbar\dot{\phi}r - \frac{J}{\lambda} + \frac{\lambda K_z}{2} - Hr + \lambda K_y \sin^2\phi\right). \tag{1.11}$$

Varying Eq. (1.11) with respect to λ, we obtain:

$$\lambda = \sqrt{-\frac{2J}{K_z + 2K_y\sin^2\phi}}, \tag{1.12}$$

which coincides with Eq. (1.9) for $\phi = 0$. To account for the spin relaxation we introduce the dissipation functional, describing the enthropy production rate,

$$R = \frac{\hbar\alpha}{2}\int dtdx(\dot{\boldsymbol{S}})^2 = \hbar\alpha\int dt\left(\frac{(\dot{r})^2}{\lambda} + \lambda(\dot{\phi})^2\right). \tag{1.13}$$

The equations of motion have the form

$$\frac{\delta A}{\delta\nu} = \frac{\delta R}{\delta\dot{\nu}},$$

where ν runs over x, ϕ and λ. Since R does not depend on $\dot{\lambda}$, Eq. (1.12) is not changed by taking the dissipation into account. Equations for x and ϕ are:

$$\begin{aligned}\hbar\dot{\phi} - \frac{\hbar\alpha}{\lambda}\dot{r} &= H,\\ \hbar\alpha\dot{\phi} + \frac{\hbar}{\lambda}\dot{r} &= K_y\sin 2\phi\end{aligned}$$

They can be written in the form

$$\begin{cases}(1+\alpha^2)\hbar\dot{\phi} = H + \alpha K_y\sin 2\phi,\\ (1+\alpha^2)\dfrac{\hbar}{\lambda}\dot{r} = K_y\sin 2\phi - \alpha H.\end{cases} \tag{1.14}$$

The first equation has the form $(1+\alpha^2)\dot{\phi} = -\frac{dV(\phi)}{d\phi}$ and describes the overdamped motion of a massless particle with the coordinate ϕ in the potential $V(\phi) = -H\phi + \frac{\alpha K_y}{2}\cos 2\phi$ (Fig. 1.7).

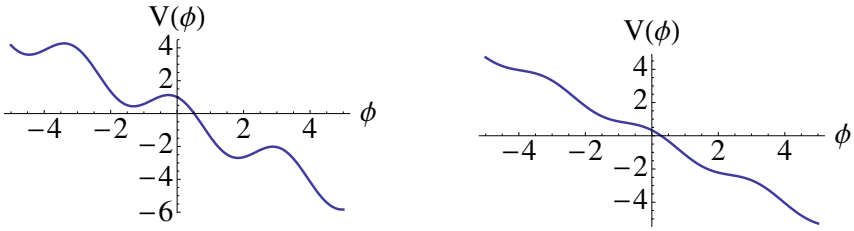

Figure 1.7: Equation of motion for a domain wall in a ferromagnet is analogous to Newton's equation describing a massless particle in the tilted washboard potential $V(\phi)$.

It has two different types of solutions:

1. For small fields, $H < \alpha K_y$, local minima of the potential exist (Fig. 1.7, left), and the particle is stuck in one of them, $\phi = const = -\frac{1}{2}\arcsin\frac{H}{\alpha K_y}$. Then from the second equation of (1.14) we find the DW velocity $\frac{\hbar}{\lambda}\dot{r} = H/\alpha$. This solution corresponds to the motion of the DW without changing shape.

2. In the opposite case, $H > \alpha K_y$, the force exerted on the particle $-\frac{dV}{d\phi} = H + \alpha K_y \sin 2\phi$ is always positive. In this case (Fig. 1.7, right) $\dot{\phi}$ is always positive and the particle keeps moving down the washboard. This solution describes an oscillatory domain wall motion with spin precession around the magnetic field direction. The transition to this regime is known as the Walker breakdown.

The dependence of an average DW velocity on the applied magnetic field is shown in Fig. 1.8.

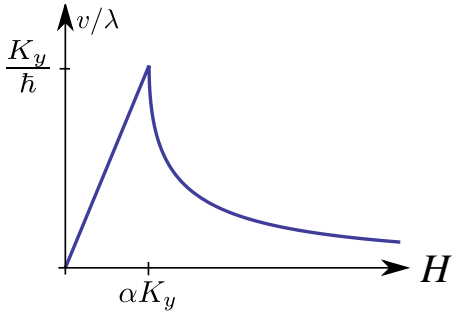

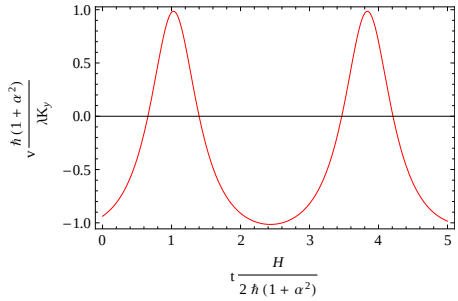

Figure 1.8: (left panel) The average domain wall velocity as a function of the magnetic field H. (right panel) The time dependence of the domain wall velocity in the Walker breakdown regime.

Chapter 2

Ferromagnetic Insulator State in Doped $FeTiO_3$

Abstract

The solid solution of two antiferromagnetic compounds, ilmenite and α-hematite $Fe_{1+x}Ti_{1-x}O_3$ exhibits an unusual insulating ferrimagnetic state appearing around room temperature. We show that Fe dopants in Ti layers induce large non-collinear modulations of spins in neighboring magnetic layers. We study spin polarons and their effect on magnetic properties of this material. Long-range interactions between the polarons suppress the antiferromagnetic order and lead to the ferromagnetic state.

A large magnetic moment of the polaron explains the superparamagnetic phase found experimentally at low doping. We consider effects of an applied magnetic field on the ferromagnetic polarons and show that the critical field at which the spin flop transition occurs goes down with the increase of x.

Non-isovalent doping introduces a hole bound to the dopant, which increases the ferromagnetic moment of the polaron via the double exchange. When the magnetic field is applied, the layer with spins along the field becomes more ferromagnetic, and the hole shifts to that layer in order to gain kinetic energy, thus producing an electric polarization. This leads to a magneto-electric effect.

2.1 Introduction

Dilute magnetic semiconductors (DMS) attracted much interest due to opportunities they offer for spintronics (for a review see [27, 28]) In the II-VI DMS the charge carriers, usually electrons, are provided by oxygen vacancies, acting as shallow donors [29, 30], whereas in III-V DMS the charge carriers (usually holes)

*Part of this work was performed in collaboration with Andrea Scaramucci and Andrei Berceanu.

are supplied by the magnetic impurities themselves. These charge carriers mediate the double exchange between the localized spins, which induces ferromagnetic regions — bound *magnetic polarons* — around the dopants [31]. At some critical concentration of dopants polarons percolate and a long range ferromagnetic order sets in, while the charge gap closes [32, 33].

In this chapter we study a mechanism of ferromagnetic cluster formation, which does not require itinerant carriers, and is based on frustration of exchange interactions between localized spins resulting from doping. As a prototype material we consider Fe-doped ilmenite $FeTiO_3$ [34–42]. In contrast to doped manganites, $Fe_{1+x}Ti_{1-x}O_3$ remains insulating for all x, even when an antiferromagnetic state is replaced by a ferromagnetic one, suggesting that itinerant carriers play no important role in the formation of the ferromagnetic state.

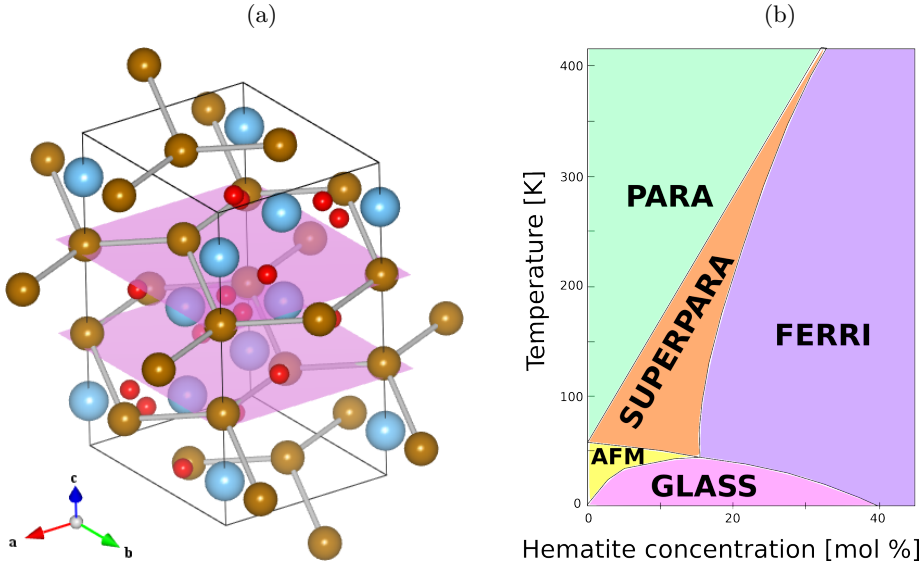

Figure 2.1: (a) The unit cell of ilmenite. Fe (brown) and Ti (blue) ions form buckled hexagonal layers. Oxygen ions are in red. (b) The magnetic phase diagram of $Fe_{1+x}Ti_{1-x}O_3$ solid solution reported in Ref. [36], showing the paramagnetic (PARA), superparamagnetic (SUPERPARA), ferrimagnetic (FERRI), antiferromagnetic (AF) and spin glass (GLASS) phases.

The ilmenite, $FeTiO_3$, has a corundum-type structure of alternating hexagonal layers of Fe and Ti ions with the Bernal stacking (see Fig. 2.1(a)). The Fe^{2+}

ion has the $3d^6$ ($s = 2$) electronic configuration, while Ti^{4+} with the empty d shell is nonmagnetic. The hematite Fe_2O_3 has a similar structure, but all the Ti ions are substituted by Fe ions.

The values of exchange constants in $FeTiO_3$ were found experimentally from inelastic neutron scattering data [43, 36]. Spins in neighboring Fe layers are antiparallel forming the A-type antiferromagnetic structure with Néel temperature of 60 K. The ferromagnetic in-plane exchange is an order of magnitude larger than the antiferromagnetic coupling between Fe layers separated by Ti layers. In the ground state spins in each plane are nearly parallel to the rhombohedral c-axis [43].

The α-hematite, Fe_2O_3, has a similar layered structure, in which all hexagonal planes are formed by Fe^{3+} ions. In this system the interlayer antiferromagnetic coupling is much stronger due to the roughly twice smaller distance between the adjacent magnetic layers. The ground state is of the up-down-down-up type with the much higher Néel temperature ($T_N = 950$ K) compared to ilmenite.

The Fe doping of ilmenite strongly affects its magnetic properties: at $x \approx 0.2$ a transition to a ferrimagnetic state was observed (see Fig. 2.1(b)) [34, 44]. Remarkably, at smaller x the magnetic susceptibility has a superparamagnetic behavior [45]: a Curie law-like paramagnetic susceptibility, but for very large spins. This effect was attributed to the formation of ferromagnetic clusters around the impurities [45]. It was concluded that the experimental results cannot be explained by the presence of ferromagnetic clusters of one certain size, and that a distribution of cluster sizes is required. The cluster size distribution was found to have peaks around clusters of 57 and 11 formula units of $FeTiO_3$. Similar superparamagnetic behavior was also found in Zn-doped $NiFe_2O_4$ [46] and some other materials (a review can be found in Ref. [35]).

In Ref. [45] it was suggested, that the strong antiferromagnetic exchange between the impurity and neighboring layers aligns spins in adjacent layers, giving rise to the superparamagnetic behavior. The transition to the ferrimagnetic state is attributed to the percolation of these clusters. This is similar to the ferromagnetic transition in oxide-based DMS, where percolation of bound magnetic polarons leads to ferromagnetic state [47].

This chapter is organized as follows: In Sec. 2.2 we present a simplified model of the Fe-doped ilmenite and study its ground state for the case of low doping. In the Sec. 2.3 we study interactions between impurities, describe the antiferromagnetic-to-ferrimagnetic transition and obtain the phase diagram. In Sec. 2.4 we consider the effect of dilute impurities on the spin-flop transition. In

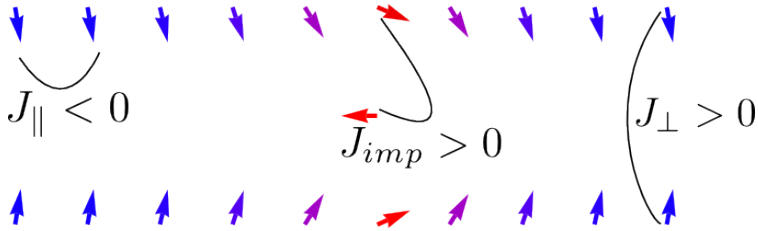

Figure 2.2: Exchange interactions in the single-dopant model. Antiferromagnetic interlayer interactions result in the A-type AFM ordering. The AFM interactions of the impurity with the neighboring spins frustrate interlayer interactions and align the spins in different layers ferromagnetically (spin directions are shown by arrows).

the Sec. 2.5 we study the polaron magnetoelectric effect.

2.2 Single impurity: the model and the ground state

In the solid solution of ilmenite and α-hematite some of Ti ions are substituted by Fe ions. The strong antiferromagnetic exchange between the iron impurity and Fe ions in the adjacent magnetic layers aligns the latter spins parallel to each other, thus frustrating the antiferromagnetic ordering. First we consider a single Fe impurity in a Ti layer sandwiched between two magnetic layers (see Fig. 2.2). The model Hamiltonian has the form:

$$\mathcal{H} = \sum_{\langle \mathbf{r},\mathbf{r}'\rangle,\lambda} J_{\|}\mathbf{S}_{\mathbf{r},\lambda}\cdot\mathbf{S}_{\mathbf{r}',\lambda} + \sum_{\mathbf{r}} J_{\perp}\mathbf{S}_{\mathbf{r},+1}\cdot\mathbf{S}_{\mathbf{r},-1} + \sum_{\lambda} J_{imp}\mathbf{S}_{imp}\cdot\mathbf{S}_{0,\lambda} \qquad (2.1)$$

where $\mathbf{S}_{\mathbf{r},\lambda}$ is a spin in the upper (lower) layer $\lambda = 1$ ($\lambda = -1$) at the position $\mathbf{r}$ on the square lattice. We consider a ferromagnetic nearest-neighbor exchange within the layers ($J_{\|} < 0$, the summation in the first term runs over the bonds connecting nearest neighbor sites in the same layer), an antiferromagnetic exchange between the layers ($J_{\perp}$) and an antiferromagnetic exchange between the impurity and the nearest Fe neighbors (J_{imp}). We assume that $J_{\perp} \ll |J_{\|}| \ll J_{imp}$.

Far from the impurity, the antiferromagnetic interaction between the two Fe layers, described by the second term ($J_{\perp} > 0$), favors an antiparallel alignment

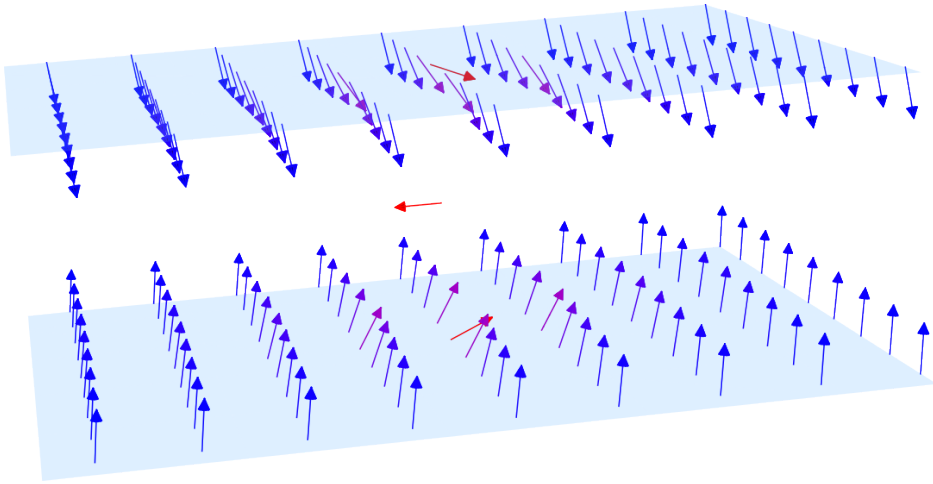

Figure 2.3: The ground state spin configuration around the Fe dopant. The color encodes the deviations of spins from the z axis.

of spins in neighboring Fe layers. On the other hand, large antiferromagnetic exchange with the dopant (J_{imp}) forces spins right above and below to align parallel to each other. In our model we assume that the Fe impurity in the Ti layer interacts with the same exchange constant J_{imp} with spins above and below. In $FeTiO_3$ this is not the case due to the layer stacking. The implications of this assumption for the realistic material are discussed below. In this section we also disregard the fact that the substitution of Fe for Ti changes valency of Fe ions and dopes the system with holes.

As a result of substitution of Ti by Fe, the A-type antiferromagnetic texture is deformed and a non-collinear spin configuration appears around the Fe dopant (see Fig. 2.2,2.3). Both layers are deformed equally, making the impurity spin to point perpendicular to spins at infinity. (For a rigorous proof that in the ground state configuration the deformation is distributed equally between the layers see appendix 2.7.) In the following we use the orthogonal coordinate system with the z axis aligned with the rhombohedral c axis (easy axis) and the x axis aligned with the impurity spin. The ground state configuration is coplanar, since the energy of any noncoplanar configuration with axially symmetric boundary conditions at $r \to \infty$ can always be decreased by rotating spins around the z axis to the xz plane (see Appendix 2.7).

The ground state can be described by the inclination angle $\theta_{\mathbf{r}}$ between the

spin $\mathbf{S_r}$ at the point $\mathbf{r}$ in the upper layer and the z axis. Then the spin in the lower layer has the inclination angle $\pi - \theta_{\mathbf{r}}$. The energy takes the form

$$H = J_{\parallel} S^2 \sum_{\langle \mathbf{r}\mathbf{r}' \rangle} 2\cos(\theta_{\mathbf{r}} - \theta_{\mathbf{r}'}) - J_{\perp} S^2 \sum_{\mathbf{r}} \cos(2\theta_{\mathbf{r}}) + 2J_{imp} S^2 \sin\theta_0. \tag{2.2}$$

In the upper layer along the line from infinity to the impurity, the angle θ varies from π to $\pi/2$, and in the lower layer along the line from the impurity to infinity spins rotate further from $\pi/2$ to 0, leading to the π angle between the spins in different layers far from the impurity required to minimize the energy of the antiferromagnetic coupling between the layers (see Fig. 2.3).

Far from the dopant, where $\theta(r)$ varies slowly on the scale of the lattice constant, the discrete Hamiltonian Eq. (2.2) can be replaced by the continuous model:

$$E = \int d^2x \left[|J_{\parallel}| \left[(\partial_x \theta)^2 + (\partial_y \theta)^2 \right] - \frac{J_{\perp}}{a^2} \cos(2\theta) \right], \tag{2.3}$$

where a is the lattice constant. Varying the energy with respect to $\theta(\mathbf{r})$, we obtain the Euler-Largange equation

$$\frac{J_{\perp}}{a^2} \sin 2\theta = |J_{\parallel}| \triangle \theta. \tag{2.4}$$

For small θ sine can be replaced by its argument and the solution of resulting two-dimensional Schrödinger equation is given by the Macdonald function:

$$\theta(r) \sim K_0(r/r_0) \sim \frac{1}{\sqrt{r/r_0}} e^{-r/r_0}, \tag{2.5}$$

where $r_0 = a\sqrt{\left|\frac{J_{\parallel}}{2J_{\perp}}\right|}$ is the polaron radius. Close to the core we solve the discrete problem numerically and match the solutions of the discrete and continuous models at $r = 20a \gg a$. The resulting spin configuration is shown in Fig. 2.4. It should be noted that the model (2.2) has continuous SO(2) rotational symmetry and so the lowest excitations are gapless Goldstone modes corresponding to a global spin rotation. Consequently, one could expect that the distortions of uniform ordering introduced by the impurity would decay in space according to a power law. This is not the case since the distortion introduced by the impurity involves an optical magnon mode, in which the spins in the neighboring layers cant in the opposite directions. The presence of the single-ion easy axis

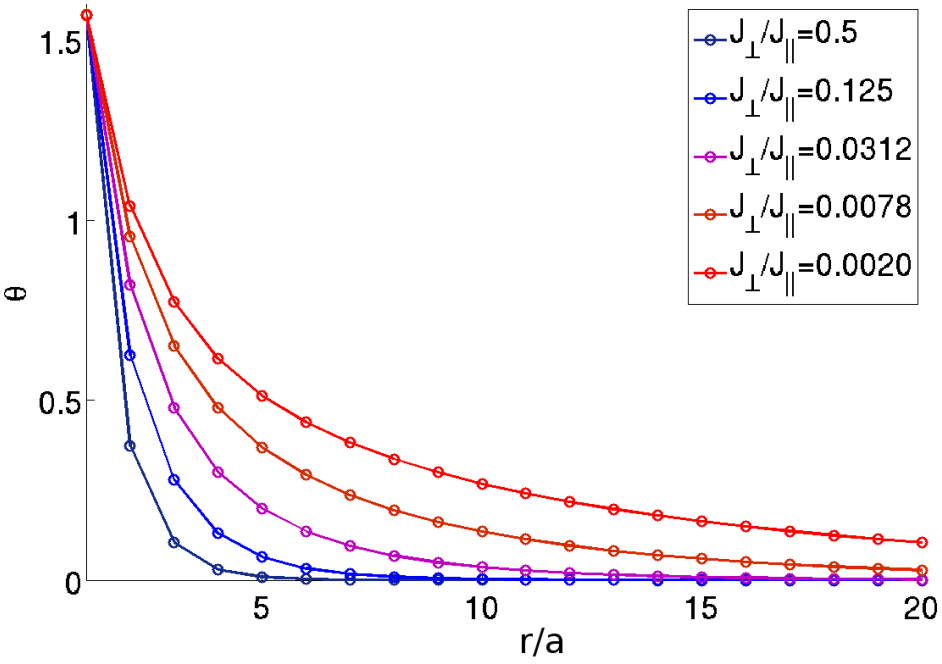

Figure 2.4: The dependence of the angle θ on the distance r from the impurity for a single spin polaron.

anisotropy also contributes to the term $\sim \theta$ in the r.h.s. of eq. (2.4), which makes the characteristic length scale r_0 smaller.

The important property of the polaron is a large in-plane magnetic moment $M_\parallel = \sum_{\mathbf{r},\lambda} S^x_{\mathbf{r}}$, which scales with r_0 approximately as $r_0^{1.8}$ (see Fig. 2.5). For small $r_0 \sim a$, $M_\parallel$ deviates from this scaling law due to the significant contribution from the polaron core. This in-plane magnetic moment can rotate freely around the easy axis, and is responsible for the superparamagnetic behavior. The large value of $M_\parallel$ is in quantitative agreement with the observed superparamagnetic effect [45] (see Sec. 2.3 for more details). The next-nearest-neighbor layers to the impurity are polarized by the spins in the nearest-neighbor layers due to the small antiferromagnetic interaction ($J_\perp$), and this polarization slightly reduces the total magnetic moment of the polaron.

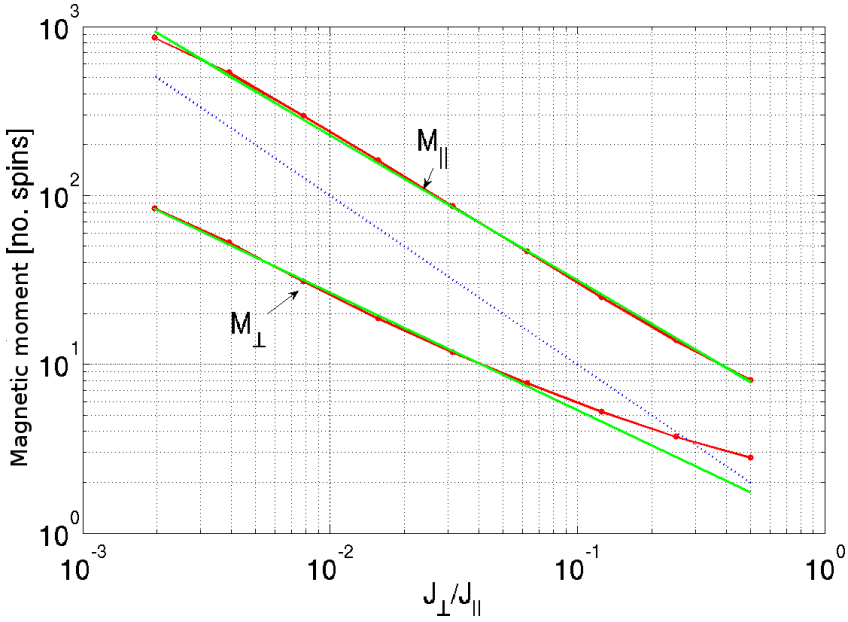

Figure 2.5: Parallel ($M_\parallel$) and staggered ($M_\perp = \sum_{\mathbf{r},\lambda} \lambda S^z_{\mathbf{r},\lambda}$) magnetic moment of spin polaron (red lines). Green lines are linear fit to red ones in the limit of small core contribution. Blue dotted line is $M \sim r_0^2$ for comparison. The results were obtained by numerical minimization of energy as described in the text.

2.3 Bulk properties

The multi-layered version of the model Eq. (2.1) with a finite concentration of Fe dopants in Ti layers was studied using Monte Carlo simulations to include the effect of thermal fluctuations. We simulated systems of six 10×10 Fe layers with open boundary conditions. We studied magnetic properties of the system when different numbers of impurities are placed between the layers, with averaging over a large number of impurity configurations. For this calculation we used the following model parameters: $J_{imp} = 6|J_\parallel|, J_\perp = 0.06 J_\parallel$ [36].

2.3.1 Superparamagnetic state at low doping

In the very dilute doping regime dopants are on average far from each other, and the overlap between different polarons is negligible. In this regime one can

consider polarons as non-interacting. The rotation of the in-plane magnetic moment of a polaron around the z-axis is a zero mode. At temperatures lower than the easy-axis anisotropy energy, the contribution of these modes (given by the expression for a gas of planar magnetic moments) dominates the magnetic susceptibility:

$$\chi = \frac{\pi n_{imp} M_p^2}{4 k_B T}, \tag{2.6}$$

where n_{imp} is the concentration of impurities. Monte Carlo simulations show that magnetic susceptibility at low doping follows this expression.

2.3.2 Interacting magnetic polarons, ferromagnetic state

As the doping is increased, the impurities get closer, and the distortions induced by adjacent impurities in ferromagnetic layers start to overlap. The energy gain due to the intralayer ferromagnetic exchange gives rise to an effective interaction between the spins of the impurities. Namely, the energy of a distortion induced by two impurities will be different from twice the energy of a single polaron, and will depend on the directions $\mathbf{m}_1, \mathbf{m}_2$ of their magnetizations, $E_2 = 2E_1 - J_{\text{eff}} \mathbf{m}_1 \mathbf{m}_2$. The effective interaction of two polarons can be evaluated using a simple model, in

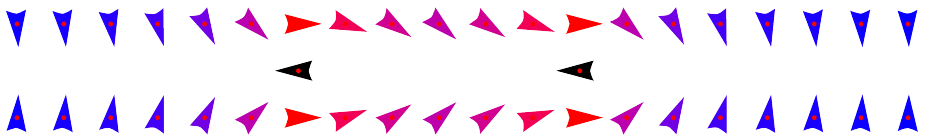

Figure 2.6: The deformations of AFM ordering mediate ferromagnetic interactions of overlapping polarons.

which the two impurity spins, $\mathbf{S}_1$ and $\mathbf{S}_2$, are sandwiched between ferromagnetic layers. The effective interaction, J_{eff}, can be found from the correlator of the two impurity spins:

$$\langle S_1 S_2 \rangle = \coth\left(\frac{J_{\text{eff}}}{T}\right) - \frac{T}{J_{\text{eff}}}. \tag{2.7}$$

Figure 2.7 shows the dependence of the effective interaction between two impurities on their distance obtained by Monte Carlo calculations at various temperatures. With the increase of the distance between the impurities, Δr, the overlap between the polarons decreases, causing exponential decay of the effective interaction. At the temperatures $T \sim J_{\parallel}$ thermal fluctuations of the polaron shape

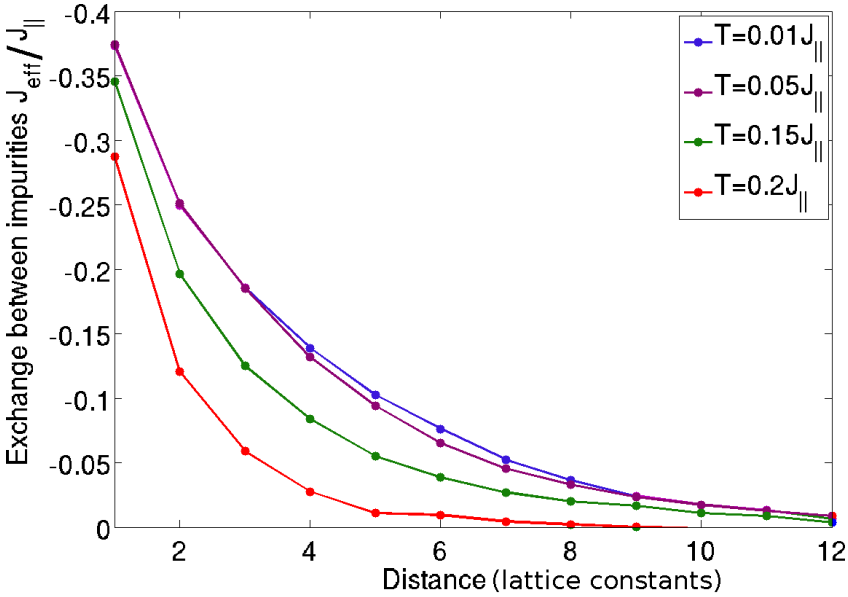

Figure 2.7: Effective interaction between impurities in the same Ti layer.

become important and reduce J_{eff}.
So far we neglected interactions between the polarons induced by impurities in different Ti layers. These interactions are included in the bulk Monte Carlo simulation. Figure 2.8 shows the dependence of the magnetization on doping calculated in the simulation. At low x the polarons in the antiferromagnetic matrix of ilmenite are uncorrelated and the total magnetization is zero. As the doping increases, the average distance between the polarons is reduced, polarons overlap more and interact stronger. At certain doping x_c these interactions give rise to the ferromagnetic ordering of the polaron magnetic moments, and a nonzero total magnetization emerges.

Upon further increase of doping, the total magnetization decreases linearly with x, since the newly introduced impurities align antiferromagnetically with the spins of Fe layers. Our simulation reproduced the experimental phase diagram, except for the spin glass phase. Study of kinetics in different phases, required to identify the spin glass state, is outside of the scope of this study.

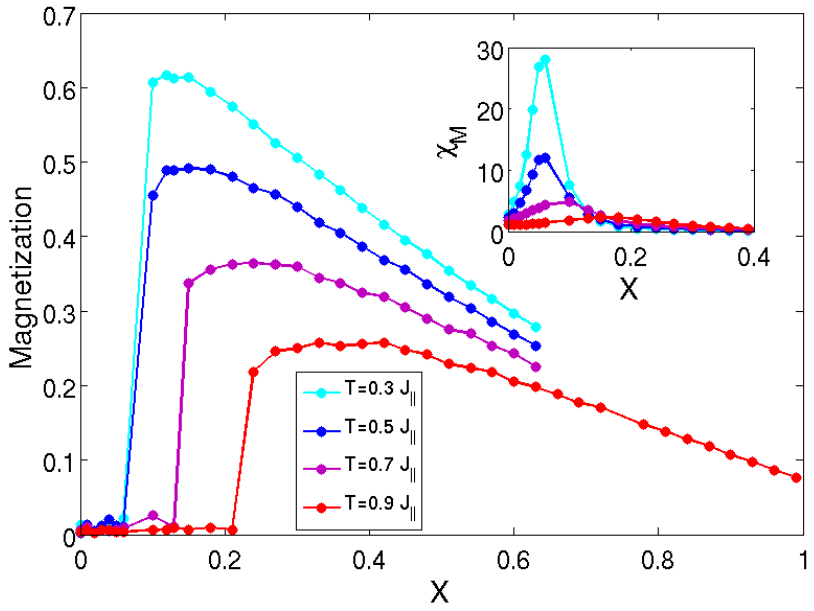

Figure 2.8: Magnetization and magnetic susceptibility (inset) as functions of doping x, as obtained from the Monte Carlo simulations. Courtesy of A. Scaramucci.

2.4 Polaron in magnetic field and spin flop transition

A characteristic feature of antiferromagnets subjected to magnetic field is a spin-flop transition. When an antiferromagnet with easy axis anisotropy is subjected to magnetic field along the easy axis, the magnetization stays nearly zero up to certain critical field, at which it suddenly jumps. This jump is a manifestation of a spin-flop transition and is related to the re-orientation of the antiferromagnetic moment perpendicularly to the easy axis, so that the spins can cant in the direction of the field and gain Zeeman energy. The $Fe_{1+x}Ti_{1-x}O_3$ has a non-zero magnetic moment perpendicular to the easy axis, which will be tilted towards the magnetic field applied along the easy axis. Therefore, at low fields the magnetization is expected to grow linearly with the field, in contrast with slower magnetization increase in the undoped system. Furthermore, in the antiferromagnets spin-flop is a result of competition between the Zeeman energy

(favoring the canted state) on one hand, and the anisotropy and exchange energy (favoring the collinear state) on the other. In $Fe_{1+x}Ti_{1-x}O_3$ the interaction of polaron magnetic moments with the field gives an additional energy gain proportional to the impurity concentration, thus shifting the balance towards the canted state. This is why the critical field for the spin-flop transition should decrease with the increase of doping. To obtain the quantitative predictions, we extend our model by adding a single-ion easy-z-axis anisotropy (term with Δ) and the Zeeman interaction with the external magnetic field $\mathbf{H}$,

$$\mathcal{H} = \sum_{\langle \mathbf{r},\mathbf{r}'\rangle,\lambda} J_{\parallel}\mathbf{S}_{\mathbf{r},\lambda}\cdot\mathbf{S}_{\mathbf{r}',\lambda} + \sum_{\mathbf{r}} J_{\perp}\mathbf{S}_{\mathbf{r},+1}\cdot\mathbf{S}_{\mathbf{r},-1} + \sum_{\lambda} J_{imp}\mathbf{S}_{imp}\cdot\mathbf{S}_{0,\lambda} - \Delta\sum_{\mathbf{r},\lambda}(S^z_{\mathbf{r},\lambda})^2 - \mathbf{H}\cdot\sum_{\mathbf{r},\lambda}\mathbf{S}_{r,\lambda}. \quad (2.8)$$

As mentioned above, in the undoped ilmenite the spin-flop transition is a result of competition of two states: antiferromagnetic state with spins parallel to the easy axis, and canted antiferromagnetic, with spins almost perpendicular to the easy axis. While in the former state system gains anisotropy energy, in the latter it gains energy due to the interaction with magnetic field (linearly in θ) while loosing on the antiferromagnetic exchange energy (quadratically in θ) and on anisotropy energy. The doping changes this energy balance: in the spin flopped state the system also gains energy on the interaction of the large polaronic magnetic moments with the magnetic field. This is the reason for the substantial decrease of the critical spin-flop field upon the doping (see Fig. 2.9).

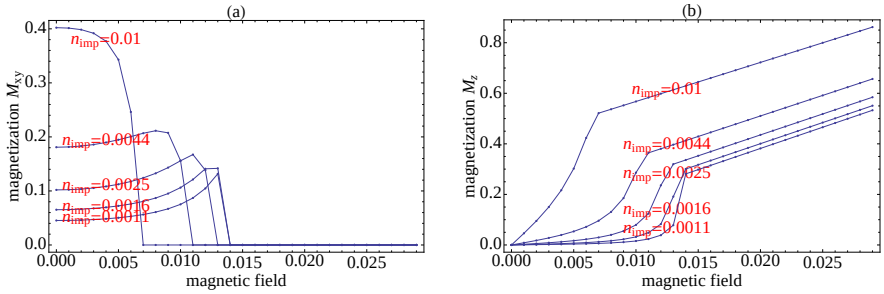

Figure 2.9: The spin-flop transition in the doped system at $T = 0$ calculated by energy minimization: dependence of the in-plane magnetization (M_{xy}, panel (a)) and the magnetization along the easy-axis (M_z, panel (b)) on the applied magnetic field.

Since the anisotropy constant Δ is of the order of $J_\perp$ [43], the polaron is significantly deformed at the spin-flop transition, which is why one should go beyond the rigid polaron approximation. Therefore, the spin-flop dependence of magnetization on the external magnetic field was calculated by numerical minimization of the energy (2.8). Fig. 2.9 shows the results, with deviations from the linearity being visible. In this calculation we used the model parameters $\Delta = 0.001, J_\parallel = -1.0, J_{imp} = 6.0$ and $J_\perp = 0.06$. Fig. 2.10(a) shows the deformation of the polaron in the magnetic field.

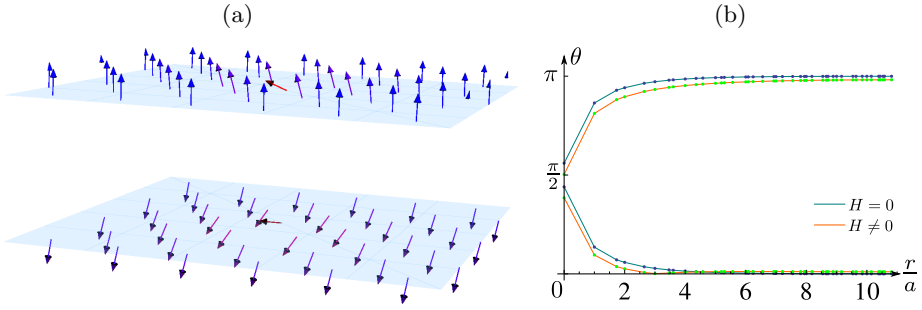

Figure 2.10: The spin polaron deformed by magnetic field $H = 0.15J_\parallel$ applied along the easy axis. (a) Arrows show spin directions. (b) Dependence of θ on the distance from the impurity. The calculation was done for $J_\perp = 0.1|J_\parallel|, K_z = 0.01|J_\parallel|$.

2.5 Non-isovalent doping: polaronic magnetoelectric effect

Non-isovalent doping introduces charge carriers (electrons or holes) bound to the dopant. In $Fe_{1+x}Ti_{1-x}O_3$ the substitution of Ti^{4+} by Fe leads nominally to the Fe^{4+} configuration of impurity with two additional holes compared to the Fe^{2+} ions in $FeTiO_3$. As we discussed in the previous section, magnetic field applied along the easy direction cants spins, rendering the polaron asymmetric. Now spins in one layer become slightly more ferromagnetic than in the other (see Fig. 2.10(b)). The hole density than shifts to the more ferromagnetic layer, where it gains kinetic energy due to hopping between the sites with parallel spins. Considerable spatial extent of the hole wave-function leads to large polarizability, making the polaron a promising candidate for observation of a polaron magneto-

electric effect. We now proceed to the quantitative description of this effect. The hole is bound to the dopant by a confining potential, which we model by a hydrogenic potential

$$\mathcal{H}_{\text{conf}} = \frac{Qe}{\epsilon|\mathbf{r} - \mathbf{e}_3/2|}, \tag{2.9}$$

where Q is an effective charge, $\mathbf{e}_3$ is a primitive translation vector in c direction, ϵ is electric permeability. The hole is able to delocalize over the neighboring Fe sites if an effective Bohr radius is larger than the lattice constant. We describe the interaction between the carrier and local Fe spins by means of the s-d model:

$$\mathcal{H}_{sd} = \sum_{\mathbf{r},\mathbf{r}',\sigma} t_{\mathbf{r},\mathbf{r}'} \psi^+_{\mathbf{r}\sigma} \psi_{\mathbf{r}'\sigma} + J_H \sum_{\mathbf{r},\sigma,\sigma'} \psi^+_{\mathbf{r}\sigma} \frac{1}{2} \boldsymbol{\sigma} \cdot \mathbf{S}_r \psi_{\mathbf{r}\sigma'} \tag{2.10}$$

where $t_{\mathbf{r},\mathbf{r}'}$ is the hopping amplitude, equal to t_{xy} between the nearest neighbors within the layer, and t_z for the hopping between the layers; $\psi_{\mathbf{r}\sigma}$ is a fermionic operator annihilating the hole with the spin σ at the site $\mathbf{r}$; σ is a vector of Pauli matrices, and $J_H > 0$ is the Hund's rule coupling for the holes. Since the Hund's rule coupling is generally large ($\sim$ eV), the electron tends to align its average spin on the site with the local spin on that site, while the hole spin tends to be opposite to the average on-site spin.

In the limit $|J_H| \to \infty$ only the state with the hole spin projection on local spin equal to minus one gets populated, the hole wave function is

$$\sum_{\mathbf{r}} \Psi_{\mathbf{r}} \cdot \begin{pmatrix} \sin \frac{\theta_{\mathbf{r}}}{2} \\ -\cos \frac{\theta_{\mathbf{r}}}{2} \end{pmatrix},$$

where $\theta_{\mathbf{r}}$ is defined in the paragraph above Eq. (2.2). The hopping term in Eq. (2.10) then takes the form $t_{\mathbf{r},\mathbf{r}'} \cos\left(\frac{\theta_{\mathbf{r}} - \theta'_{\mathbf{r}}}{2}\right) c^+_{\mathbf{r}} c_{\mathbf{r}'}$, where $c_{\mathbf{r}}$ annihilates the hole with the projection $-\frac{1}{2}$ along the average spin at the site $\mathbf{r}$. This essentially means that the hopping amplitude is reduced by the cosine of half angle between the local spins on the respective bond. Consequently, more energy is gained on bonds connecting sites with parallel local spins. Therefore the kinetic energy of the hole is minimized when the local spins in its localization region are aligned ferromagnetically. In the applied magnetic field one of the layers becomes more ferromagnetic than the other, therefore the electron density shifts towards this layer to gain on kinetic energy. This charge redistribution leads to electric polarization.

The results of numerical minimization of the energy for the model Eqs. (2.2),(2.10) under the applied magnetic field are shown in Fig. 2.11. We used the following model parameters: $J_H = 100|J_\parallel|$, $t_{xy} = 60|J_\parallel|$, $t_z = 40|J_\parallel|$, $Qe/\epsilon a = 50|J_\parallel|$.

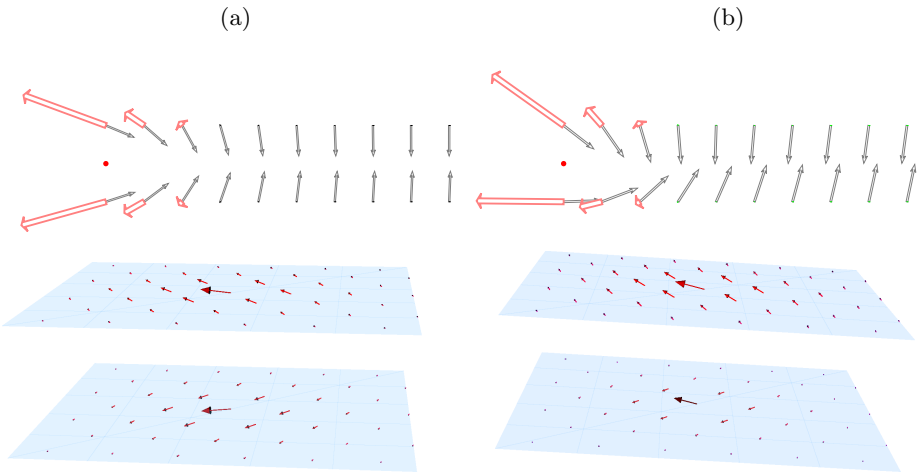

Figure 2.11: Ground state of the polaron. Gray arrows represent local spins; red dot marks the position of the impurity; red arrows (not to scale) correspond to the hole spin density. (a) $H_c = 0$. (b) In the applied magnetic field $H_c > 0$ upper layer becomes more ferromagnetic, and hole shifts there.

We minimize the energy in the first pass starting from the $H = 0$ state, and in the second pass - starting from the high-field (spin-flopped) state. Figure 2.12 shows the dependence of magnetization and polarization of the polaron on the magnetic field along the c direction. Sharp increase of magnetization at $H = H_{\mathrm{sf}}$ corresponds to the spin flop transition. At the same time the polarization drops to zero. For an estimate, if one could create the material with the Fe impurities only in odd Ti layers with the doping $x = 0.03$, magnetic field of 1 Oe would induce an electric polarization of $2 \cdot 10^{-6} \frac{\mu\mathrm{C}}{\mathrm{cm}^2}$.

2.6 Conclusions

To summarize, we proposed the model of layered antiferromagnets, frustrated by doping, which seems to capture the essential physics of the ilmenite-hematite solid solution. Within our model we studied the deformations in the antiferromagnetic ordering (magnetic polarons) induced by doping and the effect of the polarons on the magnetic properties of $Fe_{1+x}Ti_{1-x}O_3$. Large magnetization of spin polarons already at low doping results in a superparamagnetic behavior of

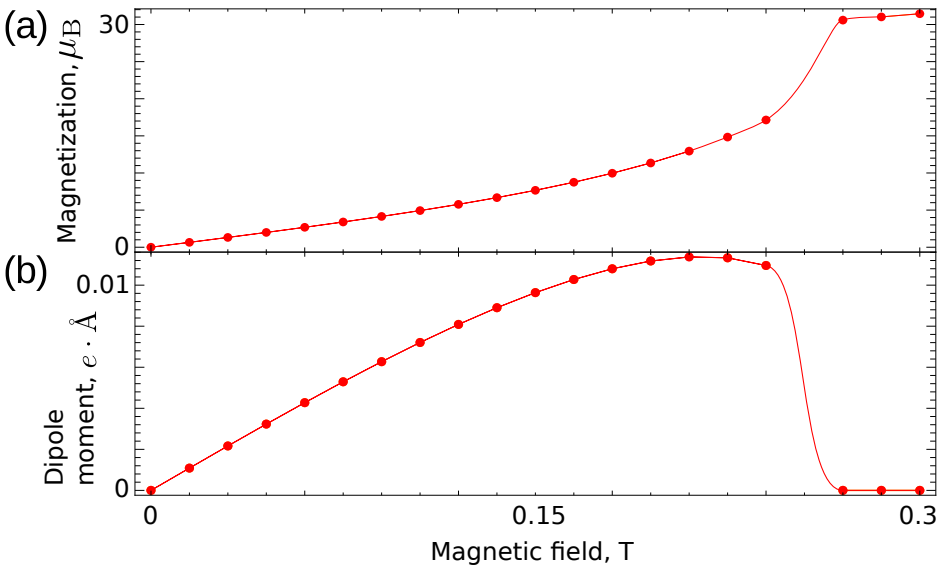

Figure 2.12: (a) Dependence of the magnetization of a supercell with a single polaron (for the 121 formula units supercell) on the magnetic field along the c direction, obtained by the numerical energy minimization. (b) Magnetoelectric effect: the dependence of the polaron dipole moment on the magnetic field in the c direction.

magnetic susceptibility. Upon further doping the overlap between neighboring polarons increases and the distortions of antiferromagnetic ordering they produce mediate ferromagnetic interactions between the magnetic moments of the polarons. At certain doping these interactions lead to the formation of the insulating ferromagnetic state. Our model calculations reproduce the experimental phase diagram, and we predict the anomalous spin-flop behavior and the spin-polaron magnetoelectric effect.

Our study has experimentally verifiable predictions concerning the dependence of the spin-flop field on doping. This seemingly easy experiment can unambiguously confirm the presence of polarons and allow for the direct measurement of their magnetic moment.

The polaron magnetoelectric effect is harder to measure since $FeTiO_3$ is centrosymmetric is present and so on average is $Fe_{1+x}Ti_{1-x}O_3$. In other words, the magnetoelectric effects of polarons formed around the impurities in the odd and

even Ti layers cancel each other. A net magnetoelectric effect could originate, for example, from the dimerization, resulting in different exchange constants $J_\perp$ through even and odd Ti layers (we have not yet found a suitable material). But even in the inversion-symmetric case the magnetoelectric effect of single polarons should lead to anomalies in magnetodielectric response.

2.7 Appendix I: symmetry of the ground state

Here we present a rigorous proof that under the conditions of the model Eq. (2.1) the deformations distribute symmetrically between two layers adjacent to the impurity.

Consider arbitrary spin configuration (a) with the spins at the $r \to \infty$ aligned along the easy axis. To prove the statement, we construct another configuration (b), where rotation is distributed equally between the layers and show that the energy of this configuration is always smaller or equal to the one of the configuration (a) (for symmetric configuration (a) the configuration (b) will be the same, and so their energies will be equal).

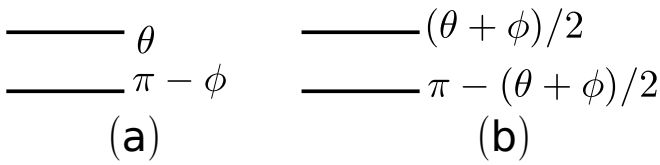

Figure 2.13: An arbitrary (a) and the symmetrized (b) configurations.

Energies of the two configurations are (vector δ connects nearest neighbors)

$$E_a = -J_\perp \sum_r \cos[\theta_r - (\pi - \phi_r)] - J_\parallel \sum_{r\delta} (\cos(\theta_r - \theta_{r+\delta}) + \cos(\phi_r - \phi_{r+\delta})) \quad (2.11)$$

$$E_b = -J_\perp \sum_r \cos\left[\frac{\theta_r + \phi_r}{2} - (\pi - \frac{\theta_r + \phi_r}{2})\right] - J_\parallel \sum_{r\delta} 2\cos\left(\frac{\theta_r + \phi_r}{2} - \frac{\theta_{r+\delta} + \phi_{r+\delta}}{2}\right) \quad (2.12)$$

The first sums in these two expressions are the same. The difference of energies

$$E_a - E_b = -J_{\parallel} \sum_{r\delta} \Bigg[\cos(\theta_r - \theta_{r+\delta}) + \cos(\phi_r - \phi_{r+\delta}) - 2\cos\left(\frac{\theta_r + \phi_r}{2} - \frac{\theta_{r+\delta} + \phi_{r+\delta}}{2}\right)\Bigg] = -J_{\parallel} \sum_{r\delta} 2\cos\left(\frac{\theta_r - \theta_{r+\delta} + \phi_r - \phi_{r+\delta}}{2}\right) \times \left[\cos\frac{\theta_r - \theta_{r+\delta} - (\phi_r - \phi_{r+\delta})}{2} - 1\right] \quad (2.13)$$

The term in the square brackets is always negative and the argument of the first cosine is a sum of partial rotations from 0 to π between the adjacent spins, which is smaller than the total rotation angle (equal to π), and so the argument of the cosine is smaller than $\pi/2$ making the cosine positive. So $E_1 - E_2 \geq 0$, meaning that the energy of the "symmetric" configuration (with rotation distributed equally between 2 layers) is always smaller.

Chapter 3

Large-period solitonic lattice in the rare earth orthoferrite $TbFeO_3$

Abstract

Magnetic phases of rare earth orthoferrites have been studied for more than four decades, in part because of the unique magneto-optical and magneto-acoustical properties of these materials [48, 49]. Here we study the recently discovered novel magnetic state in terbium orthoferrite observed by neutron diffraction under an applied magnetic field that had escaped previous scrutiny. This state has a very long period of $\sim 340\AA$ *incommensurate with the crystal lattice. The anomalously large number of observed higher-order harmonics allows us to identify this state with the periodic array of sharp domain walls in Tb spin ordering separated by many lattice constants. We discuss phenomenological and microscopic origins of this highly unconventional magnetic ordering and point at the mathematical equivalence between the coupled system of rare earth and transition metal spins and the theory of a massive scalar field that carries Yukawa-type interactions between extended charged objects.*

3.1 Introduction

Materials with magnetic transition metal and rare earth ions show a variety of spectacular effects originating from the coupling between the two spin subsystems. The transition metal spins interact stronger and order at higher temperatures than the spins of rare earth ions, but they are also much less anisotropic, which is why their orientation can be controlled by the rare earth magnetism.

*This study was motivated by the experimental discovery of the incommensurate phase in $TbFeO_3$ made in the group of D.N. Argyriou. The paper was submitted to Nature Materials, preprint: `http://arxiv.org/abs/1103.4275`.

Such re-orientation transitions, observed in many ferrites, chromites and manganites, have a profound effect on magnetic, optical and elastic properties of these materials [48–50].

More recently it was realized that interactions between transition metal and rare earth spins also play an important role in multiferroic and magnetoelectric materials [51–53]. Thus the coupling between the Mn spins forming a spiral state in the multiferroic $TbMnO_3$ and the Ising-like Tb spins leads to a significant enhancement of the electric polarization induced by the spiral [54, 55]. An order of magnitude larger polarization observed in the gadolinium orthoferrite, $GdFeO_3$, is induced by coexisting but independent magnetic orders of Fe and Gd magnetic sublattices, which together give rise to a polar lattice distortion [9], while in $DyFeO_3$ the same mechanism results in one of the strongest linear magnetoelectric responses observed in single-phase materials [56].

$TbFeO_3$ is an orthorhombic perovskite with Pbnm space group. Approximately at T_N(Fe)= 650 K G-type antiferromagnetic ordering of Fe spins with weak ferromagnetic component sets in (G_xF_z in Bertaut notation [57], see Fig. 3.1c). On cooling in zero magnetic field $TbFeO_3$ undergoes two successive transitions driven by Tb-Tb and Tb-Fe interactions [58, 59]. The ordering of Tb spins at T_N(Tb)$\sim$8.5 K appears simultaneously with a rotation of Fe spins in the ac plane, so that below 8.5 K both Fe and Tb spins have ferromagnetic components along the a axis, while their antiferromagnetic components are orthogonal to each other. The magnetic configuration of this intermediate temperature (IT) phase is F_xG_z, for Fe and $F'_xC'_y$, for Tb (see Fig. 3.1b). However, below $\sim$ 3 K there is another spin re-orientation transition, which flips the Fe order back to its high temperature G_xF_z order, while the Tb spins order antiferromagnetically in the $A'_xG'_y$ state (see Fig. 3.1a).

3.2 Experiment

Magnetic phases of $TbFeO_3$ were studied by the group of D. N. Argyriou at the Helmholtz Centrum (Berlin) using neutron diffraction under a magnetic field applied along the c axis. In zero magnetic field the sequence of the re-orientation and inverse re-orientation transitions, described above, is observed.

A series of field-cooled measurements was performed in various fields, while monitoring accessible A- and G-type reflections. In Fig. 3.2(a) the temperature dependence of scan along k around the A-type (001) reflection is shown. At high temperatures this reflection is absent as there is no order of an A-type

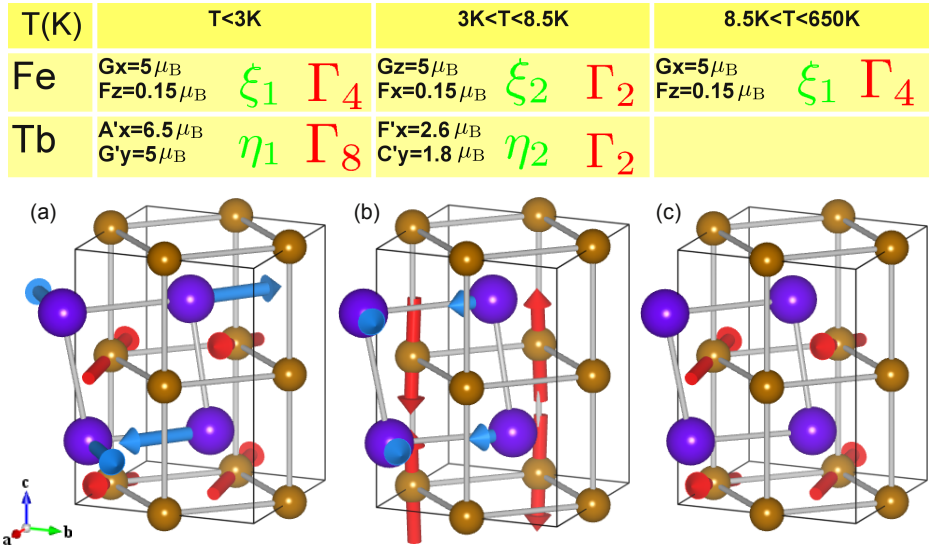

Figure 3.1: Magnetic ordering of Fe^{3+} (brown spheres) and Tb^{3+} (blue spheres) ions in the three uniform phases of $TbFeO_3$: the LT phase (panel a), the IT phase (panel b) and the HT phase (panel c). Also shown are the corresponding order parameters, irreducible representations and experimental values of magnetic moments [58]. The various types of magnetic order depicted here are labeled as F for a ferromagnetic ordering, G for a the two-sublattice antiferromagnetic Néel state, A for ferromagnetic *ab* planes stacked antiferromagnetically and C for ferromagnetic chains parallel to the *c* axis coupled antiferromagnetically.

component for either the Fe or Tb magnetic sublattice. However, on cooling a series of refections appears below 3.8 K, that merges into a single peak at 2.8 K. Examination of the wavevector of these reflections easily establishes that they are odd harmonics of up to 11th order, and the wavevector of the 1st harmonic is $\mathbf{Q} = (0, \epsilon, 1)$ with $\epsilon \sim 0.015$ r.l.u. [see Fig. 3.2(b)]. The width of these peaks gives the coherence length of ∼700 Å, and the incommensurate periodicity of approximately 67 units cells or 340 Å.

The physical significance of these observations is that the Tb magnetic order in h$\|c$ field develops a square-wave modulation – a periodic array of widely separated domain walls [1]. In the modulated A-state, Tb spins form ferromagnetic stripes

[1] here by *domain wall* we mean a kink in the order parameter appearing within a single modulated phase, rather than a real boundary separating two different domains.

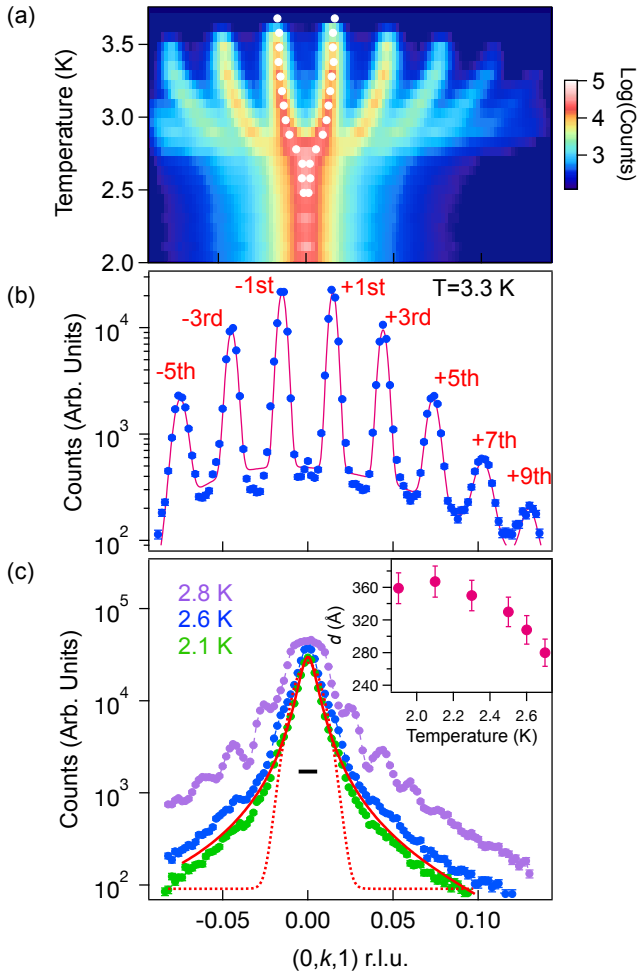

Figure 3.2: Single crystal neutron diffraction intensity measured along (0,k,1) in reciprocal space on cooling and in a magnetic field parallel to the c axis of h$\|c$ = 2 T . (a) Temperature-dependent neutron diffraction intensity. White circles are positions of the first harmonic reflection computed by fitting the diffraction data at each temperature to Gaussian peak profiles. (b) Neutron diffraction intensity measured at 3.3 K (blue dots) with the harmonics labeled. The continuous line is a fit of a sum of Gaussian peaks to the data. (c) Scans measured at 2.8, 2.6 and 2.1 K show the transition from the IC phase to the LT′ phase. At 2.8 K the various higher harmonic reflections are clearly evident, while at lower temperatures they merge together. At 2.1 K the diffraction peak is best approximated by a single Lorentzian peak (red continuous line). A Gaussian peak is shown as a dotted line for comparison while the horizontal black bar represents the resolution of the instrument. The inverse width of the Lorentzian peak corresponds to the average distance d between neighboring domain walls (see text). The temperature dependence of d determined from the lower temperature data is shown in the insert of panel (c).

in the *ab* planes with the width 170 Å along the *b* axis. The *a* component of magnetization alternates from stripe to stripe, while the stacking of spins along the *c* axis is antiferromagnetic. Investigation of an Fe G-type reflection under the same condition suggests that Fe-spins are weakly perturbed by this unusual Tb-order.

On cooling below 2.8 K Fig. 3.2(a) would indicate that the Tb modulation abruptly disappears and the Tb subsystem returns to the zero field state with the uniform $A'_xG'_y$ order. However, closer inspection of the diffraction data indicates that the (001) reflection on cooling does not yield a simple Gaussian peak shape but rather a Lorentzian one. Below, we argue that the Lorentzian peak shape

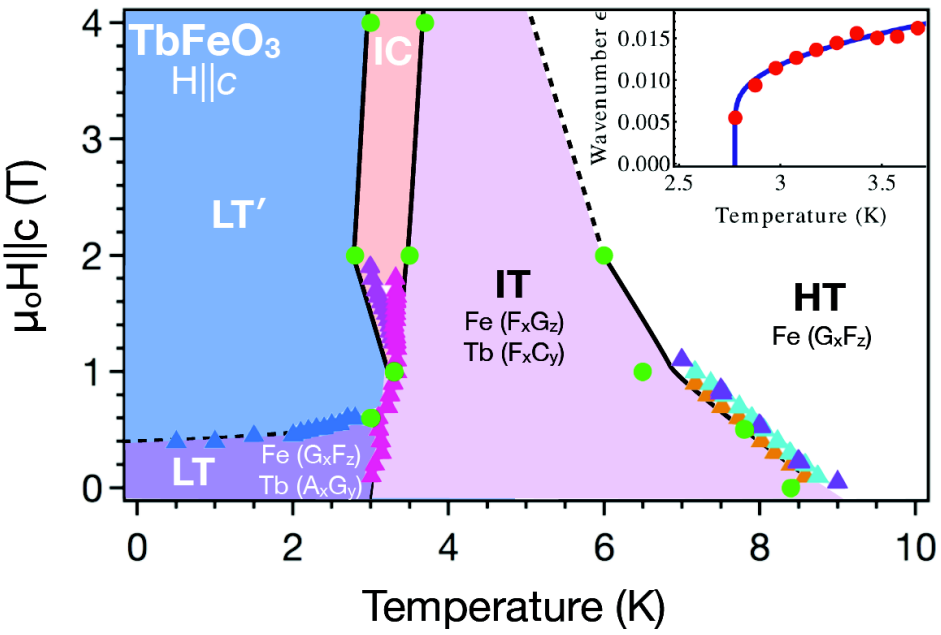

Figure 3.3: The magnetic phase diagram of $TbFeO_3$ determined from neutron diffraction data (shown as circles) and capacitance and loss measurements (shown as triangles) that are described in the supplementary information (see Fig. S2-S5). In the insert we show the temperature dependence of the modulation wavevector ϵ measured in an applied magnetic field $\mu_0 H_c = 2$ T. The blue line is the fit obtained using the theoretical description of the IC state in terms of the periodic kink array.

below 2.8 K is indicative of domain wall disordered phase that we refer to as LT′.

The transitions that are evident in the neutron data are correlated with anomalies in both the capacitance and loss data, which enabled us to construct the phase diagram shown in Fig. 3.3.

3.3 Theory

In this section we discuss the nature of interactions stabilizing such an unusual periodic domain wall array and holding the domain walls at large distances from each other. We start by formulating the phenomenological theory based on the symmetry of the crystal. Magnetic order parameters transform according to one-dimensional irreducible representations of the crystal symmetry group (see Table 3.1).

Well below $T_{\rm N}$(Fe)≈ 650 K the magnitude of the ordered antiferromagnetic moment of the Fe subsystem is independent of temperature, while its direction in the ac plane described by the angle θ can significantly vary due to the low magnetic anisotropy of the Fe^{3+} ions. In our notations $\xi_1 = \cos\theta$ is the order parameter of the G_x state (transforming according to Γ_4 irreducible representation, see Table 3.1), while $\xi_2 = \sin\theta$ (of Γ_2 symmetry) describes the G_z ordering. The free energy density of the Fe subsystem is

$$f_{\rm Fe} = \frac{c}{2}\left(\frac{d\theta}{dy}\right)^2 + \frac{K}{2}\sin^2\theta - h\cos\theta, \tag{3.1}$$

where the first term describes the exchange between Fe spins along the b axis, the second term is the magnetic anisotropy, which for $K > 0$ favors the G_x order, and the last term is the Zeeman interaction with the magnetic field H_z in the G_xF_z state.

The free energy of Tb spins is expanded in powers of the order parameters η_1, describing the zero phase LT state with antiparallel Tb spins in neighboring ab layers (Γ_8 symmetry, Fig. 3.1a), and η_2, describing the IT state with parallel Tb spins in neighboring layers (Γ_2 symmetry, Fig. 3.1b):

$$\begin{aligned} f_{\rm Tb} &= \frac{c_1}{2}\left(\frac{d\eta_1}{dy}\right)^2 + \frac{c_2}{2}\left(\frac{d\eta_2}{dy}\right)^2 + \frac{a_1}{2}\eta_1^2 + \frac{a_2}{2}\eta_2^2 \\ &+ \frac{b_1}{4}\eta_1^4 + \frac{b_{12}}{2}\eta_1^2\eta_2^2 + \frac{b_2}{4}\eta_2^4 + \ldots. \end{aligned} \tag{3.2}$$

For $\Delta = a_2 - a_1 > 0$ the Tb subsystem would order in the state with $\eta_1 \neq 0$ below some temperature T_0, at which $a_1 = 0$. However, the interaction between

	Fe	Tb	$\tilde{m}_x$	$\tilde{m}_y$	m_z
Γ_1	$A_xG_yC_z$	C'_z	+	+	+
Γ_2	$F_xC_yG_z$	$F'_xC'_y$	+	−	−
Γ_3	$C_xF_yA_z$	$C'_xF'_y$	−	+	−
Γ_4	$G_xA_yF_z$	F'_z	−	−	+
Γ_5		$G'_xA'_y$	−	−	−
Γ_6		A'_z	−	+	+
Γ_7		G'_z	+	−	+
Γ_8		$A'_xG'_y$	+	+	−

Table 3.1: Transformation properties of representations of Pbnm space group under the three generators of the group: the two glide mirrors, $\tilde{m}_x : (x, y, z) \to (1/2-x, 1/2+y, z)$ and $\tilde{m}_y : (x, y, z) \to (1/2+x, 1/2-y, 1/2+z)$, and the mirror $m_z : (x, y, z) \to (x, y, 1/2 - z)$.

the Tb and Fe spins favors the IT state with $\eta_2 \neq 0$ and $\theta = \pm\frac{\pi}{2}$, in which both subsystems have a ferromagnetic moment along the a axis. Since η_2 and $\xi_2 = \sin\theta$ transform in the same way (according to Γ_2 irreducible representation), this interaction is a linear coupling,

$$f_{\mathrm{Fe-Tb}} = -\lambda\xi_2\eta_2. \tag{3.3}$$

For $\lambda^2 > \Delta K$, the 'unnatural' IT state with parallel Tb spins in neighboring layers and Fe spins rotated by 90° away from the easy axis, intervenes between the states with the 'natural' orders of Fe and Tb spins. In this way one obtains the zero-field phase diagram of $TbFeO_3$ [58, 60].

In addition, we consider the so-called Lifshitz invariants linear in order parameter gradients of the form

$$\Gamma_8\partial_y\Gamma_2 - \Gamma_2\partial_y\Gamma_8, \tag{3.4}$$

or, more specifically,

$$f_{\mathrm{L}} = g_1\left(\eta_1\partial_y\xi_2 - \xi_2\partial_y\eta_1\right) + g_2\left(\eta_1\partial_y\eta_2 - \eta_2\partial_y\eta_1\right), \tag{3.5}$$

which favor the experimentally observed periodic spin modulation along the b axis. Similar terms inducing modulations along the a and c axes are forbidden by symmetry (see the supplemental material). Minimizing the total free energy

– the sum of Eqs.(3.1-3.5) – we obtain the phase diagram shown in Fig. 3.4a, which includes a narrow incommensurate phase region, which we identify with the IC phase revealed in our neutron data.

We note that the rotationally symmetric scalar products,

$$\mathbf{A}' \cdot \partial_y \mathbf{F} - \mathbf{F} \cdot \partial_y \mathbf{A}' \quad \text{and} \quad \mathbf{G}' \cdot \partial_y \mathbf{C} - \mathbf{C} \cdot \partial_y \mathbf{G}', \tag{3.6}$$

where e.g. $\mathbf{A}' \cdot \partial_y \mathbf{F} = A'_x \cdot \partial_y F_x + A'_y \cdot \partial_y F_y + A'_z \cdot \partial_y F_z$, are also invariant under all transformations of the Pbnm group showing that the coupling between inhomogeneous rare earth and transition metal magnetic orders can originate from Heisenberg exchange interactions [55].

It is important to stress the difference between the IC state in $TbFeO_3$ and the long period spin spirals in non-centrosymmetric magnets, also described using Lifshitz invariants [61]. First, the crystal lattice of $TbFeO_3$ is centrosymmetric (inversion symmetry is only broken in the LT phase by the Tb spin ordering). Equation (3.5) is the interaction between two distinct magnetic phases: the LT Tb state (odd under inversion) and the IT phase (even under inversion). It is only effective close to the boundary where these two phases have equal free energies, which is why the IC state is observed in a very narrow region of the phase diagram.

Second, spirals in non-centrosymmetric magnets result from the relatively weak spin-orbit coupling [61, 19]. On the other hand, the coupling Eq.(3.5) likely originates from a stronger Heisenberg exchange: in the supplemental material we give symmetry arguments showing that the exchange interactions between the Tb and Fe spin orders varying along the b axis do not cancel. Furthermore, the coupling between two Tb order parameters [the second term in Eq.(3.5)] resulting from interactions between rare earth spins separated by relatively long distances, is expected to be much weaker than interactions between the Tb and Fe spins described by the first term (in our calculations $g_2 = 0$).

Third and most important, the observation of the large number of Fourier harmonics in the IC state of $TbFeO_3$ shows that this state is qualitatively different from a magnetic spiral with slowly varying spin vectors. To account for the difference between the isotropic Fe spins and the Ising-like Tb spins [59, 62], we assumed that $c_1, c_2 \ll c$ and allowed for 40 harmonics in the periodic modulation of order parameters when we minimized the free energy. The resulting incommensurate state is shown in Fig. 3.4b. While the angle θ describing the Fe spins undergoes small amplitude fan-like oscillations around zero, corresponding to the oscillations of the weak ferromagnetic moment of Fe ions around the ap-

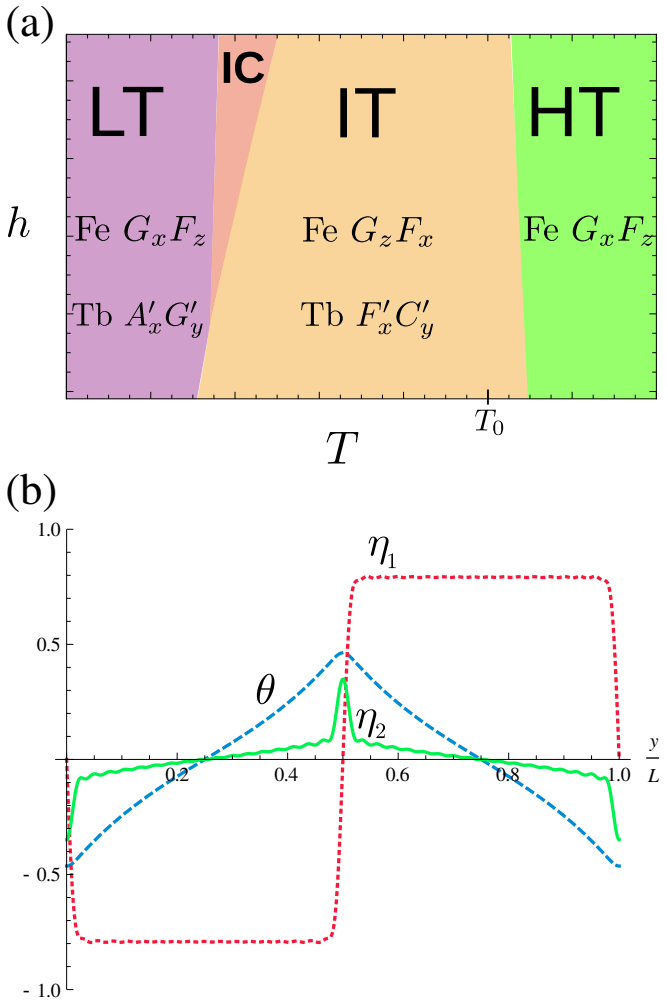

Figure 3.4: (a) Magnetic phase diagram of the Landau model of $TbFeO_3$ including the Fe-Tb interaction described by the Lifshitz invariants Eq.(3.5). The parameters used to obtain this phase diagram are: $\Delta = 0.5$, $K = 0.125$, $\lambda = 0.275$, $b_1 = b_2 = 1.0$, $b_{12} = 2.4$, $g_1 = 0.187$, $g_2 = 0$, $c = 1$, and $c_1 = c_2 = 0.01$. (b) The y-dependence of the Tb order parameters, η_1 (red line) and η_2 (green line), and the angle θ measured in radians (blue line) describing the fan-like rotation of Fe spins in the IC state with the period $L = 340$ Å.

plied magnetic field $H\|c$, the low-temperature Tb order parameter η_1 exhibits sudden jumps.

To understand the nature of the force that holds these atomically sharp domain walls at distances of $\sim$ 170 Å from each other, we (briefly) discuss an interesting field-theoretical interpretation of the coupled system of rare earth and transition metal spins. Consider a single domain wall located at $y = 0$ where the Ising-like LT order parameter η_1 shows a discontinuous jump from $-|\eta_1|$ to $+|\eta_1|$ or vice versa (see Fig. 3.5a). Such a kink can be assigned the topological charge $Q = (\eta_1(+\infty) - \eta_1(-\infty))/2|\eta_1| = \pm 1$. The free energy per unit area of the domain wall is the 'bare' energy $F_{DW}^{(0)}$ resulting from interactions between Tb spins plus

$$F_\theta = -2g\theta(0)Q + \frac{1}{2}\int dy \left[c\left(\frac{d\theta}{dy}\right)^2 + (K+h)\,\theta^2 \right], \tag{3.7}$$

where the first term is the Lifshitz invariant Eq.(3.5) ($g = 2g_1|\eta_1|$ and $g_2 = 0$), describing the interaction between the Tb and Fe spins, while the second term is the free energy of Fe spins for $|\theta| \ll 1$. Equation (3.7) can be interpreted as an energy of a charged plane with the surface charge density gQ interacting with the field θ, which describes spin waves in the Fe magnetic subsystem. Minimizing F_θ with respect to $\theta(y)$, we obtain the distortion in the Fe spin ordering produced by the Tb domain wall, $\theta(y) = \frac{Qg}{\sqrt{c(K+h)}} e^{-\frac{|y|}{l}}$ (see Fig. 3.5a), which reduces the domain wall free energy:

$$F_{DW} = F_{DW}^{(0)} - \frac{g^2}{\sqrt{c(K+h)}}. \tag{3.8}$$

When F_{DW} becomes negative, the domain walls tend to condense. Their density is, however, limited by the effective long range repulsion between the domain walls resulting from the exchange of magnons. This interaction is analogous to the pion-mediated Yukawa force between protons and neutrons in nuclei [63]. The sharp domain walls in the Tb spin subsystem play the role of nucleons, while magnons propagating through the Fe spin subsystem play the role of massive pions. The analog of the pion mass is a small gap in the magnon spectrum, which limits the range of this interaction by the length $l = \sqrt{\frac{c}{K+h}}$, much larger than the lattice constant. This Yukawa-like force attracts equal 'electric' charges and repels opposite ones. Since the topological charges of domain walls alternate along the b axis, neighboring domain walls in a periodic array have opposite 'electric' charges, resulting in net repulsion. The interaction between two neighboring

domain walls located at y_1 and y_2 [see Fig. 3.5(b)] is

$$U(y_2 - y_1) = \frac{g^2}{\sqrt{c(K+h)}} e^{-\frac{|y_2 - y_1|}{l}}, \tag{3.9}$$

and the total 'electrostatic' free energy of an array of domain walls with the charges $\{Q_n\}$ alternating along the b axis (including the 'self-energy' of the charged surfaces) is given by

$$F_\theta = -\sum_{n,m} Q_n U(y_n - y_m) Q_m, \tag{3.10}$$

where y_n is the position of the n-th kink. Minimizing the free energy density for an equidistant array of kinks (see Fig. 3.5(c)), we obtain the optimal period of the incommensurate state. Its temperature dependence fits well the experimental data above 2.8 K, as shown in the inset of Fig. 3.3. The length scale for the period of the IC state, set by $l \sim 150$ Å, is essentially the thickness of the domain wall in the antiferromagnetic ordering of Fe spins, even though such walls are not present in the IC state. Thus the long period of the IC state of Tb spins originates from the large stiffness and low magnetic anisotropy of the Fe magnetic subsystem.

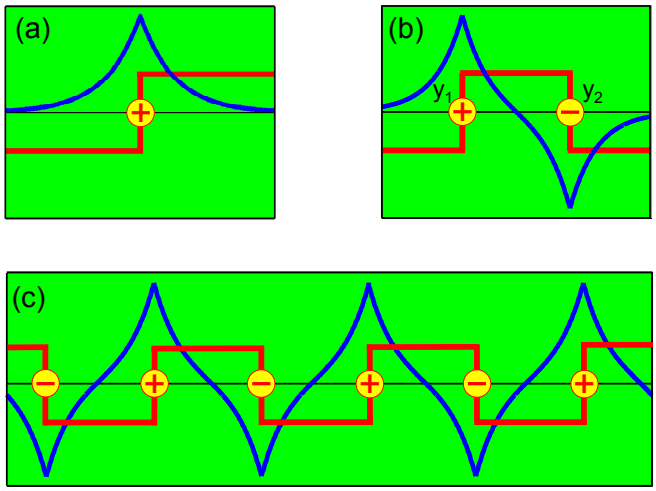

Figure 3.5: (a) Domain wall (kink) in Tb ordering (red line) and the angle θ (blue line) describing the perturbation of Fe spins near the domain wall; (b) kink-antikink pair; (c) periodic array of domain walls with alternating charges.

So far in our considerations we did not take into account crystal imperfections, which result in pinning of the domain walls and destruction of the long range incommensurate ordering. The inset of Fig. 3.3 shows that the average distance between the Tb domain walls grows as temperature decreases. This weakens the magnon-mediated interactions between the domain walls and increases the role of disorder. For randomly positioned domain walls the correlation function of the A-type Tb order parameter decays exponentially with the distance: $\langle A(y)A(0)\rangle \propto e^{-2|y|/d}$, where d is the average distance between the walls, resulting in a broad A-type reflection with the Lorentzian shape, which fits well our neutron data for $T < 2.8$ K and $\mu_0 H_c > 0.5$ T. This explains the origin of the LT$'$ phase in the experimental phase diagram Fig. 3.3.

3.4 Conclusions

We derived the Landau theory of rare earth orthoferrites, and showed that the exchange interactions between the rare earth and iron sublattices lead to frustration. If sufficiently strong, these interactions, having the form of Lifshitz invariants, can stabilize peculiar modulated states with sharp kinks in the rare-earth magnetic ordering, interacting through the smooth distortions in Fe ordering. These repulsive interactions between the neighboring kinks result in large period of the modulated structure. Another remarkable feature of the solitonic array in $TbFeO_3$ is its weak ferromagnetic moment, which is responsible for the stabilization of the state under applied magnetic field.

The tantalizing suggestion from our work is that periodic domain wall arrays may be present in other orthoferrites and orthochromites. Lifshitz invariants similar to Eq.(3.5) are certainly allowed by symmetry in multiferroic materials, such as $GdFeO_3$, where electric polarization is induced by a transition metal spin order (even under inversion and weakly ferromagnetic) coexisting with a rare earth spin order (odd under inversion) [9]. Long-ranged interactions between domain walls in these two orders resulting from such invariants can have strong effect on switching of the spontaneous electric polarization with an applied magnetic field and *vice versa*.

Chapter 4

Coupled domain wall motion in $GdFeO_3$

Abstract

The possibility to switch an electric polarization by a magnetic field (and a magnetization by an electric field) is crucial for practical applications of multiferroic materials. In multiferroic perovskite $GdFeO_3$ the polarization is proportional to the product of two magnetic order parameters, one of which describes the weakly ferromagnetic ordering of Fe spins and therefore can be reversed by the magnetic field. Another order parameter, describing the purely antiferromagnetic ordering of Gd spins, on the contrary, should not be influenced by the applied magnetic field. Thus one expects the polarization to be reversed as the magnetic field is swept through zero. In the experiment, however, the polarization reversal is not observed [9].

Switching of the order parameters in the bulk involves the propagation of domain walls. Thus the switching of the magnetization by an electric field in multiferroics requires the coupled motion of interacting ferromagnetic and ferroelectric domain walls. We study interactions between the domain walls in Gd and Fe magnetic ordering, model their motion and explain how the drag of the domain walls in the Gd ordering by the magnetic field-driven domain walls in the Fe spin ordering can explain the incomplete polarization switching.

4.1 Introduction

Magnetic domains are at the heart of the modern information storage technology. Manipulation of domains in data storage devices is achieved by driving currents through miniature electromagnets, which leads to the excessive heating of the devices, preventing further increase of the information density [64]. Multiferroic materials offer a unique opportunity to manipulate magnetic domains by electric fields, which was demonstrated in $GdFeO_3$ by the seminal work of Tokunaga *et al*.

This project was performed in the collaboration with K. Duivenvoorden.

[9]. In this material electric polarization is proportional to the product of the order parameters describing the magnetic orders of Gd and Fe ions. The Fe spins are ordered antiferromagnetically with a weak ferromagnetic component in the crystallographic c direction, which allows to reverse their ordering by reversing an applied magnetic field while the purely antiferromagnetic ordering of Gd spins should stay unaltered under the field reversal. However in the experiment a polarization, although changed significantly, was not reversed, indicating that the Gd order does change greatly upon the magnetization reversal. Moreover, the reversal of the applied electric field did not reverse the magnetization, but changed it only slightly.

To switch an order parameter at once in the whole volume of a material one needs to overcome the anisotropy barrier which scales as a volume. Much energetically cheaper way is to create a domain wall (DW) on the boundary (DW energy scales as a cross-section area) and propagate it through the volume. That's why the switching in the samples larger than the domain wall width (in which the domain wall fits) is facilitated by the domain wall motion.

Then the magnetic field is applied to the $GdFeO_3$ sample, domain walls in Fe ordering move in such a way that the domains with a weak ferromagnetic moment along the field grow. On their way Fe DWs might be capable to drag Gd DWs. Since purely AFM ordering of Gd can not be reversed by sweeping the magnetic field, the drag of Gd DWs by Fe DWs seems to be the only explanation for the experimentally observed change in Gd ordering.

Although the dynamics of magnetic domain walls driven by applied magnetic fields or currents has been extensively studied both theoretically and experimentally [65–67], little is known about the dynamics of DWs of one kind driven by the interaction with moving DWs of another kind. Although seemingly complicated, this mechanism is at the heart of switching in multiferroics, and thus could be very important for future applications. New nonlinear phenomena such as the creation, drag and annihilation of DWs of one kind induced by the DWs of another kind should be understood in order to explain and exploit the magnetoelectric switching in multiferroics. Here we present (to our best knowledge) the first study addressing the *multiferroic switching*, that is a change of one order parameter induced by the driven switching of another.

In this chapter we aim to derive the equations of motion of interacting ferroelectric and weak ferromagnetic domain walls in $GdFeO_3$ and show how their interaction can lead to simultaneous switching of (non-interacting in the uniform state) magnetic order parameters of Gd and Fe sublattices. The reminder of this

chapter is structured as follows. In the sec. 4.2 we use the microscopic symmetry considerations to derive the phenomenological theory describing interacting non-uniform orders in $GdFeO_3$. This allows us to obtain an effective model of interacting ferroelectric and ferromagnetic domain walls (sec. 4.3). We study the dynamics of this model by a variational method in sec. 4.4 and check our analytical results performing the numerical simulations in sec. 4.5. We conclude by discussing the relevance to the published experimental data and possible further experiments in the sec. 4.6.

4.2 Symmetry analysis

The orthoferrite $GdFeO_3$ has a distorted perovskite crystal structure (space group P*bnm*, [68]) with 8 magnetic ions in the unit cell: four Fe^{3+} ions (d^5, $S = 5/2, L = 0$) and four Gd^{3+} ions (f^7, $S = 7/2, L = 0$), as shown in Fig. 4.1. Table 4.1 shows irreducible representations of this symmetry group and the transformation properties of all the possible magnetic order parameters with a zero wavevector.

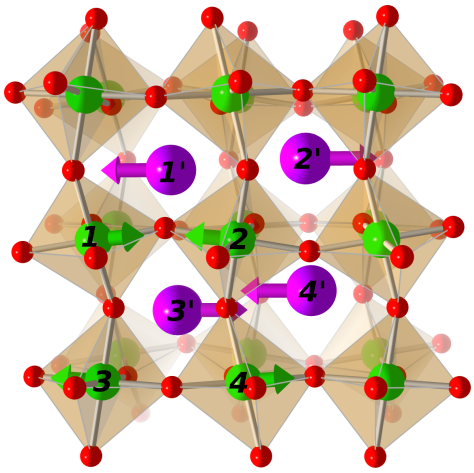

Figure 4.1: The unit cell of $GdFeO_3$ with four Fe ions in green (marked $1, 2, 3, 4$) and four Gd ions in violet ($1', 2', 3', 4'$). For simplicity, the oxygen ions are ommitted. The arrows show the directions of magnetic moments observed below 2.5 K [69, 9].

Below the Néel temperature $T_N^{Fe} = 661$ K, Fe spins order antiferromagneti-

	Fe	Gd	$\tilde{m}_x$	$\tilde{m}_y$	m_z
Γ_1	$A_xG_yC_z$	C'_z	+	+	+
Γ_2	$F_xC_yG_z$	$F'_xC'_y$	+	−	−
Γ_3	$C_xF_yA_z$	$C'_xF'_y$	−	+	−
Γ_4	$G_xA_yF_z$	F'_z	−	−	+
Γ_5		$G'_xA'_y$	−	−	−
Γ_6		A'_z	−	+	+
Γ_7		G'_z	+	−	+
Γ_8		$A'_xG'_y$	+	+	−

Table 4.1: Irreducible representations of $Pbnm$ space group and transformation properties of order parameters under the three generators of the group: the two glide mirrors, $\tilde{m}_x : (x, y, z) \to (1/2 - x, 1/2 + y, z)$ and $\tilde{m}_y : (x, y, z) \to (1/2+x, 1/2-y, 1/2+z)$, and the mirror $m_z : (x, y, z) \to (x, y, 1/2-z)$, notation from [70].

cally [71] (G_xA_y in Bertaut's notation [57]) with a weak ferromagnetic moment (F_z). This ordering has Γ_4 symmetry (Table 4.1). Below 2.5 K, the Gd spins also order antiferromagnetically G'_x [72] (prime denotes that the order parameter describes Gd magnetic ordering). G'_x ordering transforms according to Γ_5 irreducible representation and breaks inversion symmetry. In this state $GdFeO_3$ is an improper ferroelectric — the symmetry-allowed term in the free energy density

$$f_P = \eta_P P_z G_x G'_x \tag{4.1}$$

leads to a polarization in the c-direction, $P_z = -\frac{\partial \mathcal{F}}{\partial E_z} = \eta_P G_x G'_x$. This means that the domain wall in G'_x order is also a ferroelectric domain wall. At the domain wall in G_x order both the weak magnetization and polarization change sign, which is why in ref. [9] this domain wall is termed the *multiferroic domain wall*. If a domain wall in G_x is accompanied by a domain wall in G'_x, the polarization across this composite domain wall does not change.

Another important symmetry-allowed term, linear in the two order parameters, is the Lifshitz invariant

$$f_L = \eta_L G_x \partial_z G'_x. \tag{4.2}$$

This term allows for a simple microscopic interpretation. The Fe ion is surrounded by the 8 antiferromagnetically-ordered Gd ions (Fig. 4.1). If their antiferromag-

netic ordering is uniform, the effective fields they produce on Fe mutually cancel. However, if G'_x order parameter is modulated, the exchange fields produced by the neighboring Gd ions do not cancel each other anymore, and the resulting effective field is proportional to the derivative of the Gd order parameter, $H_z^{Fe} \sim \partial_z G'_x$. This is described by the term $F_z \partial_z G'_x$ in the free energy density, or the term Eq. 4.2 of the same symmetry. This interaction, if sufficiently strong, can even stabilize a modulated state [73].

Even if this term is not strong enough to induce a modulation (to our best knowledge, no evidence for a non-uniform state in $GdFeO_3$ exists so far), it is still capable of inducing an interaction between the domain walls in the G_x and G'_x orders. In particular, from Eq. 4.2 it follows that a domain wall in Gd ordering gives rise to an effective field $\partial_z G'_x$ acting on an iron order parameter and *vice versa*. The Lifshitz term can, therefore, be responsible for the clamping of the domain walls in G'_x and G_x orderings.

4.3 Model

The dissipative magnetization dynamics is described in the Lagrange framework by equations [67]

$$\frac{\delta \mathcal{L}}{\delta L} = \frac{\delta \mathcal{R}}{\delta \dot{L}}. \tag{4.3}$$

Here L denotes an order parameter, $\mathcal{L} = \mathcal{L}_{\mathrm{Fe}} + \mathcal{L}_{\mathrm{Gd}} + \mathcal{L}_{\mathrm{int}}$ is the Lagrangian of a coupled Fe-Gd system, including the Lagrangian for Fe spins, Gd spins and the term describing their interaction, respectively; $\mathcal{R}$ is the Rayleigh's dissipation functional (proportional to the entropy production rate), describing the spin relaxation. Eq. (4.3) allows to calculate the time evolution of the order parameters.

The action for the Fe spins consists of the kinetic (T) and potential (U) parts: $\mathcal{L}_{\mathrm{Fe}} = \int dV \, [T_{\mathrm{Fe}} - U_{\mathrm{Fe}}]$, where the integration goes over the sample volume. The kinetic part T_{Fe} is given by [67, 74]

$$T_{\mathrm{Fe}} = \sum_{i=1}^{4} \hbar \mathcal{A}(\mathbf{s}_i) \cdot \frac{\partial \mathbf{s}_i}{\partial t}, \tag{4.4}$$

where $\mathbf{s}_1, ..., \mathbf{s}_4$ represent the spin density from different Fe ions in the unit cell,

and the vector potential $\mathcal{A}$ obeys $\nabla_{\mathbf{s}_i} \times \mathcal{A}(\mathbf{s}_i) = \mathbf{s}_i$. The potential energy

$$\begin{aligned} U_{Fe} &= \frac{a_1}{2}\mathbf{F}^2 + \frac{a_2}{2}\mathbf{A}^2 + \frac{a_3}{2}\mathbf{C}^2 \\ &+ \frac{c_F}{2}\left(\frac{\partial \mathbf{F}}{\partial z}\right)^2 + \frac{c_G}{2}\left(\frac{\partial \mathbf{G}}{\partial z}\right)^2 + \frac{c_A}{2}\left(\frac{\partial \mathbf{A}}{\partial z}\right)^2 + \frac{c_C}{2}\left(\frac{\partial \mathbf{C}}{\partial z}\right)^2 \\ &- \frac{k_x}{2}G_x^2 + d_1 F_x G_z - d_2 F_z G_x + d_3 A_x G_y \\ &- d_4 A_y G_x + d_5 C_y G_z - d_6 C_z G_y - \mathbf{FH} \end{aligned} \tag{4.5}$$

is the sum of the exchange terms (with a_i and c_i), the easy x-axis anisotropy (term with k_x), the Dzyaloshinskii-Moriya interactions (terms with d_i) and the coupling of the weak ferromagnetic moment to the applied magnetic field $\mathbf{H}$ (the last term). Here we neglect the magnetic anisotropies for the order parameters $\mathbf{F}$, $\mathbf{A}$ and $\mathbf{C}$ and the possible couplings between them. This is justified since the order parameters $\mathbf{F}$, $\mathbf{A}$, $\mathbf{C}$ are small compared to $\mathbf{G}$. The first seven terms originate from the exchange interactions between the spins in the unit cell and are thus assumed to be of the same order of magnitude, i.e. all A_i and $c^2 a_i$ are of the same order of magnitude, where c is the lattice constant in the z-direction. In the following we are considering planar domain walls perpendicular to the z-axis, for which the exchanges along the x and y directions are not important and are thus dropped. The exchange constants a_i, c_i and anisotropy constant k_x are assumed to be positive to ensure the G_x order of Fe spins. The terms proportional to d_i originate from the relativistic Dzyaloshinskii-Moriya interaction and thus are small: $d_i \ll a_j$. The terms with d_1 and d_2 result in weak ferromagnetism.

The Lagrangian $\mathcal{L}_{\mathrm{Gd}}$ for the Gd spins has a similar form except that in U_{Gd} the d_1, d_2, d_5 and d_6-terms are not allowed by symmetry.

The interaction between the Fe and Gd subsystems is described by the Lagrangian $\mathcal{L}_{\mathrm{int}} = \int dV(-f_L - f_P)$.

The dissipation functional has the form

$$\mathcal{R} = \int dV \sum_{i=1}^{4} \left[\frac{\Gamma_{\mathrm{Fe}}}{2}\left(\frac{d\mathbf{s}_i}{dt}\right)^2 + \frac{\Gamma_{\mathrm{Gd}}}{2}\left(\frac{d\mathbf{s}_i'}{dt}\right)^2 \right],$$

where $\mathbf{s}_1', ..., \mathbf{s}_4'$ represent the spin density from different Gd ions in the unit cell.

4.4 Variational solution

In the limit of zero interaction between Fe and Gd sublattices, $\mathcal{L}_{\mathrm{int}} = 0$, Eq. (4.3) is solvable analytically and with the appropriate boundary conditions results in

the following shape of domain walls in G_x and G'_x orders:

$$G_x = gG_x^0 \tanh \frac{z - z_1}{\lambda}, \tag{4.6}$$

$$G'_x = g'G'^0_x \tanh \frac{z - z_2}{\lambda'}, \tag{4.7}$$

where g and g' are the topological charges of the domain walls, $\lambda \approx \sqrt{\frac{c_G}{k_x}}$ and $\lambda' \approx \sqrt{\frac{c'_G}{k'_x}}$ denote the widths of the two domain walls and G_x^0 and G'^0_x denote the magnitude of the order parameters in the uniform state. c'_G and k'_x are, respectively, the Heisenberg exchange constant and the easy-axis anisotropy for Gd spins. If Gd-Fe interactions are strong, they could lead to non-trivial effects, such as the creation of Gd domain walls. Here we consider the limit of weak Fe-Gd interactions, in which they don't change the shape of the domain walls significantly. In this limit we can plug the Ansatz Eq. (4.7) in Eq. (4.5), integrate over the sample volume and using Eq. (4.3) obtain the equations for the positions of the domain walls z_1 and z_2:

$$m\ddot{z_1} + \Gamma\dot{z}_1 = gH_zG_x^0 \sin\theta + F_{\text{int}}, \tag{4.8}$$

$$m'\ddot{z}_2 + \Gamma'\dot{z}_2 = -F_{\text{int}}, \tag{4.9}$$

where the dot above a variable denotes the time derivative. These equations are analogous to the Newton's equations describing the motion of interacting massive particles with friction. Here $m = 2\frac{(G_x^0)^2}{\lambda A}$ and $m' = 2\frac{(G'^0_x)^2}{\lambda' A'}$ are the masses of the two domain walls, while $\Gamma = \frac{\alpha}{\lambda}G_x^0$ and $\Gamma' = \frac{\alpha'}{\lambda'}G'^0_x$ are the friction coefficients. The angle θ describes the canting of the Fe spins from the x axis in the uniform state (measured to be ≈ 0.01 rad [75]) and F_{int} is the force with which one domain wall acts on the other. Furthermore, Γ and Γ' are the Gilbert damping parameters describing the energy dissipation of the Fe and Gd spins. From eqs. (4.8-4.9) one can see that in antiferromagnets domain wall mass is inversely proportional to its width [76, 77].

We consider the interaction Lagrangian, $\mathcal{L}_{\text{int}}$, (*cf.* eqs. (4.1),(4.2)):

$$\mathcal{L}_{\text{int}} = -\int dV \left[\eta_L G'_x \partial_z G_x + \eta_P E_z G_x G'_x\right]. \tag{4.10}$$

The energy per unit cell of two interacting DWs due to the Lifshitz term can be estimated by $\eta_L c G'_x \partial_z G_x \approx \eta_L G_x^0 G'^0_x c/\lambda$. Given the Gd-Fe exchange ~ 93 mK

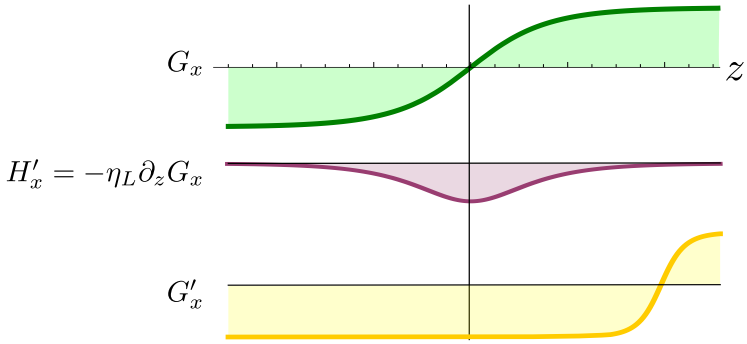

Figure 4.2: The domain walls in Fe and Gd antiferromagnetic ordering and an effective field on G'_x order parameter, H'_x, produced due to the presence of the domain wall in the Fe ordering.

[78] and the G_x domain wall width of $\lambda/c \approx 30$ unit cells, we get the interaction energy density of 1.3 mK/unit cell. This value is small compared to the energy density in the domain wall $\sim$ 6 mK/unit cell [72, 79]. The energy density due to the interaction with the electic field is even smaller. Thus the shape of the domain walls is not affected significantly by the interaction between the domain walls and can be approximated by eqs. (4.6)-(4.7).

The dependence of the potential energy on the distance between the domain walls in G_x and G'_x can now be found from eq. (4.10). Since the exchange field between Gd ions ($\sim$60 mK, [78]) is much smaller than that between Fe ions ($\sim$24 K), while the anisotropy constants are comparable, the width of a DW in the Gd ordering is at least an order of magnitude smaller than that in the Fe ordering. Performing the integration in eq. (4.10) over the z-coordinate we get for the interaction potential to the leading order in the small parameter λ'/λ:

$$V_{\text{int}} = 2\eta_L g g' {G'_x}^0 G^0_x \tanh\left(\frac{z_1 - z_2}{\lambda}\right) - 2\eta_P g g' E_z {G'_x}^0 G^0_x \ln\cosh\left(\frac{z_1 - z_2}{\lambda}\right). \tag{4.11}$$

These potentials, plotted in Fig. 4.3, result in an unusual interaction between the domain walls in Fe and Gd magnetic ordering. As depicted in Fig. 4.2, the DW in Fe ordering induces an effective field H'_x on the Gd order parameter. The Gd spins gain energy in this effective field only if the Gd DW stays to the right from the Fe DW (provided that the topological charges of two DWs are equal, $g = g'$). If the G_x domain wall shown in the Fig. 4.2 is driven by the applied magnetic field to the right, the domain wall in G'_x ordering can be carried along.

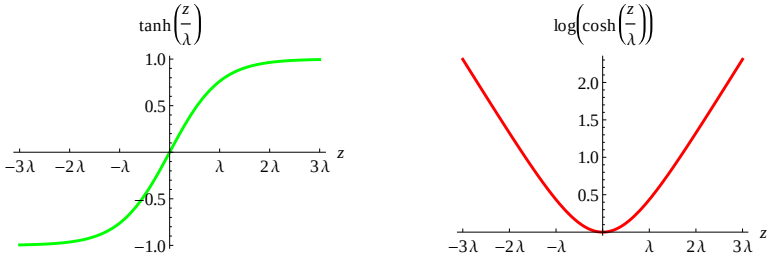

Figure 4.3: The sketch of the Lifshitz invariant-induced (a) and E_z-induced (b) contributions to the interaction energy between the domain walls in G_x and G'_x ordering of positive topological charge $g = g' = +1$ depending on their relative distance.

This gives an opportunity to move the purely antiferromagnetic domain wall in G'_x using the magnetic field.

The second term in the r.h.s. of eq. (4.11) gives rise to an even potential between domain walls in Fe and Gd ordering. For $|z_2 - z_1| \gg \lambda$ this potential grows linearly with the distance between the domain walls. That is natural, since in the electric field E_z the energy of the ferroelectric domain contained between the walls grows linearly with its size.

From eq. (4.8) we get the velocity of the domain wall in the Fe ordering:

$$v_{\mathrm{Fe}} = \frac{H_z G_x^0 \sin\theta}{\Gamma}.$$

The domain walls in the Fe and Gd orderings are clamped and moving together (see Fig. 4.4, bottom row), if

$$H_z < \frac{2\eta_L}{\lambda G_x^0 \sin\theta}\left(\frac{\Gamma}{\Gamma'} + 1\right). \tag{4.12}$$

Their velocity is

$$v_{\mathrm{clamp}} = \frac{H_z G_x^0 \sin\theta}{\Gamma + \Gamma'},$$

and the largest velocity the clamped domain walls can reach, as the magnetic field is increased, is

$$v_{\mathrm{clamp}}^{\max} = \frac{2\eta_L}{\lambda\Gamma'}.$$

If the magnetic field exceeds the upper value set by the eq. (4.12), the coupling η_L is not inducing a sufficient velocity for the Gd domain wall to follow the domain

wall in the Fe ordering, and therefore the Gd DW is eventually left behind (see Fig. 4.4, two upper rows).

4.5 Numerical simulations

In the above calculations some simplifications have been made, in particular, we assumed that the shape of the DWs is not significantly affected by their interactions. To check how sensitive our results are to the violation of these assumptions, we performed numerical simulations of motion of interacting domain walls by solving a discrete version of the Landau-Lifshitz-Gilbert equations. The model parameters we used in the simulations are summarized in the Table 4.2. The Dzyaloshinskii field is chosen to give the experimentally observed canting angle of 0.01 rad.

parameter	value	reference
Fe-Fe exchange constant	24 K	[78]
Gd-Gd exchange constant	60 mK	[78]
Gd-Fe exchange constant	93 mK	[78, 80]
Gd easy axis anisotropy	6 mK	[78, 80]

Table 4.2: The model parameters used in the numerical calculations.

As we discussed in the previous section, whether or not the clamping of domain walls occurs depends crucially on the values of the damping parameters Γ_{Fe} and Γ_{Gd}, determining the spin relaxation rates in Fe and Gd subsystems. Unfortunately, there is no data about these Gilbert parameters (to our best knowledge). Still our results suggest that the increase of the applied magnetic field reduces clamping and *vice versa*.

Fig. 4.4 shows the snapshots of the domain wall in G'_x order parameter as it is pushed by the magnetic filed-driven domain wall in G_x. Fig. 4.5 shows the phase trajectories of the two domain walls for different values of the coupling η_L. For low values of η_L the maximal velocity the DW in G'_x gets due to the Lifshitz term is lower than the velocity of Fe DW, and so Gd wall is dragged for some distance and eventually left behind (see Fig. 4.5(a,b) and two upper rows in Fig. 4.4), while for larger value of the coupling the clamped motion is observed (see Fig. 4.5(a,b) and the lower row in Fig. 4.4).

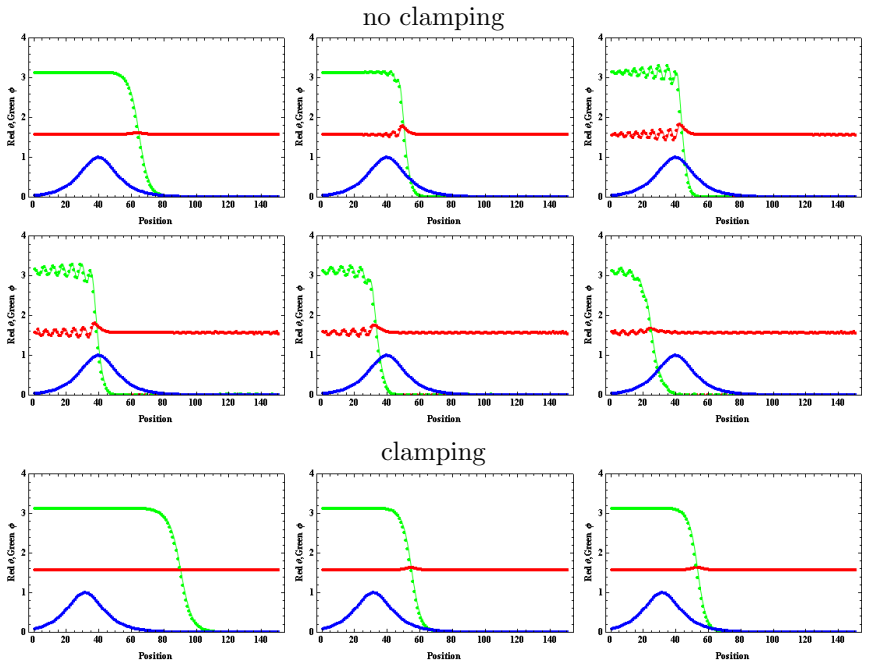

Figure 4.4: The snapshots of the motion of interacting domain walls in the reference frame bound to the center of domain wall in G_x. The applied magnetic field drives the G_x DW. The blue line shows the effective field on G'_x induced by the domain wall in G_x ordering. The z-dependence of the spherical angles of $\mathbf{G}'$ is plotted in green (for ϕ) and red (for θ). If the Gd domain wall is able to reach the velocity of Fe DW, the clamped motion occurs (lower row). Otherwise the Gd domain wall is dragged for some distance and is eventually left behind the Fe domain wall (two upper rows).

4.6 Discussion

As was shown in ref. [9] $GdFeO_3$ allows for some electric control of magnetization and for the magnetic control of polarization. Under an inversion of the electric field in c-direction, the magnetic moment (M_c) shows discontinuous jumps of the order of 1% of the average magnetic moment. Our analysis explains that the electric field leads to the linear confinement potential (term with η_P in eq. (4.11)) between the Gd and Fe DWs of certain topological charges, which makes them move towards each other. The reversal of the electric field results in attraction

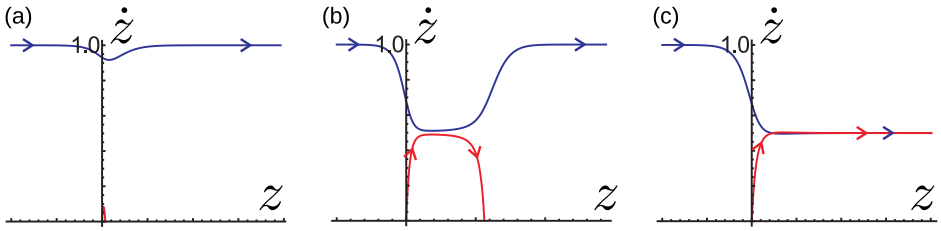

Figure 4.5: The trajectory of domain walls in G_x (blue) and G'_x (red) ordering in the $(z, \dot{z})$ phase space. The applied magnetic field drives the domain wall in Fe ordering, which drags the G'_x domain wall due to the coupling through the Lifshitz term. The Fe-Tb coupling constant is (a) $\eta_L = 0.02\eta_L^{\text{clamp}}$, (b) $\eta_L = 0.98\eta_L^{\text{clamp}}$, (c) $\eta_L = 1.02\eta_L^{\text{clamp}}$.

between different pairs of domain walls. As a result, the weakly ferromagnetic domain walls move and the change of the magnetic moment of the sample is observed. However this change depends on (essentially random) relative positions of domain walls, which makes it difficult to use the effect in applications.

It was also shown that the polarization of $GdFeO_3$ can be controlled by the magnetic field [9]. Both the polarization and magnetization show discontinuous jumps when the applied magnetic field along the crystallographic c-direction exceeds a certain threshold value. As the magnetic moment is reversed, the polarization changes from a positive value P_i to a smaller, but still positive, value P_f. Both the magnetic moment and polarization also oriented along the crystallographic c-direction.

Incomplete reversal of the polarization suggests that while the order parameter G_x is reversed due to the magnetic field-driven motion of DWs in Fe ordering, the G'_x also changes due to the drag of G'_x domain walls by G_x DWs.

4.7 Conclusions

We studied the dynamics of antiferromagnetic and ferroelectric Gd domain walls, dragged due to the interaction with the magnetic field-driven DWs in the Fe spin ordering. Such interaction results from the magnetic exchange between the Fe and Tb sublattices, the one which leads to the incommensurate state in $TbFeO_3$. The dynamics of the domain walls is analogous to that of two massive particles interacting by a long-ranged interaction that has a very peculiar dependence on the coordinates of the particles. We performed the variational calculation

and validated it by the numerical simulations. Our results explain how purely antiferromagnetic Gd ordering can be affected by the magnetic field reversal. This effect is specific to multiferroic materials.

Understanding the dynamics of domain walls in multiferroic materials could give new opportunities for spintronics and information storage technology.

Chapter 5

Landau theory of topological defects in multiferroic hexagonal manganites

Abstract

Recent experimental and theoretical advances in the field of multiferroics clarified the microscopic mechanisms of coupling between ferroelectricity and magnetism in bulk materials. On the other hand, interactions between the ferroelectric and ferromagnetic domain walls, which play the crucial role in the switching of magnetization with an applied electric field and vice versa, are less understood. Thus the observed clamping between the ferroelectric and antiferromagnetic domain walls in multiferroic hexagonal manganites[10] seems to be in contradiction with the fact that the directions of the electric polarization and spins are decoupled in the bulk. Furthermore, recent measurements showed that electric polarization changes sign at the boundaries of structural domains and revealed the existence of unusual vortices, where six structural domains merge and the electric polarization changes sign six times around the defect[11]. Here we present a theory of topological defects in hexagonal manganites based on the Ginzburg-Landau expansion of free energy with parameters determined from first-principles calculations. This theory explains the observed coupling between the structural distortions, electric polarization and spins at the domain walls and vortices.

5.1 Introduction

The simultaneous presence of ferroelectric and magnetic orders in multiferroic materials makes possible to control the electric polarization vector by an external magnetic field and to switch the direction of magnetic dipoles with an applied voltage[81–83]. Inverting the sign of ferroic order parameters by applied fields

*The *ab-initio* part of this study was performed by K. Delaney and N. Spaldin.

invariably involves the domain wall dynamics. This is why the efficiency of the 'magnetoelectric switching' crucially depends on interactions between ferroelectric and ferromagnetic domain walls, which may or may not be related to the coupling between charges and spins in bulk materials.

The recent upsurge of activity in the field of multiferroics led to discovery of many families of materials, e.g. the orthorombic rare earth manganites, spinels, hexaferrites and delafossites, in which ferroelectricity is induced by a spin ordering, usually of the cycloidal or conical spiral type.[82, 7] The resulting electric polarization is highly susceptible to an applied magnetic field and can be easily rotated or reversed.[51, 52, 84] However, this magnetically-induced polarization is usually too small to manipulate spin states by an applied voltage.

Much higher values of electric polarization are found in multiferroics such as $BiFeO_3$ and hexagonal rare earth manganites, in which ferroelectricity results from electronic and lattice instabilities.[85–87] Yet, also in these materials the electric control of magnetism is not straightforward,[88–90] since the direction of spins in magnetically ordered states is not correlated with the sign of the electric polarization.[91]

In particular, the hexagonal $R\mathrm{MnO}_3$ manganites, where R denotes a rare earth ion or Y, are improper ferroelectrics, in which electric polarization appears as a by-product of a lattice transition.[87] Their crystal structure consists of the corner-sharing MnO_5 bipyramids forming triangular layers interspaced with the layers of rare earth ions. The structural transition at $\sim$ 1100K results in the periodic tilts of the MnO_5 bipyramids and displacements of the rare earth ions along the c axis normal to the layers.[92] This periodic lattice distortion makes the size of the unit cell three times larger and is called trimerization (see Fig. 5.1). The anharmonic coupling between the trimerization and a polar optical phonon mode induces the electric polarization along the c axis, $P_z \sim 6\ \mu\mathrm{C}\cdot\mathrm{cm}^{-2}$.[87, 93]

An antiferromagnetic ordering of Mn spins in the triangular layers sets in at much lower temperatures $\sim$100 K. There is a large body of evidence for the strong interplay between the spin, charge and lattice degrees of freedom in hexagonal manganites.[94–97] However, the sign of the antiferromagnetic order parameter is decoupled from the direction of the electric polarization, as such correlation is forbidden by e.g. time reversal symmetry. So it came as a surprise when non-linear optical measurements done on $YMnO_3$ have shown that ferroelectric domain walls are firmly locked to magnetic ones.[10] Furthermore, this clamping was found to be non-reciprocal, as 'free' magnetic domain walls, not associated with the electric polarization reversals, were also observed. Strain-mediated and

spin-orbit coupling mechanisms of the clamping have been proposed.[98, 99] Very recently, however, the combination of the conducting atomic force microscopy and transmission electron microscopy showed that the ferroelectric domain walls are pinned to the boundaries of the structural domains appearing below the transition to the trimerized state.[11] In addition to the domain walls, unusual line defects have been observed, at which six different structural domains merge and the electric polarization changes its sign six times along a loop encircling the defect. These results have put the clamping between the ferroelectric and antiferromagnetic domain walls into an entirely new perspective.

In Ref. [100] it was suggested that the line defects are discrete analogs of vortices and that the change of polarization sign at structural domain boundaries is a consequence of the special form of the coupling between the lattice distortion and electric polarization originating from the 'geometric' nature of ferroelectricity in hexagonal manganites.[87, 93] Here we present the detailed study of structural domain walls and vortices in these materials based on the Ginzburg-Landau expansion and first-principles calculations. In addition, we study the spin structure of the structural defects and explain the puzzling coexistence of the clamped and free magnetic domain walls. We also show that the antiferromagnetic domain walls in hexagonal manganites can carry a ferromagnetic moment.

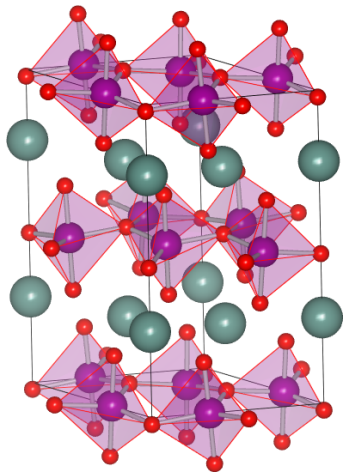

Figure 5.1: The trimerized unit cell of $YMnO_3$. The Mn ions (violet) are five-fold coordinated with oxygen ions (red). The corner-sharing MnO_5 bipyramids form buckled triangular layers, separated by the Y layers (green).

5.2 Ginzburg-Landau theory of trimerized state and improper ferroelectricity

The Landau theory of improper ferroelectricity induced by uniformly trimerized states was suggested by Fennie and Rabe. [93] Extracting parameters of the Landau expansion from the first-principles studies of $YMnO_3$, they obtained the experimentally observed lattice distortions and electric polarization. Here we extend this theory to spatially inhomogeneous lattice configurations and find the behavior of the electric polarization at structural domain walls and vortices. Furthermore, we add the coupling between the spin and lattice degrees of freedom and study the magnetic structure of these topological defects.

In the trimerized state three neighboring MnO_5 bipyramides tilt towards (or away from) the common oxygen ion (see Fig. 5.2).[87] Owing to the hexagonal structure of Mn-O layers, there are six distinct trimerized states, corresponding to six degenerate minima of the lattice energy. Being a periodic lattice modulation, the trimerization is described by the amplitude Q and phase Φ. The minimal-energy states can then be labeled by the six values of the phase: $0, \pm\frac{\pi}{3}, \pm\frac{2\pi}{3}$ and π. The physical meaning of the phase Φ is the azymuthal angle describing the in-plane displacements of apex oxygens (see Fig. 5.2). In the domain walls and vortices the phase Φ continuously interpolates between the minimal-energy values.

The trimerization is the 'frozen' zone-boundary K_3 mode with the wave vector $\mathbf{q} = (1/3, 1/3, 0)$, which breaks the $P6_3/mmc$ symmetry of the undistorted phase down to $P6_3cm$. The electric polarization P_z is associated with the zone-center Γ_2^- mode. This polar mode is non-nonlinearly coupled to the K_3 mode and appears together with the trimerization. The transformations of the trimerization phase Φ and the polarization P_z under the generators of the high-temperature space group are given in Table 5.1.

Using these symmetry properties, we obtain the expansion of the free energy density of a uniform state in powers of the amplitude and phase of the trimerization, Q and Φ, and the electric polarization P_z:

$$f_{\mathrm{u}} = \frac{a}{2}Q^2 + \frac{b}{4}Q^4 + \frac{Q^6}{6}\left(c + c'\cos 6\Phi\right) - gQ^3P_z\cos 3\Phi + \frac{g'}{2}Q^2P_z^2 + \frac{P_z^2}{2\chi_0} - E_zP_z. \tag{5.1}$$

In essence, this is the theory of Fennie and Rabe[93], to which the Q^6-terms are added and the non-linear coupling between Q and P_z has now the $\cos(3\Phi)$ dependence.

	S_a	3_z	$\tilde{2}_z$	m_{x+y}	I
Φ	$\Phi + 2\pi/3$	Φ	$-\Phi$	$-\Phi$	$\pi - \Phi$
Ψ	$\Psi + 2\pi/3$	Ψ	$\pi - \Psi$	$-\Psi$	$-\Psi$
P_z	$+P_z$	$+P_z$	$+P_z$	$+P_z$	$-P_z$
M_z	$+M_z$	$+M_z$	$+M_z$	$-M_z$	$+M_z$

Table 5.1: Transformations of the trimerization phase Φ, the spin angle Ψ, the electric polarization P_z and the magnetization M_z under the generators of the $P6_3/mmc$ space group describing the high-temperature phase: translation $S_a = (x+1, y, z)$, three-fold axis $3_z = (-y, x-y, z)$, two-fold screw axis $\tilde{2}_z = (-x, -y, z+1/2)$, mirror plane $m_{x+y} = (-y, -x, -z)$ and inversion $I = (-y, -x, -z)$.

The Φ-dependence of the energy, which determines the height of the energy barriers between the six structural domains, first appears in the sixth-order of the expansion in powers of Q. Note, however, that an additional $Q^6 \cos 6\Phi$ term is generated by minimizing the energy with respect to P_z and eliminating it from Eq.(5.1), which leads to

$$c' \to c'_{\text{eff}} = c' - \frac{1}{4}\chi_0 g^2. \tag{5.2}$$

Our *ab initio* calculations discussed below, give $c'_{\text{eff}} < 0$, corresponding to the six energy minima at $\Phi = 0, \pm\frac{\pi}{3}, \pm\frac{2\pi}{3}$ and π (see Fig. 5.3).

Importantly, the coupling $-gQ^3 P_z \cos 3\Phi$ implies that for $g > 0$ the electric polarization induced in the states with $\Phi = 0, +\frac{2\pi}{3}$ and $-\frac{2\pi}{3}$ is positive (the α_+, β_+ and γ_+ phases[11, 100]), while for $+\frac{\pi}{3}, \pi$ and $-\frac{\pi}{3}$ it is negative (the γ_-, α_- and β_- phases). In other words, 'neighboring' trimerization phases, separated by $\Delta\Phi = \frac{\pi}{3}$, have opposite electric polarizations.

To describe defects in the non-uniformly trimerized states, such as domain walls and vortices with inhomogeneous Q, Φ and P_z, we add to Eq.(5.1) the lowest-order stiffness terms accounting for the energy cost of spatial variations of these order parameters:

$$f_{\text{s}} = \frac{1}{2} \sum_{i=x,y,z} \left[s^i_Q \left(\partial_i Q \partial_i Q + Q^2 \partial_i \Phi \partial_i \Phi_i \right) + s^i_P \partial_i P_z \partial_i P_z \right]. \tag{5.3}$$

By symmetry, $s^x_Q = s^y_Q$ and $s^x_P = s^y_P$.

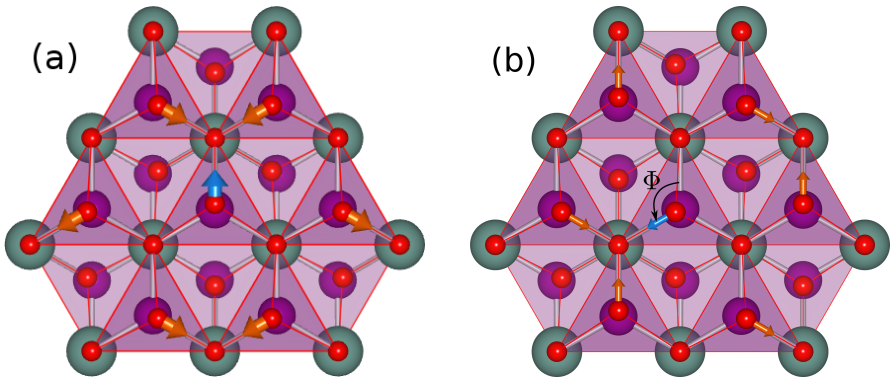

Figure 5.2: Red arrows indicate the displacements in the *ab* plane of apex oxygens in the trimerized state with $\Phi = 0$ (panel a) and with $\Phi = \frac{2\pi}{3}$ (panel b). The displacements of apex oxygens in the neighboring Mn-O layer (lighter triangles) are also shown.

5.3 Structural domain walls and vortices

The lowest-energy structural domain wall separates two 'neighboring' trimerization phases in the (Q, Φ)-plane (see Fig. 5.3), whose trimerization angles differ by $\pm\pi/3$. Figure 5.4 shows the coordinate dependence of Φ near such a domain wall obtained by numerical minimization of the free energy with the model parameters taken from *ab-initio* calculations. The domain wall width is $\sim$17Å. The amplitude of the trimerization, Q, is reduced at the domain wall by about 10 percent. This relatively small variation is the consequence of the weak Φ-dependence of the energy $f_{\mathrm{u}}(Q, \Phi)$, which only appears in the sixth order of the expansion in powers of Q.

Since the neighboring energy minima separated by $\Delta\Phi = \pm\pi/3$ have antiparallel electric polarizations, the structural domain wall is at the same time a ferroelectric domain wall (see Fig. 5.4) [100]. The improper nature of ferroelectricity in hexagonal manganites forbids purely ferroelectric domain walls, i.e. the reversals of P_z within one structural domain, since the sign of P_z is uniquely determined by the sign of $\cos 3\Phi$. Furthermore, the structural domain walls with $\Delta\Phi = 2\pi/3$, separating states with the same electric polarization, are unstable: they 'decay' into two elementary domain walls with $\Delta\Phi = \pi/3$, which repel each other. This explains the clamping between the structural and ferroelectric domain walls observed by Choi *et al.* [11]

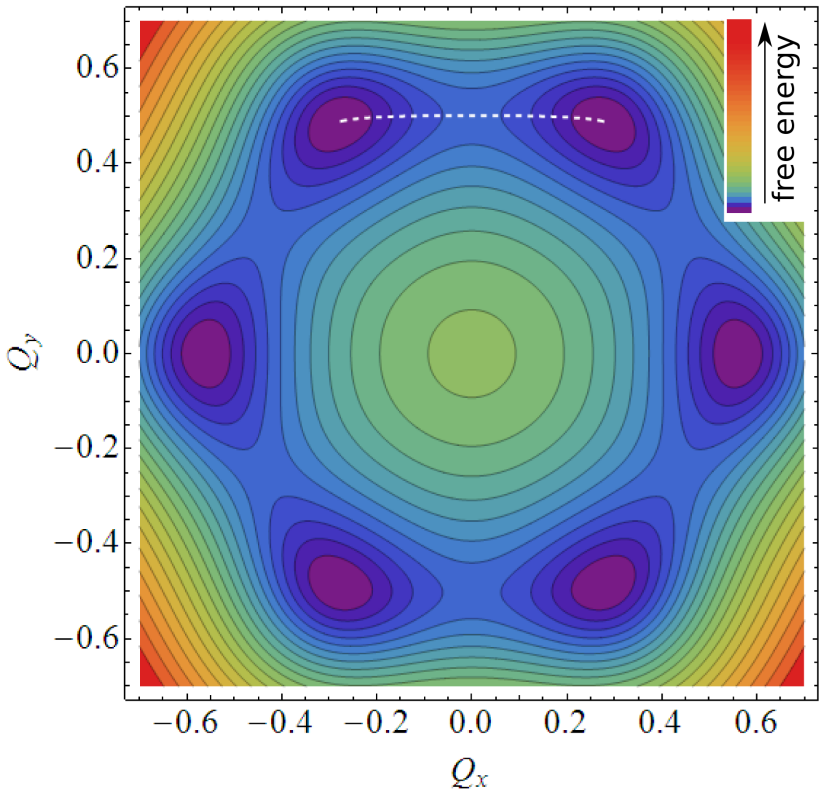

Figure 5.3: The contour plot of the free energy of uniformly trimerized states as a function of Q and Φ, for $E_z = 0$. The trajectory $Q(\Phi)$ (white dashed line) connecting two neighboring energy minima corresponds to a lowest-energy structural domain wall.

Another type of stable topological defect in the Ginzburg-Landau theory of trimerization is a structural vortex, shown in Figs. 5.5 and 5.6. At the vortex line, where the trimerization amplitude Q vanishes, all six structural domains meet in such an order that the trimerization phase Φ changes by 2π around a contour encircling the vortex line.[100] Such a defect cannot be unwound and can only be annihilated by an anti-vortex, around which the phase changes by -2π. The vortex in hexagonal manganites resembles vortices in superfluid liquids only close

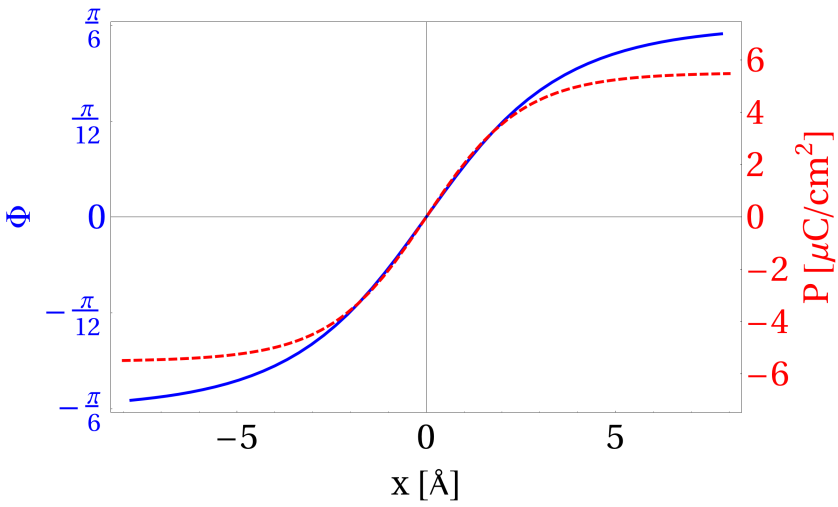

Figure 5.4: The variation of the trimerization angle Φ and the polarization P_z across the lowest-energy domain wall.

to the vortex core, where the rotation of Φ is approximately uniform. Away from the core it is a discrete vortex with a hexagonal symmetry, as the trimerization phase varies strongly only at the six radial domain walls. The electric polarization changes sign at each domain wall and varies six times along a loop encircling the vortex line. These vortices and anti-vortices are the 'cloverleaf defects' observed in Ref. [11].

Figure 5.7 shows vortex-anitvortex pair configurations. It is obtained by minimizing the energy for fixed distances between the vortex and anti-vortex and shows how the shape of the domain walls changes as the separation between the two defects increases. The domain walls diverge radially from the vortex/antivortex core with the 60°-angle between neighboring domain walls. Far from the core they bend and become parallel to minimize the total length of the structural boundaries. This shape gives rise to a linear confining potential between the vortices and anti-vortices. The observed network of domain walls connecting vortices and anti-vortices in hexagonal manganites does not have this shape,[11] since the vortex/antivortex defects are created at high temperatures, at which the shape of the domain walls is governed by thermal fluctuations. At lower temperatures the domain walls are pinned by disorder and the defect pattern becomes quenched.

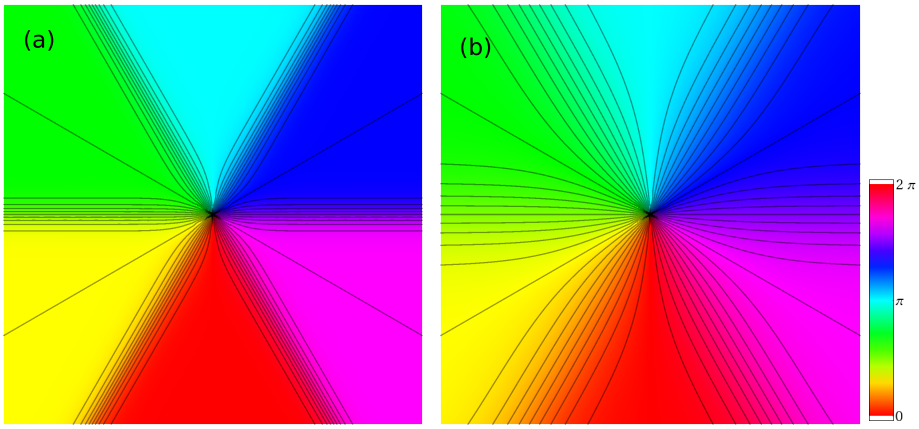

Figure 5.5: The structural vortex configuration (a), obtained by numerical minimization of the energy of the Ginzburg-Landau model. Here color encodes the trimerization angle Φ. Away from the vortex core the vortex consists of six different trimerization domains separated by the relatively sharp domain walls. The white arrows show how the magnetic order parameter varies around the vortex. Panel (b) shows the contour plot of the Ψ in an antiferromagnetic vortex, coinciding with the structural vortex.

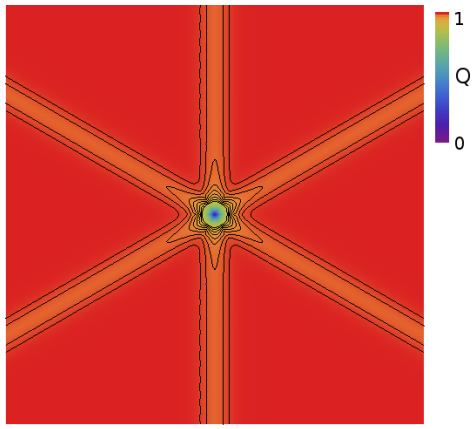

Figure 5.6: The contour plot of the amplitude of the trimerization Q in the structural vortex.

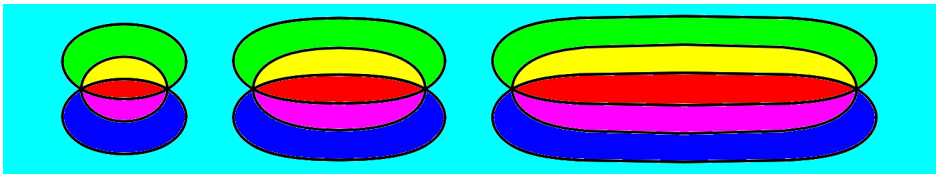

Figure 5.7: Vortex-antivortex pair configuration for a three different distances between the vortex and anti-vortex. The colored regions are six different trimerization domains separated by domain walls (black lines).

5.4 Magnetic structure of structural domain walls and vortices

Hexagonal manganites exhibit four different magnetic states, shown in Fig 5.8. Which of these states has the lowest free energy depends on the rare earth ion, temperature and the strength of an applied magnetic field.[101] For example, $YMnO_3$ below 75K undergoes the transition to the B_2 state, which in an applied magnetic field $H \geq 16$T along the c axis transforms into the A_2 phase.[102]

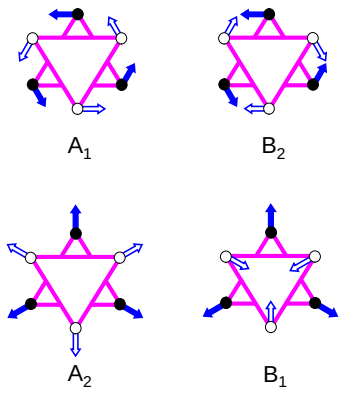

Figure 5.8: Four magnetic phases of hexagonal manganites. Filled(empty) arrows show the directions of spins in neighboring Mn layers.

In all these states, the antiferromagnetic coupling between neighboring Mn spins in the triangular *ab* layers results in the non-collinear 120°-ordering. Whether the spin orientation is 'radial' or 'tangential', depends on the directions of the local easy axes on Mn sites, while the parallel or anti-parallel alignment of spins in neighboring layers is governed by the sign of relatively weak interlayer exchange interactions.[103]

To describe inhomogeneous spin textures near structural domain walls and vortices, we introduce the angle Ψ, such that the state with $\Psi = 0$ is the B_2 state, stabilized e.g. in $YMnO_3$ below the Néel temperature, in the $\Phi = 0$ structural domain (see Fig.5.10). Other spin states are obtained by rotating all spins by the angle $+\Psi$ in odd Mn layers and by the angle $-\Psi$ in even Mn layers. This guarantees that the states with $\Psi = 0, \pm\pi/3, \pm 2\pi/3$ and π are the lowest free energy B_2 states in the structural domains with Φ equal, respectively, $0, \pm\pi/3, \pm 2\pi/3$ and π.

From the transformation properties of the spin angle Ψ, shown in Table 5.1, we find an invariant,

$$f_{\text{ani}} = \frac{\kappa Q^2}{2} \sin^2 (\Psi - \Phi) , \tag{5.4}$$

which describes the dependence of the directions of the local anisotropy axes on the tilts of the MnO_5 bipyramids. We assume κ to be positive, in which case the energy of the B_2 magnetic phase, e.g. the state with $\Psi = 0, \Phi = 0$, is lower than that of the A_2 phase, e.g. the $\Psi = \pi/2, \Phi = 0$ state. Actually, for each Φ there are two minimal-energy spin states: $\Psi = \Phi$ and $\Psi = \Phi + \pi$, which are related by the time reversal operation (reversal of all spins).

At structural domain walls Φ increases or decreases by $\pi/3$, corresponding to the rotation of the local easy axes at Mn sites by the same angle. In the minimal-energy spin state the angle Ψ rotates over the same angle as the easy axes, i.e. $\Delta\Psi = \Delta\Phi$ at each domain wall. The changes in Φ and Ψ occur, however, at very different length scales. While the width of the structural domain is of order a few lattice constants, the magnetic domain wall has the width ~ 300Å (see Fig. 5.9).

Thus, structural domain walls change the sign of the electric polarization and induce the 60° magnetic domain walls, which explains the clamping between the ferroelectric and magnetic domain walls observed by Fiebig *et al.*[10] The 'free' antiferromagnetic domain walls, also observed in experiment, that do not follow ferroelectric domain boundaries are the usual 180° antiferromagnetic domain walls, at which Ψ changes by $\pm\pi$ within one structural domain (i.e. the domain walls between magnetic states related by time reversal).

It is also clear that in the minimal-energy magnetic state spins wind around

the structural vortices and the total spin rotation angle along a loop encircling the vortex is $\Delta\Phi = \Delta\Psi = \pm 2\pi$ (see Fig. 5.5). In other words, structural vortices are also magnetic vortices.

The recent small-angle neutron scattering experiment on $HoMnO_3$ as well as the electric switching of magnetization of a the coupled ferromagnetic and $LuMnO_3$ thin films,[104, 90] suggest that antiferromagnetic domain walls in hexagonal manganites can carry a ferromagnetic moment. The coupling between the magnetization along the c axis and the phase difference $\Psi - \Phi$ allowed by symmetries of the structural and magnetic order parameters (see Table 5.1) has the form,

$$f_{\mathrm{M}} = -\lambda M_z Q \sin(\Psi - \Phi)\,. \tag{5.5}$$

In the minimal-energy domain wall, shown in Fig. 5.9, the spin angle Ψ is larger than Φ at negative x and larger than Φ at positive x, so that the net induced ferromagnetic moment is 0. On the other hand, the domain wall with $\Delta\Phi = +\pi/3$ and $\Delta\Psi = -2\pi/3$ gives rise to a nonzero ferromagnetic moment induced by the coupling Eq.(5.5). This 'ferromagnetic' domain wall has a higher energy than the one shown in Fig. 5.9 due to the larger spin-rotation angle. Nevertheless, a finite density of such ferromagnetic domain walls must be present in hexagonal manganites.

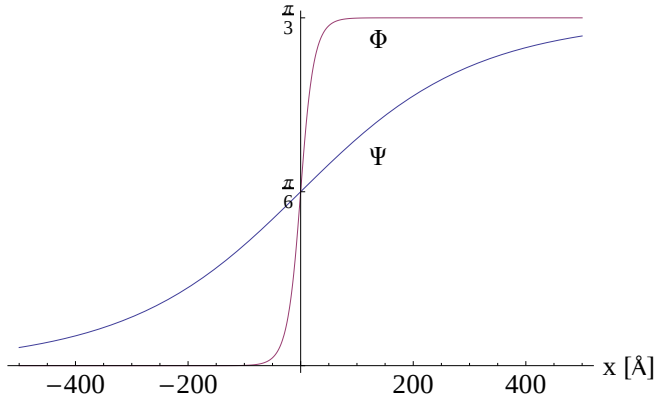

Figure 5.9: At the structural domain wall the trimerization phase Φ and the directions of magnetic easy axes on Mn sites rotate by $\pm\frac{\pi}{3}$. The directions of spins, described by the angle Ψ, adjust to the new directions of the easy axes by continuously rotating over the same angle at a much larger length scale.

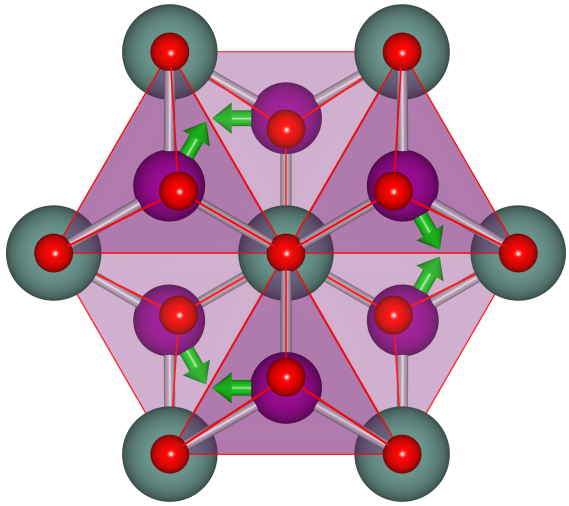

Figure 5.10: The antiferromagnetic ordering of Mn ions (green arrows) is of B_2 type.

5.5 Conclusions

In conclusion, we presented Ginzburg-Landau theory of topological defects in 'geometric ferroelectrics'. This theory explains unusual properties of domain walls and vortices in the periodically distorted crystal lattice of hexagonal manganites, recently revealed by combined transmission electron and conductive atomic force microscopies.[11] We showed that ferroelectric domain walls in these materials coincide with structural domain walls and that the sign of electric polarization changes six times around the vortex core.

The model parameters were calculated using first-principles methods, which allowed us to find the spatial extent of the domain walls and vortices. These calculations also showed that the improper ferroelectricity in hexagonal manganites has a surprisingly strong 'feedback' effect on their structural properties. We have found that the energy barriers between different structural phases almost entirely result from the non-linear coupling between the lattice trimerization and electric polarization. This coupling, therefore, determines the shape of the domain wall and vortices and may also have a strong effect on the nature of the phase transition into the trimerized state.

Finally, we studied magnetic properties of the structural defects. Using sym-

metry considereations, we showed that there are several kinds of antiferromagnetic domain walls present in these materials: the 60° domain wall, which is the minimal-energy magnetic state of the structural domain wall and the usual 180° domain walls inside structural domains. The former domain walls are clamped with ferroelectric domain walls, while the latter are not, which explains the results of non-linear optical studies of hexagonal manganites.[10] There are exist also 120° domain walls, residing at the structural domain boundaries, which carry a ferromagnetic moment. Finally, below the spin ordering temperature the structural/ferroelectric vortices also become magnetic vortices with spins rotating over an angle of $\pm 2\pi$ around the vortex core.

Chapter 6

Excitonic magneto-absorption in Cu_2O

Abstract

We study the absorption spectra of the yellow excitons in Cu_2O in high magnetic fields. We show that the symmetry of the yellow exciton results in unusual selection rules for the optical absorption of polarized light and that the mixing of ortho- and para- excitons in magnetic field is important. Our calculation of the energies of the yellow exciton series in an arbitrary magnetic field gives an excellent fit to experimental data and allows us to understand the complex structure of excitonic levels and their magnetic field dependence, which resolves the old-standing disagreement between the results of optical absorption and cyclotron resonance measurements.

6.1 Introduction

Cuprous oxide Cu_2O is a first material where excitons – particle-hole pairs bound by Coulomb interaction – were observed [105, 106]. Experiments showed that the optical absorption spectrum of cuprous oxide exhibits a hydrogen-like series just below the band gap with the term energies $E_n = E_{\rm gap} - {\rm Ry_X}/n^2, n = 2, 3, \ldots,$ lately called the Wannier-Mott yellow exciton series. Here ${\rm Ry_X} = 98$ meV is the excitonic Rydberg constant, and $E_{\rm gap} = 2.17$ eV is the optical gap.

Elliott [107] studied the dependence of the absorption intensity on the line number and found that for dipole-allowed transitions all the lines with $n = 1, 2, \ldots$ are visible, whereas the dipole-forbidden series starts with $n = 2$ line. Since in the yellow series the $n = 1$ line is absent, he attributed this series to dipole-forbidden transitions. Later Elliott [108] analyzed the anisotropy of $1s$ excitonic absorption and suggested that the valence band is formed mostly by the Cu 3d orbitals, whereas the conduction band is of the Cu 4s and/or O 3s

*This study was motivated and heavily relies on the experimental work performed by the group of P.H.M van Loosdrecht based in the University of Groningen.

method	m_e	m_h	μ	ϵ	g_c	g_v
optical[113]	0.61	0.84	0.35	7.1	-2.0	0.28
cyclotron resonance [114]	0.99	0.69	0.41	7.5		

Table 6.1: Effective masses of electrons m_e, holes m_h, the dielectric constant ϵ and an exciton reduced mass μ obtained in different experiments. The masses are in the units of bare electron mass m_0.

origin. The crystal field splits the Cu $3d$ orbitals and the upper of them is of Γ_{25}^+ symmetry (We use the notation for irreducible representations from [109] except that instead of primes, the parity is denoted by + or − superscripts.). It is further split by the spin-orbit coupling into twofold Γ_7^+ (with higher energy) and fourfold degenerate Γ_8^+ level, and the lowest conduction band has Γ_1^+ symmetry (Γ_6^+ including spin). This assignment is confirmed by the recent first principles studies [110, 111].

Optical experiments give information about the excitonic Rydberg constant and the reduced mass. Further information about the material can be obtained from the splittings of excitonic levels under electric and magnetic fields. The large dielectric constant and small effective masses of carriers in Cu_2O make the size of the exciton much larger than that of a hydrogen atom, so that the effects of external electric and magnetic fields, which are small for atoms, are much stronger for excitons in Cu_2O. For example, the exciton ionization was observed [112] already in electric field $E = 5$ kV/cm, whereas the characteristic fields required to ionize the atoms are of the order of $E \sim 1000$ kV/cm. Pronounced and fairly complex Zeeman and Stark effects were first observed by Gross and Zakharchenya at magnetic field up to 2.8 T [112].

The magnetoabsorption spectra of excitons in Cu_2O were widely studied over the past decades [112, 115–119]. These experiments gave contradictory information (see Table 6.1) and motivated theoretical studies of the excitons in strong magnetic field. Since the excitonic Rydberg constant is much smaller than that of a hydrogen atom, in Cu_2O one can achieve the regime of strong magnetic fields, where field-induced level splittings become comparable to level spacing in zero field, the regime for hydrogen atom only achieved in neutron stars. For Cu_2O at the magnetic field of $H = 30T$ the cyclotron energy is comparable to the binding energy already for the $n = 3$. For higher levels the high field limit ($\beta = \hbar\omega_c/(2Ry_X/n^2) \approx 0.05n^2 \gg 1$) is reached for $n \geq 5$, but the spectrum is

very complex due to the overlap of large number of lines, which makes it difficult to use to extract exciton parameters. Therefore the most promising are the levels with $n \leq 5$, falling into intermediate field regime $\beta \sim 1$. One does not have a small parameter for a perturbative expansion, and numerical calculations are required to obtain the exciton spectrum.

Zhilich *et al.* [113] studied the oscillations of optical absorption well above the gap in magnetic field up to 10 T. These oscillations originate from the transitions between the Landau levels of electrons and holes. The effective masses of electrons and holes were estimated to be $m_e = 0.61m_0, m_h = 0.84m_0$, where m_0 is the bare electron mass. In this estimate the Coulomb interaction was neglected. Furthermore, its accuracy was limited by energy resolution and weak available magnetic fields.

At lower energies, in the region of bound excitons, the absorption lines are much more pronounced, which motivated the attempts to use them to extract the information about the excitons. Sasaki and Kuwabara [119] measured the magnetoabsorption spectrum in static magnetic fields up to 16 T. Kobayashi *et al.* [117] studied the $n = 2$ and $n = 3$ exciton absorption in pulsed magnetic fields up to 150 T. Seyama *et al.* [116] measured the spectra in static fields up to 25 T with better spectral resolution. However, the complexity of the spectra with large number of overlapping lines prevented the unambiguous assignment of excitonic levels.

Later the effective masses in Cu_2O were measured in the cyclotron resonance experiments [114], which gave $0.58m_0$ and $0.69m_0$ for light and heavy holes, respectively, and $0.99m_0$ for electrons. The disagreement between these values and the masses obtained in the excitonic optical absorption experiments [115, 113] was ascribed to polaronic effects.

Here we resolve these contradictions and provide a quantitative explanation of the magnetoabsorption spectrum. Our collaborators (P. van Loosdrecht *et al.*) performed polarized high spectral resolution optical absorption measurements in static magnetic field up to 32 T. To address the intermediate-field region, where the interaction with magnetic field and Coulomb interaction are of the same order of magnitude, we performed numerical calculation of the energies of the $n = 2, 3, 4$ excitons. The electron and hole effective masses and g-factors were chosen to fit the experimental data. Not only we get a good agreement between the theory and magnetoabsorption experiments, but the masses we obtain coincide with those obtained from the cyclotron resonance experiments thus resolving the long-standing contradiction.

This chapter is organized as follows. In section 6.2 we discuss the results of magneto-absorption measurements in Cu_2O in static magnetic fields up to 32 T. In section 6.3 we discuss the crystal symmetry, the band structure of Cu_2O and determine the symmetry of electron and hole wave functions, which allows us to derive the optical selection rules (Section 6.4). Then, in section 6.5 we calculate the peak positions of the absorption spectrum. The comparison of the experimental and theoretical results is presented in section 6.7.

6.2 Experimental results

The magnetoabsorption of Cu_2O has been studied in a Faraday geometry ($\mathbf{H}||\mathbf{k}$) with magnetic fields up to $B = 32$ T at a temperature of $T = 1.2$ K in the group of Paul van Loosdrecht. Here we outline the main results. Figure 6.1 shows the magnetic field dependence of the absorption spectra. In the absence of magnetic field, the absorption spectrum of Cu_2O exhibits the well known hydrogen-like absorption series below the gap. The spectral resolution of the experiments and the quality of the sample enable the observation of at least 5 exciton peaks of the yellow exciton series (n=2-6). In the magnetic field the Zeeman splitting of absorption peaks is observed, and the continuum above the band gap shows oscillations of intensity originating from transitions between Landau levels of the unbound electrons and holes.

Figure 6.2 shows a color plot of the optical absorption intensity as a function of the photon frequency and magnetic field. The absorption spectrum becomes more complex with the increase of the principal quantum number n. In case of Cu_2O, only the transitions to p-states ($l = 1$) for each principal quantum number n are allowed. These states are clearly observed in the absence of a magnetic field. As the magnetic field is increased, lines corresponding to the states with $l \neq 1$ become visible due to the mixing with the $l = 1$ state of relative motion [117].

6.3 Symmetry of the yellow excitons

The cuprite Cu_2O has a cubic symmetry (space group $Pn\bar{3}m$) with 4 Cu ions in the unit cell (see Fig. 6.3). The electron can be excited from the highest valence band, formed mostly by the Cu $3d$ orbitals, to the lowest conduction band, formed by the Cu $4s$ orbitals. The yellow excitons are then formed by binding the excited electrons and holes with Coulomb interaction.

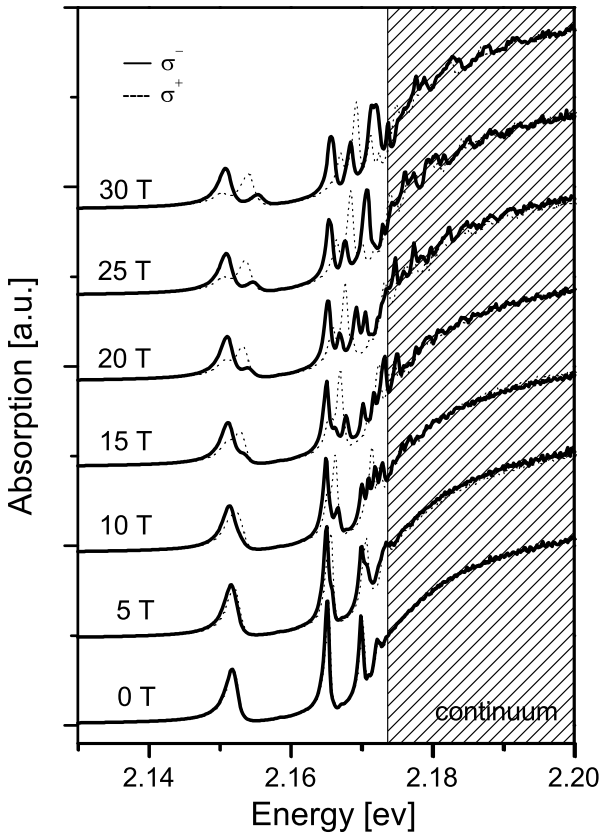

Figure 6.1: Optical absorption spectra of Cu_2O in the yellow exciton energy range for different magnetic fields measured at $T = 1.2$ K. Light has left circular polarization. Solid lines correspond to the magnetic field in the c direction, dotted lines – to the field in the opposite direction. The spectra for different fields have been given vertical offset for clarity.

The symmetries of the electron and hole bands, respectively, Γ_6^+ and Γ_7^+ [108], can be understood as follows. Each Cu^+ ion is coordinated by two oxygen ions in the dumbbell configuration, which splits its d-shell into two doublets,$(x_i^2 - y_i^2, x_i y_i)$ and $(x_i z_i, y_i z_i)$, and one singlet, $3z_i^2 - r_i^2$. Here the direction of the z_i axis is parallel to the O-Cu-O line passing through the i-th Cu ion ($i = 1, 2, 3, 4$)

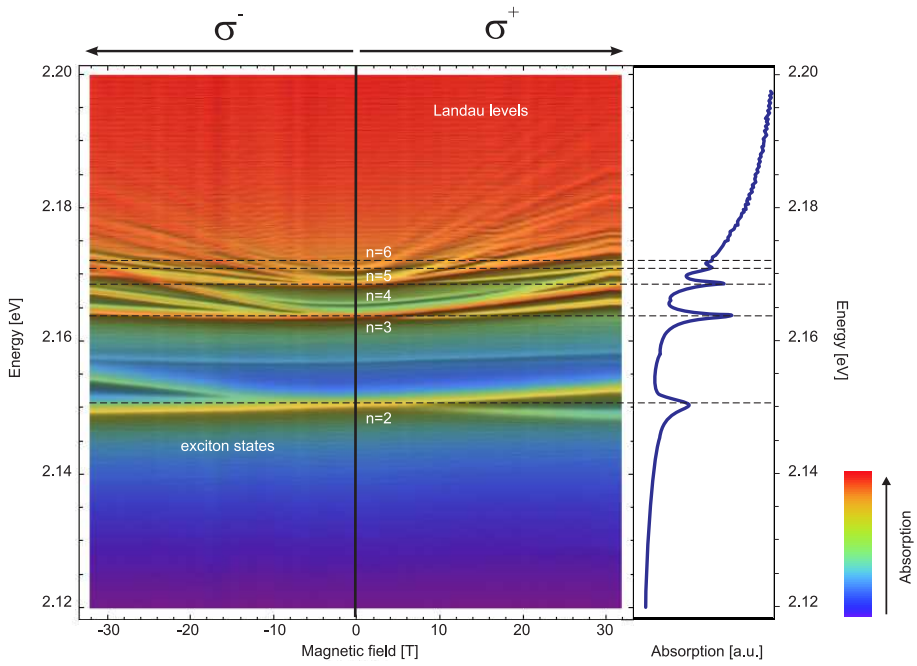

Figure 6.2: Color plot of the optical absorption of Cu_2O. Light has left circular polarization.

in the unit cell and is different for different Cu sites (see Fig. 6.3). Since the $3z_i^2 - r_i^2$ state has the highest energy, we assume for simplicity that the upper valence band is formed by these orbitals only.

As the hopping amplitudes between all pairs of the $3z_i^2 - r_i^2$ orbitals on neighboring Cu sites are equal by symmetry, the tight-binding band structure at the Γ-point consists of the non-degenerate singlet state,

$$|S\rangle = \frac{1}{2}\left(|1\rangle + |2\rangle + |3\rangle + |4\rangle\right) \tag{6.1}$$

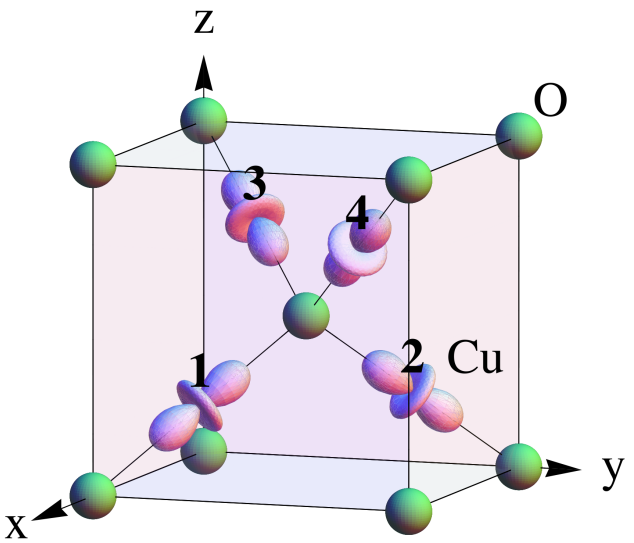

Figure 6.3: The unit cell of Cu_2O. Oxygen ions in green form a body-centered cubic lattice. The Cu d orbitals (numbered) give the dominant contribution to the upper valence band.

and the triplet of degenerate states,

$$\begin{cases} |X\rangle &= \frac{1}{2}\left(+|1\rangle - |2\rangle - |3\rangle + |4\rangle\right), \\ |Y\rangle &= \frac{1}{2}\left(-|1\rangle + |2\rangle - |3\rangle + |4\rangle\right), \\ |Z\rangle &= \frac{1}{2}\left(-|1\rangle - |2\rangle + |3\rangle + |4\rangle\right), \end{cases} \tag{6.2}$$

where $|i\rangle$ denotes the $3z_i^2 - r_i^2$ orbital on the i-th Cu site. Table 6.2 shows the transformation of these three states under the generators of $Pn\bar{3}m$ group: the π-rotation around the z-axis, C_{2z}: $(x, y, z) \to \left(\frac{1}{2} - x, \frac{1}{2} - y, z\right)$, the $\frac{2\pi}{3}$-rotation around the body diagonal of the cube, C_3: $(x, y, z) \to (z, x, y)$, the mirror, m_{x-y}: $(x, y, z) \to (y, x, z)$, and inversion I: $(x, y, z) \to (1/2 - x, 1/2 - y, 1/2 - z)$.

As the hopping between nearest-neighbor Cu sites is mediated by oxygen ions, the hopping parameter t of the effective tight-binding model describing the Cu sites only, $H = -t\sum_{<i,j>\sigma}\left(c^\dagger_{i\sigma}c_{j\sigma} + c^\dagger_{j\sigma}c_{i\sigma}\right)$, where the operator $c_{i\sigma}$ annihilates electron in the state $3z_i^2 - r_i^2$ on the site i with the spin projection σ, is given

State	C_{2z}	C_3	m_{x-y}	I
$\|X\rangle$	$-\|X\rangle$	$\|Y\rangle$	$\|Y\rangle$	$\|X\rangle$
$\|Y\rangle$	$-\|Y\rangle$	$\|Z\rangle$	$\|X\rangle$	$\|Y\rangle$
$\|Z\rangle$	$+\|Z\rangle$	$\|X\rangle$	$\|Z\rangle$	$\|Z\rangle$

Table 6.2: The transformation rules of the $|X\rangle, |Y\rangle, |Z\rangle$ states under the generators of point subgroup of $Pn\bar{3}m$ group.

by $t = \frac{t_{pd}^2}{\Delta}$, where t_{pd} is the hopping amplitude between the Cu to O sites and $\Delta > 0$ is the charge transfer energy. Since $t > 0$, the states with the energy $+2t$ at the Γ-point lie higher than the singlet state with the energy $-6t$. The spin-orbit interaction further splits the six (including the spin degeneracy) states into a doublet [120],

$$\begin{cases} |\uparrow\rangle_v &= -\frac{1}{\sqrt{3}}\left[\left(|X\rangle + i\,|Y\rangle\right)|\downarrow\rangle + |Z\rangle\,|\uparrow\rangle\right], \\ |\downarrow\rangle_v &= \frac{1}{\sqrt{3}}\left[\left(-|X\rangle + i\,|Y\rangle\right)|\uparrow\rangle + |Z\rangle\,|\downarrow\rangle\right], \end{cases} \tag{6.3}$$

and a quadruplet (here the subscript v indicates the valence band). The energy of the doublet is higher than the energy of the quadruplet by ~ 134 meV [121]. This spin-orbital splitting originates from the virtual admixture of $x_i z_i$ and $y_i z_i$ states to the $3z_i^2 - r_i^2$ state by the spin-orbit coupling on Cu sites. The doublet belongs to the upper valence band, which gives rise to the yellow exciton, while the quadruplet gives rise to the green exciton series [112]. We stress that our $|X\rangle$, $|Y\rangle$ and $|Z\rangle$ states are formed by the $3z_i^2 - r_i^2$ orbitals of 4 Cu ions in the unit cell and are different from the atomic xy, yz, and zx orbitals discussed in Ref. [120].

Using Eq. (6.3) and Table 6.2, one finds that the valence-band doublet, $\psi_v =$

$\begin{pmatrix} |\uparrow\rangle_v \\ |\downarrow\rangle_v \end{pmatrix}$, transforms as Γ_7^+ representation:

$$
\begin{aligned}
C_{2z}\psi_v &= e^{-i\frac{\pi}{2}\sigma_z}\psi_v = \begin{pmatrix} -i & 0 \\ 0 & i \end{pmatrix}\psi_v, \\
C_3\psi_v &= e^{-i\frac{\pi}{3\sqrt{3}}(\sigma_x+\sigma_y+\sigma_z)}\psi_v = \frac{1}{2}\begin{pmatrix} 1-i & -1-i \\ 1-i & 1+i \end{pmatrix}\psi_v, \\
m_{x-y}\psi_v &= \frac{i}{\sqrt{2}}\left(\sigma_x-\sigma_y\right)\psi_v = \frac{i}{\sqrt{2}}\begin{pmatrix} 0 & 1+i \\ 1-i & 0 \end{pmatrix}\psi_v, \\
I\psi_v &= \psi_v.
\end{aligned}
\tag{6.4}
$$

Similarly, the lowest conduction band, formed by the Cu $4s$ orbitals, splits into a triplet and singlet at the Γ-point with the singlet state having a lower energy. Since the orbital part of the singlet wave function [see Eq. (6.1)], is invariant under all operations of the space group, the symmetry of the doublet, $\psi_c = \begin{pmatrix} |\uparrow\rangle_c \\ |\downarrow\rangle_c \end{pmatrix}$, formed by the spin-up and spin-down electron states in the lowest conduction band, is determined by its spin wave function. Thus, the conduction electron in the yellow exciton has the same transformation properties as the valence electron [see Eq. (6.4)], except for the opposite sign for the mirror transformation, m_{x-y}, and, hence, belongs to Γ_6^+ representation.

Finally, the conduction electron and the valence hole form ortho- and para-excitons with the total spin, S, respectively, 1 and 0. Due to the exchange interaction between the conduction and valence electrons in the $n = 1$ yellow exciton state, the energy of the ortho-exciton is 12meV higher than that of para-exciton [122–124, 120, 125].

6.4 Selection rules

Since the valence $3d$ and conduction $4s$ bands have the same parity, the excitation of the yellow exciton series is dipole forbidden and results from the electric quadrupole transition [108]. The conduction and valence band doublets, ψ_c and ψ_v, transform under the mirror m_{x-y} with opposite signs (see Sec. 6.3), resulting

in the"wrong" symmetry of yellow excitons: the paraexciton wave function,

$$|S=0,S_z=0\rangle = \frac{1}{\sqrt{2}}\left(\psi_{c\uparrow}\psi_{v\downarrow} - \psi_{c\downarrow}\psi_{v\uparrow}\right),$$

is odd under m_{x-y}, while the orthoexciton wave function with zero projection of the total spin,

$$|S=1,S_z=0\rangle = \frac{1}{\sqrt{2}}\left(\psi_{c\uparrow}\psi_{v\downarrow} + \psi_{c\downarrow}\psi_{v\uparrow}\right),$$

is even.

The invariance of the paraexciton wave function $|0,0\rangle$ under C_3 and C_2 rotations requires that the amplitude of the photoexcitation of this state has the form,

$$A_{00} \propto \sum_{\mathbf{k}} \varphi^*_{\mathbf{k}} \left(\mathbf{e}\cdot\mathbf{k}\right), \tag{6.5}$$

where $\mathbf{k}$ is the relative wave vector of the electron-hole pair, $\varphi_{\mathbf{k}}$ is the wave function of the relative motion, discussed in the next section, and $\mathbf{e} = \mathbf{e}_{\mathbf{q}\lambda}$ is the polarization vector of the photon with the wave vector $\mathbf{q}$ and polarization λ. The scalar product $(\mathbf{e}\cdot\mathbf{k})$ is invariant under m_{x-y}, while A_{00} must be odd, implying that $A_{00}=0$, i.e., paraexcitons cannot be excited via the one-photon absorption.

The orthoexciton states $|1,S_z\rangle$ with $S_z=-1,0,1$, are excited by the components of the quadrupolar tensor,

$$Q_{ab} \propto \sum_{\mathbf{k}} \varphi^*_{\mathbf{k}} \left(e_a k_b + e_b k_a - \frac{2}{3}\delta_{ab}\mathbf{e}\cdot\mathbf{k}\right). \tag{6.6}$$

The excitation amplitudes, invariant under all crystal symmetries, have an obvious form for the Cartesian components of the orthoexciton atomic wave functions, $|\mathrm{x}\rangle$, $|\mathrm{y}\rangle$, and $|\mathrm{z}\rangle$:

$$\begin{cases} |1,1\rangle &=& -\frac{1}{\sqrt{2}}\left(|\mathrm{x}\rangle + i\,|\mathrm{y}\rangle\right), \\ |1,0\rangle &=& |\mathrm{z}\rangle\,, \\ |1,1\rangle &=& \frac{1}{\sqrt{2}}\left(|\mathrm{x}\rangle - i\,|\mathrm{y}\rangle\right). \end{cases} \tag{6.7}$$

The form of the invariant amplitudes is:

$$\begin{array}{lcl} A_{\mathrm{x}} &\propto& Q_{yz}, \\ A_{\mathrm{y}} &\propto& Q_{zx}, \\ A_{\mathrm{z}} &\propto& Q_{xy}, \end{array} \tag{6.8}$$

and the proportionality coefficient is the same for all states.

For the Faraday geometry, $q \| H$ (and $H \| z$),

$$A_x, A_y \propto \sum_{\mathbf{k}} k_z \varphi^*_{\mathbf{k}} \propto \left. \frac{\partial \varphi^*}{\partial z} \right|_{\mathbf{r}=0}, \tag{6.9}$$

so that these amplitudes are only nonzero for $m = 0$, where m is the z-projection of orbital momentum of the relative motion of the electron-hole pair. Similarly, A_z, does not vanish only for $m = \pm 1$ states with nonzero $\left[\frac{\partial \varphi^*}{\partial x} \mp i \frac{\partial \varphi^*}{\partial y} \right]_{\mathbf{r}=0}$. For zero magnetic field the allowed excited states have the orbital momentum $l = 1$ (p-states).

In this way we can obtain the following unusual selection rules for orthoexcitons from the yellow series: a photon with the polarization $\lambda = \pm 1$ [$\mathbf{e}_{\mathbf{q},\pm 1} = \frac{1}{\sqrt{2}} (1, \pm i, 0)$] excites either the state with $S_z = -\lambda$ and $m = 0$, or the state with $S_z = 0$ and $m = -\lambda$. These selection rules are opposite to those for rotationally-invariant systems, where the z-component of the total angular momentum is a good quantum number.

6.5 Motion of electron-hole pair in magnetic field

The atomic part of the exciton wave function, discussed in the previous section, remains largely unaffected by an applied magnetic field of 32T, except for the mixing of the paraexciton and orthoexciton states. On the other hand, magnetic field has a strong effect on the relative motion of the electron and hole, especially, in highly-excited excitonic states. The problem of finding energies of excitonic states in magnetic field is simplified by the conservation of the total momentum of the electron-hole pair [126], which makes it equivalent to the problem of hydrogen atom in magnetic field [127], [1].

The relatively slow motion of electron and hole in the Cu_2O excitonic states is, to a good approximation, decoupled from the dynamics of their spins and can be considered separately. The Lagrangian describing this motion is

$$L = \frac{m_e \dot{\mathbf{r}}_e^2}{2} + \frac{m_h \dot{\mathbf{r}}_h^2}{2} - \frac{e}{c} \mathbf{A}(\mathbf{r}_e) \cdot \dot{\mathbf{r}}_e + \frac{e}{c} \mathbf{A}(\mathbf{r}_h) \cdot \dot{\mathbf{r}}_h + \frac{e^2}{\varepsilon \left| \mathbf{r}_e - \mathbf{r}_h \right|}, \tag{6.10}$$

[1] for a review see I.B. Khriplovich, G.Yu. Ruban, arXiv:quant-ph/0309014v2

where $\mathbf{r}_e(\mathbf{r}_h)$ is the electron(hole) coordinate, m_e and m_h are the electron and hole masses, and $\mathbf{A}(\mathbf{r}) = \frac{1}{2}[\mathbf{H} \times \mathbf{r}]$ is the vector potential (the electron charge is $-e$).

In the center-of-mass and relative coordinates, $\mathbf{R} = \frac{\mathbf{r}_e m_e + \mathbf{r}_h m_h}{m_e + m_h}$ and $\mathbf{r} = \mathbf{r}_e - \mathbf{r}_h$, the Lagrangian has the form,

$$L = \frac{M\dot{\mathbf{R}}^2}{2} + \frac{\mu\dot{\mathbf{r}}^2}{2} - \frac{e}{c}\left(\dot{\mathbf{R}} + \frac{\gamma}{2}\dot{\mathbf{r}}\right) \cdot [\mathbf{H} \times \mathbf{r}] + \frac{e^2}{\varepsilon r}, \tag{6.11}$$

where $M = m_e + m_h$ and $\mu = \frac{m_e m_h}{m_e + m_h}$ are, respectively, the total and the reduced mass of the electron-hole pair,

$$\gamma = \frac{m_h - m_e}{m_h + m_e}, \tag{6.12}$$

and the total time derivative $\frac{e}{2c}\frac{d}{dt}(\mathbf{r} \cdot [\mathbf{H} \times \mathbf{R}])$ was omitted from the Lagrangian.

The corresponding Hamiltonian is

$$H = \frac{1}{2M}\left(\mathbf{P} + \frac{e}{c}[\mathbf{H} \times \mathbf{r}]\right)^2 + \frac{1}{2\mu}\left(\mathbf{p} + \frac{e\gamma}{2c}[\mathbf{H} \times \mathbf{r}]\right)^2 - \frac{e^2}{\varepsilon r}, \tag{6.13}$$

where $\mathbf{P} = M\dot{\mathbf{R}} - \frac{e}{c}[\mathbf{H} \times \mathbf{r}]$ and $\mathbf{p} = \mu\dot{\mathbf{r}} - \frac{e\gamma}{2c}[\mathbf{H} \times \mathbf{r}]$ are, respectively, the total and relative momenta. The Hamiltonian is independent of the center-of-mass coordinate $\mathbf{R}$, which makes the total momentum $\mathbf{P}$ an integral of motion. Since only the excitons with $\mathbf{P} = 0$ are directly excited in an optical experiment, the Hamiltonian can be written in the form,

$$H = \frac{\mathbf{p}^2}{2\mu} + \frac{e}{2\mu c}\mathbf{L} \cdot (\gamma\mathbf{H}) - \frac{e^2}{\varepsilon r} + \frac{e^2}{8\mu c^2}[\mathbf{H} \times \mathbf{r}]^2, \tag{6.14}$$

where $\mathbf{L} = [\mathbf{r} \times \mathbf{p}]$ is the orbital momentum. Equation (6.14) has the form of the Hamiltonian of an electron in the hydrogen atom in a magnetic field $\gamma\mathbf{H}$ and in a parabolic trapping potential in the plane perpendicular to $\mathbf{H}$ (the last term in Eq. (6.14) also known as the Langevin or diamagnetic term).

For convenience we choose the cylindrical coordinates with the z axis along the magnetic field, and $\rho = \sqrt{x^2 + y^2}$. The Hamiltonian (6.14) is invariant under rotations around the direction of magnetic field, therefore $m = \frac{1}{\hbar}L_z$ is a good quantum number. As was discussed in Sec. 6.4, only the exciton states with $m = 0, \pm 1$ are excited in the photoabsorption experiment.

The dependence of eigenfunctions on z and ρ was found numerically by solving eigenvalue problem for the Hamiltonian written in the basis of functions,

$$\psi_{mn_\rho n_z}(\rho, z) = e^{-\frac{(z^2+\rho^2)}{2l^2}}\left(\frac{\rho}{l}\right)^{|m|} L_{n_\rho}^{|m|}\left(\frac{\rho^2}{l^2}\right) H_{n_z}\left(\frac{z}{l}\right), \tag{6.15}$$

where $l = \sqrt{\frac{2\hbar c}{eH}}$ is the magnetic length $l_0 = \sqrt{\frac{\hbar c}{eH}}$ multiplied by $\sqrt{2}$, while H_{n_z} and $L_{n_\rho}^{|m|}$ are, respectively, the Hermite and Laguerre polynomials. In this basis the matrix elements of the Coulomb interaction can be evaluated analytically, which simplifies the calculation of the eigenstates of the Hamiltonian (6.14).

This method is appropriate in the strong-field limit, where the distance between the Landau levels, $\frac{\hbar eH}{\mu c}$, is larger than the exciton Rydberg constant, $\mathrm{Ry}_X = \frac{\mu e^4}{2\varepsilon^2\hbar^2}$. However, using a rather large basis with $n_\rho \leq 10$ and $n_z \leq 10$, we can extend its applicability up to the physically interesting fields of ~ 15T. In the opposite limit of weak fields we diagonalize the Hamiltonian (6.14) in the basis of the zero-field hydrogen wave functions of the discrete spectrum and truncate the basis at $n = 20$. In both cases we checked that the energies of the levels do not change upon a further increase of the basis dimension. The H-dependence of the exciton energies obtained in the two opposite limits matches in the region of intermediate magnetic fields, which allows us to calculate the exciton energies for arbitrary magnetic fields. The dashed lines in figures 6.5 and 6.6 show the magnetic field dependence of the excitonic levels calculated by numerical diagonalization of the Hamiltonian (6.14) superimposed on experimental absorption spectra. The red dots indicate the points of a crossover between high- and low-field lines.

6.6 Fit to experimental data

In order to fit the experimental data, it is necessary to take into account the field-dependence of exciton energies resulting from the interaction of the electron and hole spins with the magnetic field $H \| z$:

$$\hat{H}_{\mathrm{spin}} = -\mu_{\mathrm{B}} H (g_c s_e^z + g_v s_v^z), \tag{6.16}$$

where s_e^z and s_v^z are z-components of the conduction and valence electron spins forming the exciton and g_c and g_v are respectively the $g-$factors of electrons in the conduction and valence band. The interaction of spins with a magnetic field mixes the ortho $|1,0\rangle$ and para $|0,0\rangle$ states and the corresponding energies are:

$$E_\pm = E_0 \pm \sqrt{\left(\frac{\Delta_{\mathrm{o-p}}}{2}\right)^2 + \left[\frac{1}{2}(g_c - g_v)\mu_{\mathrm{B}} B\right]^2}$$

where $\Delta_{\mathrm{o-p}}$ is the exchange splitting between the ortho and para states in zero field. It is proportional to the square of the enveloping electron-hole wavefunction

φ at $r = 0$ [120], which is only nonzero for s-states, whereas electric quadrupole excitation is only allowed to p-states [see Eq. (6.9)]. In fact, existing experimental data on the yellow exciton series shows that the ortho-para splitting is zero for $n > 1$ within the experimental precision [128].

Therefore, in an applied magnetic field the spin part of exciton wave functions has the form,

$$\begin{aligned} \psi_+ &= \frac{|10\rangle + |00\rangle}{\sqrt{2}} = |\uparrow_c\rangle\,|\downarrow_v\rangle\,, \\ \psi_- &= \frac{|10\rangle - |00\rangle}{\sqrt{2}} = |\downarrow_c\rangle\,|\uparrow_v\rangle\,, \end{aligned} \tag{6.17}$$

which allows us to extract the g-factors of electrons in the conduction and valence band (see Sec. 6.7).

Furthermore, to extract the exciton parameters it is important to take into account that the coupling of excitons to the lattice modifies the shape of the absorption peaks, and shifts the maximum of the absorption away from the position in the rigid lattice. The lineshape can be fitted with the asymmetric Lorenzian[129],

$$I(\omega) \sim \frac{\hbar\Gamma/2 + 2A(\hbar\omega - E)}{(\hbar\omega - E)^2 + (\hbar\Gamma/2)^2}, \tag{6.18}$$

where E is the exciton energy in the "rigid" lattice, Γ is the exciton-phonon scattering strength and A is the asymmetry parameter.

The fit of the absorption spectrum for the $n = 2, 3$ excitons at various values of magnetic field is shown in Fig. 6.4, where circles represent the experimental data and the continuous line is a fit by Eq. (6.18). The linewidth $\Gamma = 2$meV for $n = 2$ levels agrees with the results of earlier studies [130].

The excellent quality of the fit allows us to extract the 'bare' exciton energies, indicated by vertical lines. Since the maxima of the absorption spectra are displaced with respect to the bare exciton energies, this procedure enables us to extract the g-factors and masses of electron and hole from experimental data in a more reliable way.

6.7 Discussion

Figures 6.5 and 6.6 show the magnetic field and the light frequency dependence of optical absorption with the calculated excitonic energies superimposed. In accordance with the selection rules, $n \geq 2$ excitons contribute to optical absorption, forming at zero magnetic field hydrogen-like series $\hbar\omega_n = E_{gap} - \frac{\mathrm{Ry}_X}{n^2}$

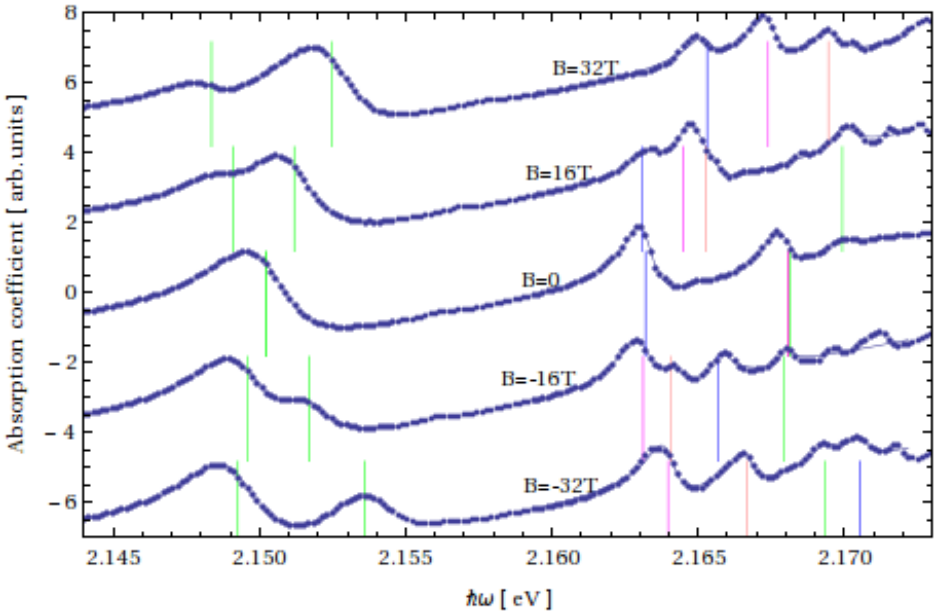

Figure 6.4: The absorption spectrum for the $n = 2, 3$ exciton (dots) at various values of magnetic field fitted with the sum of asymmetric Lorenzian peaks (solid line) The 'bare' exciton energies (see text) are indicated by vertical lines.

with the optical band gap $E_{gap} = 2.174$ eV and the excitonic Rydberg constant $\mathrm{R}y_X = 98$ meV. [2] Using $\epsilon = 7.5$ for the dielectric constant [115, 125, 114], we obtain the reduced mass $\mu = 0.41m_0$ in agreement with Ref. [113].

According to the selection rules derived in Sec. 6.4, the absorption spectrum for the right circularly-polarized light ($\lambda = +1$) is formed by two different sets of states: the states with $S_z = -1$ and $m = 0$ (set 1) and the states with $S_z = 0$ and $m = +1$ (set 2). Dashed lines in Figs. 6.5 and 6.6 show the numerically calculated energies of $n = 2, 3, 4$ exciton states in magnetic field up to 32T, which belong, respectively, to the sets 1 and 2, superimposed on the experimental absorption spectra.

[2] The binding energy of $n = 1$ exciton is anomalously large (150 meV). The exciton radius of the $n = 1$ exciton (7 Å) is comparable to the lattice constant (4.2 Å), which leads to significant central cell corrections and reduced screening of Coulomb interaction responsible for this anomaly [120]. The corrections to the binding energy of the $n = 2$ level, produced by these mechanisms, are negligible.

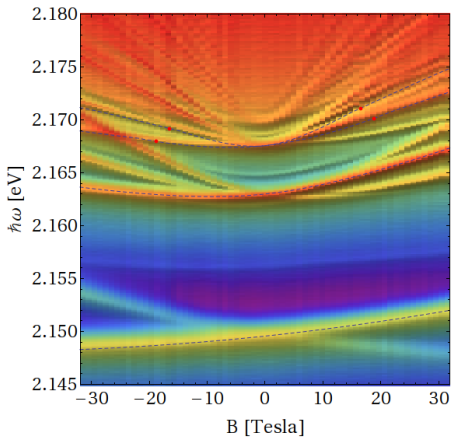

Figure 6.5: The magnetoabsorption spectra measured in the Faraday geometry, $\mathbf{H}\|\mathbf{q}\|(001)$, together with the theoretically calculated magnetic field dependence of the energies for the excitons with $S_z = -1$ and $\mu = 0$ (dashed lines).

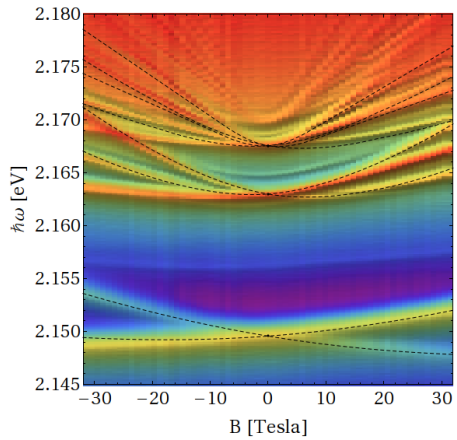

Figure 6.6: The magnetoabsorption spectra measured in the Faraday geometry, $\mathbf{H}\|\mathbf{q}\|(001)$ together with the theoretically calculated magnetic field dependence of the energies for the excitons with $S_z = 0$ and $\mu = -1$ (dashed lines).

Set 1 corresponds to the absorption of a photon with $\lambda = +1$ and creation of an exciton in the state $|1,-1\rangle, m = 0$. The magnetic moment in this state is determined by the atomic g-factors of electrons and holes. Since the hole in the upper valence band has $s_z = 1/2$ and $l_z = -1$, it has zero g-factor since $(l_z + 2s_z) = 0$ [131]. The electron wave function is mostly of Cu s character, and since in this case the spin-orbit interaction is not effective, the g-factor should be close to the bare value of -2. Indeed, a good agreement with the experiment is obtained for $g_c = -2.0$ (see Fig. 6.5).

The last term in the Hamiltonian Eq. (6.14) mixes the state $|l,m\rangle$ with the states $|l,m\rangle$ and $|l \pm 2, m\rangle$. This leads to the mixing of p and f states for $n \geq 4$ giving rise to additional lines. In general the line with the main quantum number n splits in magnetic field into $\left[\frac{n}{2}\right]$ levels (here $[x]$ denotes the largest integer smaller than x).

Set 2 of the absorption lines is produced by the $|1,0\rangle \pm |0,0\rangle, m = 1$ excitonic transitions. This set has twice more states, corresponding to $|\uparrow_c\downarrow_v\rangle$ and $|\downarrow_c\uparrow_v\rangle$.

The energy shifts of these levels up to the terms linear in the magnetic field are

$$E = 2\left(\frac{m_0}{m_h} - \frac{m_0}{m_e}\right)\mu_B H m \pm \frac{1}{2}|g_c - g_v|\mu_B H.$$

We extracted $m_e = 1.0m_0, m_h = 0.7m_0, |g_c - g_v| = 2.25$ and $g_c + g_v = -2.0$, so that for the atomic g-factors of electrons in the conduction and valence bands we obtain, respectively, $g_c = -2.1, g_v = 0.1$ in good agreement with our simple arguments given above ($g_c = -2, g_v = 0$).The effective masses coincide with the results of the cyclotron resonance experiments [114]. These values of the parameters result in good agreement between the calculated and the measured spectra.

gnetic field strength is the ratio of the exciton Bohr radius to the magnetic length, $\beta = \frac{a}{l_0}$. Another dimensionless quantity - the ratio of the distance between the Landau levels, $\hbar\omega$, where $\omega = \frac{eH}{\mu c}$ is the cyclotron frequency, and the exciton atomic unit, $2\mathrm{R}y_X = \frac{e^2}{\varepsilon a}$, equals β^2. In this sense even the strongest field in our experiment, $H = 30\mathrm{T}$, can be considered as weak, as it corresponds to $\beta \sim 0.2$.

To conclude, we studied the magneto-absorption spectrum of cuprous oxide in high magnetic fields and extracted the exciton parameters from the intermediate field region, where the peaks are clearly discernible. Our results suggest that the wide $n = 2$ line is a result of the overlap of two lines with different quantum numbers, resolving a long-standing controversy over the number of excitonic levels in the applied magnetic field. This observation allows us to extract the masses of electrons and holes, which are consistent with the results of cyclotron resonance experiments, and g-factors consistent with the present understanding of the nature of valence and conduction bands of Cu_2O.

Bibliography

[1] L. D. Landau, E. M. Lifshitz, Statistical Physics. Vol. 5 (3rd ed.) (1980), Butterworth-Heinemann.

[2] T. A. Kaplan, Phys. Rev. **116**, 888 (1959).

[3] J. J. Villain, Phys. Chem. Solids **11**, 303 (1959).

[4] A. J. Yoshimori, Phys. Soc. Jpn **14**, 807 (1959).

[5] V. G. Bar'yakhtar, V. A. L'vov and D. A. Yablonskii, JETP Lett., **37**, 673 (1983).

[6] M. Mostovoy, Phys. Rev. Lett., **96**, 067601 (2006).

[7] For a review see D. Khomskii, Physics **2**, 20 (2009).

[8] R. Moessner, A. P. Ramirez, Physics Today **59**, 24 (2006).

[9] Y. Tokunaga, N. Furukawa, H. Sakai, Y. Taguchi, T.-h. Arima, and Y. Tokura, Nature Mater. **8**, 558 (2009).

[10] M. Fiebig, Th. Lottermoser, D. Fröhlich, A. V. Goltsev, R. V. Pisarev, Nature **419**, 818 (2002).

[11] T. Choi *et al.*, Nature Mater. **9**, 253 (2010).

[12] J. Hubbard, Proc. Roy. Soc. A **276**, 238 (1963).

[13] D. I. Khomskii, J. Phys.: Condens. Matter **22**, 164209 (2010).

[14] H. A. Kramers, Physica **1**, 182 (1934).

[15] P. W. Anderson, Phys. Rev. **79**, 350, (1950).

[16] J. Kanamori, J. Phys. Chem. Solids **10**, 87 (1959).

[17] J. B. Goodenough, J. Phys. Chem. Solids **6**, 287 (1958).

[18] I. Dzyaloshinsky, J. Phys. Chem. Solids, **4**, 241 (1958).

[19] Tôru Moriya, Phys. Rev. **120**, 91 (1960).

[20] Tôru Moriya, Phys. Rev. Lett. **4**, 228 (1960).

[21] M. Mostovoy, Lectures on strongly correlated systems at Boulder summer school (2008).

[22] T. Kimura et al., Phys. Rev. B **68**, 060403(R) (2003).

[23] I. E. Dzialoshinskii, JETP **6**, 1259 (1957).

[24] H. Katsura, N. Nagaosa and A. V. Balatsky, Phys. Rev. Lett. **95**, 057205 (2005).

[25] A. Auerbach, *Interacting Electrons and Quantum magnetism*, Chap. 10, (Springer, New York, 1994).

[26] N. L. Schryer and L. R. Walker, Journal of Applied Physics **45**, 5406 (1974).

[27] T. Jungwirth, J. Sinova, J. Masek, J. Kucera, and A. MacDonald, Rev. Mod. Phys. **78**, 809 (2006).

[28] T. Dietl and H. Ohno, MRS Bull. **10**, 714 (2003).

[29] L. Forro et al, J. Appl. Phys. **75**, 633 (1994).

[30] H. Tang et al, J. Appl. Phys. **75**, 2042 (1994).

[31] E. Nagaev, JETP Letters **6**, 484 (1967).

[32] T. Kasuya and A. Yanase, Rev. Mod. Phys. **40**, 684 (1968).

[33] A. Kaminski and S. Das Sarma, Phys. Rev. Lett. **88**, 247202 (2002).

[34] Y. Ishikawa and S. Akimoto, Journal of the Physical Society of Japan **12**, 1083 (1957).

[35] Y. Ishikawa, Journal of Applied Physics **35**, 1054 (1964).

[36] Y. Ishikawa, N. Saito, M. Arai, Y. Watanabe, and H. Takei, Journal of the Physical Society of Japan **54**, 312 (1985).

[37] M. Arai, Y. Ishikawa, N. Saito, and H. Takei, Journal of the Physical Society of Japan **54**, 781 (1985).

[38] M. Arai and Y. Ishikawa, Journal of the Physical Society of Japan **54**, 795 (1985).

[39] M. Arai, Y. Ishikawa, and H. Takei, Journal of the Physical Society of Japan **54**, 2279 (1985).

[40] P. Robinson, R. J. Harrison, S. A. McEnroe, and R. B. Hargraves, Nature **418**, 517 (2002).

[41] R. J. Harrison, American Mineralogist **91**, 1006 (2006)

[42] R. J. Harrison, S. A. McEnroe, P. Robinson, B. Carter-Stiglitz, E. J. Palin, and T. Kasama, Phys. Rev. B **76**, 174436 (2007).

[43] H. Kato, Y. Yamaguchi, M. Ohashi, M. Yamada, and H. Takei, Solid State Commun. **45**, 669 (1983).

[44] R. Bozorth, D. E. Walsh, and A. Williams, Phys. Rev. **108**, 157 (1957).

[45] Y. Ishikawa, JPSJ **17**, 1835 (1962).

[46] Y. Ishikawa, JPSJ **17**, 1877 (1962).

[47] M. Calderon and S. Das Sarma, Annals of Physics **322**, 2618 (2007).

[48] K. P. Belov, A. K. Zvezdin, A. M. Kadomtseva, and R. Z. Levitin, Sov. Phys. Uspekhi **19**, 574 (1976).

[49] V. D. Buchel'nikov, N. K. Dan'shin, L. T. Tsymbal, and V. G. Shavrov, Phys. Usp. **39**, 547 (1996).

[50] A. V. Kimel, A. Kirilyuk, P. A. Usachev, R. V. Pisarev, A. M. Balbashov, and Th. Rasing, "Ultrafast non-thermal control of magnetization by instantaneous photomagnetic pulses", Nature **435**, 655-657 (2005).

[51] T. Kimura, T. Goto, H. Shintani, K. Ishizaka, T. Arima, and Y. Tokura, Nature **426**, 55 (2003).

[52] N. Hur, S. Park, P. A. Sharma, J. S. Ahn, S. Guha, and S-W. Cheong, "Electric polarization reversal and memory in a multiferroic material induced by magnetic fields", Nature (London) **429**, 392 (2004).

[53] A. K. Zvezdin and A. A. Mukhin, "Magnetoelectric interactions and phase transitions in a new class of multiferroics with improper electric polarization", JETP Letters, **88**, 505 (2008).

[54] O. Prokhnenko, R. Feyerherm, M. Mostovoy, N. Aliouane, E. Dudzik, A. U. B. Wolter, A. Maljuk, and D. N. Argyriou, Coupling of Frustrated Ising Spins to the Magnetic Cycloid in Multiferroic $TbMnO_3$, Phys. Rev. Lett. **99**, 177206 (2007).

[55] N. Aliouane, O. Prokhnenko, R. Feyerherm, M. Mostovoy, J. Strempfer, K. Habicht, K. C. Rule, E. Dudzik, A. U. B. Wolter, A. Maljuk, and D. N. Argyriou, Magnetic order and ferroelectricity in $RMnO_3$ multiferroic manganites: coupling between R- and Mn-spins, J. Phys.: Condens. Matter **20**, 434215 (2008).

[56] Y. Tokunaga, S. Iguchi, T. Arima, and Y. Tokura, "Magnetic-Field-Induced Ferroelectric State in $DyFeO_3$", Phys. Rev. Lett. **101**, 097205 (2008).

[57] E. F. Bertaut, in Magnetism, edited by G. T. Rado and H. Suhl (Academic, New York, 1963), Vol. **3**, p. 149.

[58] E. F. Bertaut, J. Chappert, J. Mareschal, J. P. Rebouillat and J. Sivardiere, Solid State Commun. **5**, 293 (1967).

[59] J. E. Bouree and J. Hammann, "Mise en vidence exprimentale des effets de forme dans l'orthoferrite de terbium", J. Phys. (Paris) **36**, 391 (1975).

[60] K. P. Belov, A. K. Zvezdin, and A. A. Mukhin, Sov. Phys. JETP **49**, 557 (1979).

[61] I. Dzyaloshinskii, Sov. Phys. JETP **19**, 960 (1964).

[62] R. Bidaux, J. Bouree and J. Hammann, J. Phys. Chem. Solids **36**, 655 (1975).

[63] N. Kemmer, Nature of the Nuclear Field, Nature **141**, 116 (1938); see `http://www.nature.com/physics/looking-back/kemmer/index.html`

[64] M. Bibes, A. Barthlmy, Nature Materials **7**, 425 (2008).

[65] N. L. Schryer and L. R. Walker, Journal of Applied Physics **45**, 5406 (1974).

[66] A. P. Malozemov and J. C. Slonzewski, *Magnetic domain walls in bubble materials* (Academic Press, 1979).

[67] M. E. Lucassen, H. J. van Driel, C. M. Smith, and R. A. Duine, Phys. Rev. B **79**, 224411 (2009).

[68] S. Geller, J. Chem. Phys. **24**, 1236 (1956).

[69] D. Treves, J. Appl. Phys. **36**, 1033 (1965.

[70] E. Bertaut, Acta Cryst. **A24**, 217 (1968).

[71] R. M. Bozorth, H. J. Williams, and D. E. Walsh, Phys. Rev. **103**, 572 (1956).

[72] A. H. Cooke, N. J. England, N. F. Preston, S. J. Swithenby, and M. R. Wells, Solid State Communications **18**, 545 (1976).

[73] S. Artyukhin, M. Mostovoy, N. P. Jensen, D. Le, K. Prokes, V. G. Paula, H. N. Bordallo, A. Maljuk, S. Landsgesell, H. Ryll, B. Klemke, S. Paeckel, K. Kiefer, K. Lefmann, L. T. Kuhn, and D. N. Argyriou, "Solitonic lattice and Yukawa forces in the rare earth orthoferrite $TbFeO_3$," ArXiv:1103.4275

[74] T. Gilbert, Phys. Rev **100**, 1243 (1955).

[75] D. Treves, Phys. Rev. **125**, 1843 (1962).

[76] A. V. Kimel, B. A. Ivanov, R. V. Pisarev, P. A. Usachev, A. Kirilyuk, and T. Rasing, Nature Physics **5**, 727 (2009).

[77] A. K. Zvezdin, JETP Letters, **29**, 553 (1979).

[78] J. D. Cashion, A. H. Cooke, D. M. Martin, and M. R. Wells, J. Phys. C **3**, 1612 (1970).

[79] G. Durbin, C. Johnson, and M. Thomas, Journal of Physics C: Solid State Physics **8**, 3051 (1975).

[80] G. W. Durbin, C. E. Johnson and M. F. Thomas, J. Phys. C: Solid State Phys., **10**,1975 (1977).

[81] G. A. Smolenskii and I. E. Chupis, Sov. Phys. Usp. **25**, 475 (1982).

[82] A review: S.-W. Cheong and M. Mostovoy, Nature Mater. **6**, 13 (2007).

[83] A review: R. Ramesh and N. A. Spaldin, Nature Mater. **6**, 21 (2007).

[84] Y. Kitagawa, Y. Hiraoka, T. Honda, T. Ishikura, H. Nakamura and T. Kimura, Nature Mater. **9**, 797 (2010).

[85] D. Lebeugle, D. Colson, A. Forget, and M. Viret, Appl. Phys. Lett. **91** 022907 (2007).

[86] J. B. Neaton, C. Ederer, U. V. Waghmare, N. A. Spaldin, and K. M. Rabe, Phys. Rev. B **71**, 014113 (2005).

[87] B. van Aken, T. T. M. Palstra, A. Filippetti, N. A. Spaldin, Nature Mater. **3**, 164 (2004).

[88] Y-H. Chu *et al.* Nature Mater. **7**, 478 (2008).

[89] D. Lebeugle, A. Mougin, M. Viret, D. Colson, and L. Ranno, Phys. Rev. Lett. **103**, 257601 (2009).

[90] V. Skumryev, V. Laukhin, I. Fina, X. Marti, F. Sanchez, M. Gospodinov, and J. Fontcuberta, Phys. Rev. Lett. **106**, 057206 (2011).

[91] Materials where such a correlation does exist are discussed e.g. in C. Fennie, Phys. Rev. Lett. **100**, 167203 (2008).

[92] S. C. Abrahams, Acta Cryst. B **65** 450 (2009).

[93] C. Fennie and K. Rabe, Phys. Rev. B **72**, 100103(R) (2005).

[94] T. Katsufuji *et al.*, Phys. Rev. B **64**, 104419 (2001).

[95] C. delaCruz, F. Yen, B. Lorenz, Y. Q. Wang, Y. Y. Sun, M. M. Gospodinov, and C. W. Chu, Phys. Rev. B **71**, 060407(R) (2005).

[96] S. Lee *et al.*, Nature **451**, 805 (2008).

[97] U. Adem, M. Mostovoy, N. Bellido, A. A. Nugroho, C. Simon and T. T. M. Palstra, J. Phys.: Condens. Matter **21** 496002 (2009).

[98] A. V. Goltsev, R. V. Pisarev, T. Lottermoser and M. Fiebig, Phys. Rev. Lett. **90**, 177204 (2003).

[99] E. Hanamura, K. Hagita and Y. Tanabe, J. Phys.: Condens. Matter **15**, L103 (2003).

[100] M. Mostovoy, Nature Mater. **9**, 188 (2010).

[101] M. Fiebig, T. Lottermoser, and R. V. Pisarev, J. of Appl. Phys. **93**, 8194 (2003).

[102] U. Adem, "Magnetodielectric Coupling in Multiferroic Transition Metal Oxides", Zernike Institute for Advanced Materials Ph.D. thesis (2008).

[103] T. J. Sato, S.-H. Lee, T. Katsufuji, M. Masaki, S. Park, J. R. D. Copley, and H. Takagi, Phys. Rev. B **68**, 014432 (2003).

[104] B. Ueland, J. W. Lynn, M. Laver, Y. J. Choi, and S.-W. Cheong, Phys. Rev. Lett. **104**, 147204 (2010).

[105] E. F. Gross and N. A. Karryev, Dokl. Akad. Nauk SSSR[Sov. Phys.— Doklady] **84**, 261 (1952).

[106] M. Hayashi, J. Fac. Sci. Hokkaido Univ. **4**, 107 (1952).

[107] R. Elliott, Phys. Rev. **108**, 1384 (1957).

[108] R. Elliott, Phys. Rev. **124**, 340 (1961).

[109] G. F. Koster, Solid-State Physics, edited by F. Seitz and D. Turnbull (Academic Press, Inc., New York, 1957), Vol. 5, p. 174.

[110] M. French, R. Schwartz, H. Stolz, and R. Redmer, J. Phys.: Condens. Matter **21**, 015502 (4pp) (2009).

[111] F. Bruneval, N. Vast, L. Reining, M. Izquierdo, F. Sirotti, and N. Barrett, Phys. Rev. Lett. **97**, 267601 (2006).

[112] E. F. Gross and B. P. Zakharchenya, Dokl. Akad. Nauk SSSR[Sov. Phys.— Doklady] **111**, 564 (1956).

[113] A. G. Zhilich, J. Halpern, and B. P. Zakharchenya, Phys. Rev. **188**, 1294 (1969).

[114] J. W. Hodby, T. E. Jenkins, C. Schwab, H. Tamura, and D. Trivich, J. Phys. C **9**, 1429 (1976).

[115] J. Halpern and B. P. Zakharchenya, Solid State Commun. **5**, 633 (1967).

[116] M. Seyama, T. Takamasu, Y. Imanaka, H. Yamaguchi, T. Masumi, and G. Kido, J. Phys. Soc. Jpn. **72**, 437 (2003).

[117] M. Kobayashi, K. Kanisawa, A. Misu, Y. Nagamune, S. Takeyama, and N. Miura, J. Phys. Soc. Jpn. **58**, 1823 (1989).

[118] K. Hammura, K. Sakai, and M. Seyama, Prog. Theor. Phys. Suppl. **138**, 143 (2000).

[119] H. Sasaki and G. Kuwabara, J. Phys. Soc. Jpn. **34**, 95 (1973).

[120] G. M. Kavoulakis, Y.-C. Chang, and G. Baym, Phys. Rev. B **55**, 7593 (1997).

[121] C. Uihlein, D. Fröhlich, and R. Kenklies, Phys. Rev. B **23**, 2731 (1981).

[122] V. A. Kiselev and A. G. Zhilich, Fiz. Tverd. Tela **13**, 2398 (1971).

[123] G. Pikus and G. Bir, Zh. Eksp. Teor. Fiz. **60**, 195 (1971).

[124] M. Denisov and V. Makarov, Phys. Status Solidi B **56**, 9 (1973).

[125] D. Fishman, C. Faugeras, M. Potemski, A. Revcolevschi, and P. H. M. van Loosdrecht, Phys. Rev. B **80**, 045208 (2009).

[126] L. Gor'kov and I. Dzyaloshinskii, JETP **26**, 449 (1967).

[127] Y. Lozovik and S. Volkov, JETP **96**, 564 (2003).

[128] M. Jörger, T. Fleck, C. Klingshirn, and R. von Baltz, Phys. Rev. B **71**, 235210 (2005).

[129] Y. Toyozawa, J. Phys. Chem. Solids **25**, 59 (1964).

[130] L. P. Zverev, M. M. Noskov, and M. Y. Shur, Sov. Phys.— Solid State **2**, 2357 (1961).

[131] C. Ballhausen, *Introduction to ligand field theory* (McGraw-Hill Book Company, Inc., 1962).